INVERSE PROBLEMS IN DISORDERED SYSTEMS

Shardul S. Mukim

A THESIS SUBMITTED FOR THE DEGREE OF
DOCTOR OF PHILOSOPHY

SCHOOL OF PHYSICS
TRINITY COLLEGE DUBLIN

2023

DECLARATION

I, Shardul Mukim, hereby declare: This thesis has not been submitted as an exercise for a degree at this or any other university; That it comprises work performed entirely by myself during the course of my Ph.D. studies at Trinity College Dublin; That I was involved in a number of collaborations, and where it is appropriate my collaborators are acknowledged for their contributions.

A copy of this thesis may be lended or copied by the Trinity College Library upon request by a third party provided it spans single copies made for study purposes only, subject to normal conditions of acknowledgement.

Paul D. Gorman

February 14, 2023

"It's a magical world, Hobbes, ol' buddy...let's go exploring

— Bill Watterson

ABSTRACT

It is a simple Quantum Mechanics problem to find the electronic conductance of a device by directly solving the Schrodinger Equation. Obviously, this is the case if and only if the underlying Hamiltonian is known, i.e., if all scattering sources are fully specified. Trying to perform the same task in reverse is significantly more challenging. For example, assuming that the device conductance is known, how can one infer about the Hamiltonian components from that information alone? To make matters worse, what if the device is made of a heavily disordered material? Questions of this type are generally labelled as Inverse Problems (IP) and are classified as those which attempt to obtain from a set of observations the causal factors that generated them in the first place. IP are integral parts of classical visualization tools but far less common in the quantum realm. Materials Science is ideal for applications of inverse problem since it involves studying structures for which the underlying Hamiltonians are rarely known. Identifying the precise Hamiltonian that generates a specific observable is a difficult process. In general, it consists of solving the Schrodinger equation with a Hamiltonian containing one (or more) parameter(s) that must be changed until the solution closely matches the original observation. Because of the gigantic number of possibilities, finding the exact configuration is computationally very demanding. Efficient codes and powerful computers alone are not sufficient to make this approach feasible and alternative ways of probing the phase space of possibilities are needed.

In this thesis, I introduce a simple mathematically-transparent inversion technique capable of extracting structural and compositional information from a disordered quantum device and nanowire/nanosheet networks by looking at their electronic signatures. We put forward an efficient way that can quantify the overall concentration of scatterers in a device. In addition, a sudoku style technique is also presented

which enables us not only to specify the total number of scatterers but also to determine how they are spatially distributed.

PUBLICATIONS

Publications resulting, partially or wholly, from this work:

- **S. Mukim**, F. P. Amorim, A. R. Rocha, R. B. Muniz, C. Lewenkopf, M. S. Ferreira
  Disorder information from conductance: a quantum inverse problem
  Phys. Rev. B 102, 0755409 (2020)

- F. R. Duarte, **S. Mukim**, A. Molina-SÃ¡nchez, Tatiana G. Rappoport, M. S. Ferreira
  Decoding the DC and optical conductivities of disordered MoS2 films: an inverse problem
  New Journal of Physics, Volume 23, July 2021

- **S.Mukim**, J. O'Brien, M. Abarashi, M. S. Ferreira, C. G. Rocha
  Decoding the conductance of disordered nanostructures: a quantum inverse problem
  J. Phys.: Condens. Matter 34 085901 (2022)

- **S. Mukim**, C. Lewenkopf, M.S. Ferreira
  Spatial mapping of disordered 2D materials: the conductance Sudoku
  Carbon 188, 360 (2022)

- **S.Mukim**, M. Kucukbas, S. R. Power and M. S. Ferreira,
  Characterization of zigzag edged Graphene nanoribbons using spin current
  In preparation

ACKNOWLEDGEMENTS

Over the last 1452 days and a pandemic, I have received an unmeasurable amount of guidance and support from numerous people. To begin with, I would like to thank Prof. Mauro Ferreira for his guidance, zest and, most importantly, patience. He gave me this opportunity to study under his supervision and allowed me to develop many of my skills. I stumbled upon many difficulties during the PhD and Mauro was always available to discuss and point me in the correct direction. I am incredibly grateful for his constant support and our numerous brainstorming sessions over the last few years.

PhD allowed me to collaborate with some of the finest researchers. Mainly, I would like to thank Prof. Caio Lewenkopf Dr. Roberto Bechara, Dr. Alex Rocha and Dr. Claudia G. Rocha for the fruitful collaborations we had from the start. I am thankful for lively, informative and equally entertaining discussions. I am also grateful to Dr. Stephen Power for his encouragement and creative ideas. The online coffee meetings were always a source of laughter in a pandemic. I am also grateful to Prof. Jonathan Coleman and Prof. Cormac McGuinness for valuable insights and suggestions. I would like to thank many of my office colleagues who have always been there to share this journey. To begin with I must thank Meric for his support and friendship over the last four years. I would also like to thank Dr. Urvesh Patil, Dr. Sumanta Bhandary ,Umit, Felippe and office members of 2.21 for creating an enjoyable environment, Fabio for sitting through so many of my trial talks.

On a personal note, I am lucky to have friends to go along with over the years. Ammar, Arunima and Sagar, you have been the best fellowship any hobbit can ask for. I would also like to thank many of my housemates especially Surojit, Saurabh and Unmesh for time we shared together. I would also like to thank Avani, Rasika and Vikram for their friendship and constant support. Dhanashree, without your love and support this thesis would not have been possible. To my cousins, aunts and

uncles, thank you for your moral support. Finally, I am incredibly grateful to Shweta, Shree and my parents for their unwavering love, support and encouragement. I would not be where I am today without your love. Thank you.

CONTENTS

LIST OF FIGURES

COMMON ACRONYMS

AC Armchair

ACNT Armchair Carbon Nanotube

AGNR Armchair Edged Graphene Nanoribbon

HbN Hexagonal Boron Nitride

CNT Carbon Nanotube

CVD Chemical Vapour Deposition

DFT Density Functional Theory

DOS Density of States

FM Forward Modelling

IM Inverse Modelling

GF Green's Function

CA Configurational Average

LDOS Local Density of States

RKKY Ruderman-Kittel-Kasuya-Yosida

ZZ Zigzag

ZZNT Zigzag Carbon Nanotube

ZGNR Zigzag Edged Graphene Nanoribbon

CPE Coherant Phase Element

NWN Nanowire Network

STM Scanning Tunneling Microscopy

1

INTRODUCTION

1.1 INTRODUCTION

In 1821, Alexis Bouvard, a French astronomer, published data describing the orbit of Uranus. However, the observed data revealed substantial deviation from the published data. Bouvard suggested that the deviation is a result of perturbation induced due gravitational field of another planet. This led to the discovery of Neptune as the 8^{th} planet in the solar system. This is one of the earliest examples of what is known as the inverse problem in science [1]. All problems in non-relativistic physics can be classified into two techniques, forward problem and inverse problem. Forward modelling, *i.e.* forward problem schemes are well-defined and commonly used techniques in science. As a result of which comprehension of forward problems is far more complete than its complementary counterpart [2–4]. Forward modelling allows us to calculate response of the system for predetermined input parameters. One well-known example of the forward modelling scheme in science is the Schrödinger equation that governs the wave function of a quantum mechanical system. For a given hamiltonian operator the wave function evaluates state of the system. Hamiltonian operator encodes necessary information about the quantum mechanical systems, *i.e.* input parameters. Most problems in condensed matter physics require solving the wave equation in one form or another. Such forward problems are defined to understand the cause-effect relationship. In reality, the solution of the forward problem is closer and smoother to the observed data as, by definition, forward problems define unique, stable and complete solutions [5].

The inverse technique has been a fundamental aspect of problem-solving in science. Inverse problems (IP) is a method of extracting information about causal

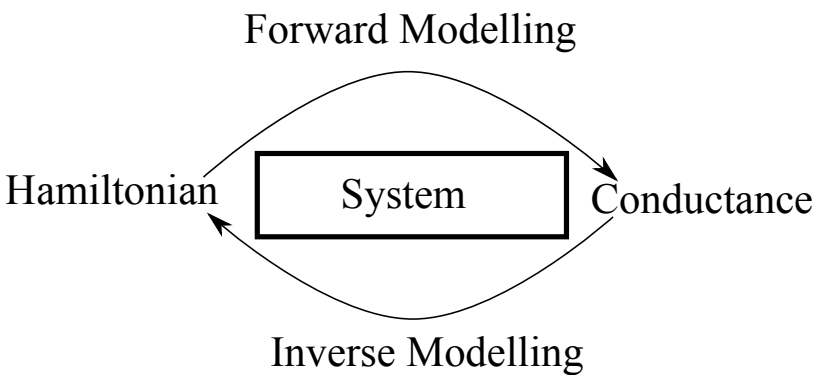

Figure 1.1: Two types of modelling techniques are defined in terms of the transport property of a system. Hamiltonian, *i.e.* encodes the input parameters of the system to generate the the output using forward modelling technique. Inverse modelling uses the observed information (in this case conductance) to derive the input parameters.

factors of a phenomenon from its observed effect. To solve a new problem, one must account for the unknown interactions and variables. Thus it is necessary to develop the inverse mechanisms along with the forward technique to equal lengths. In quantum mechanics, IP were investigated from a purely mathematical perspective to obtain unique and stable solutions [6]. Since the development of scattering matrix theory, IP in quantum mechanics, especially in nuclear and molecular physics, mainly revolves around the reconstruction of the potential from scattering operators [7–9]. Ideally, IP defines analytically how the observed data transforms and reconstructs the model. In very few cases, such IP exists with noise-free data. IP suffers from the problems associated with the uniqueness and completeness of the characterisation data to derive information about the scatterers. However, a practical approach to solving the inverse problems is necessary to keep up with the ever-developing fabrication techniques and forward methods. In realistic situations defining the IP becomes tricky as it requires accommodating random disorders and seemingly unpredictable electronic dynamics induced because of perturbations. As a result,the inverse model usually suffers from the problem of uniqueness. The results obtained from the inversion of experimental data is not always equal to the true model. Additional information about the underlying factors is necessary for the IP to recreate forward model. Interrogating the various aspects of the system is

one way to enhance the accuracy of IP. Such IP are an intrinsic part of the numerous visualization tools but is not that common in the quantum realm and even less so in the presence of disorders [10–13].

Condensed matter physics is a fertile ground for developing inverse problems, but unfortunately, it has been overlooked over development of forward techniques. Deriving a mathematical description of the N-particle system from the observed scattering data is not an easy task, especially if the interactions are unknown. Recent experimental advancements have benefited from characterisation techniques like Scanning Tunnelling Microscopy (STM) or Atomic force Microscopy (AFM). However, they require detailed analysis of convoluted data with various practical aspects playing a role in it. Developing inverse computational methods can provide well needed assistance to experimental and theoretical modelling schemes. The literature on field of the quantum inverse problem is mainly focused on the fundamental inversion processes determining whether the problem is ill-posed or solutions are unique and stable [14, 15]. Following different scope studies of nanomaterials and their physical properties could benefit from applications of quantum IP since they involve investigating structures for which the underlying hamiltonian is not always known [16–24]. Recently machine learning techniques and neural-network based search engines are being used to invert the observables to obtain the quantum mechanical systems [25–38] but these are large-scale simulations that generate large volumes of data with the intention of identifying the ideal parameters describing the system. With different degrees of success these simulations can speed up the search for the "inverted" configuration. As a result, simulations are starting to have an impact in reducing the time and cost associated with materials design, specially those involving high throughput studies of material groups. A more intuitive approach is necessary along with data science driven techniques to extract fundamental information about the physical processes from their observables. A significant portion of the condensed matter community is versed in the electronic transport problem in quantum devices and nanomaterial network. In this work, we wish to lay out an inversion technique that can be used to extract fundamen-

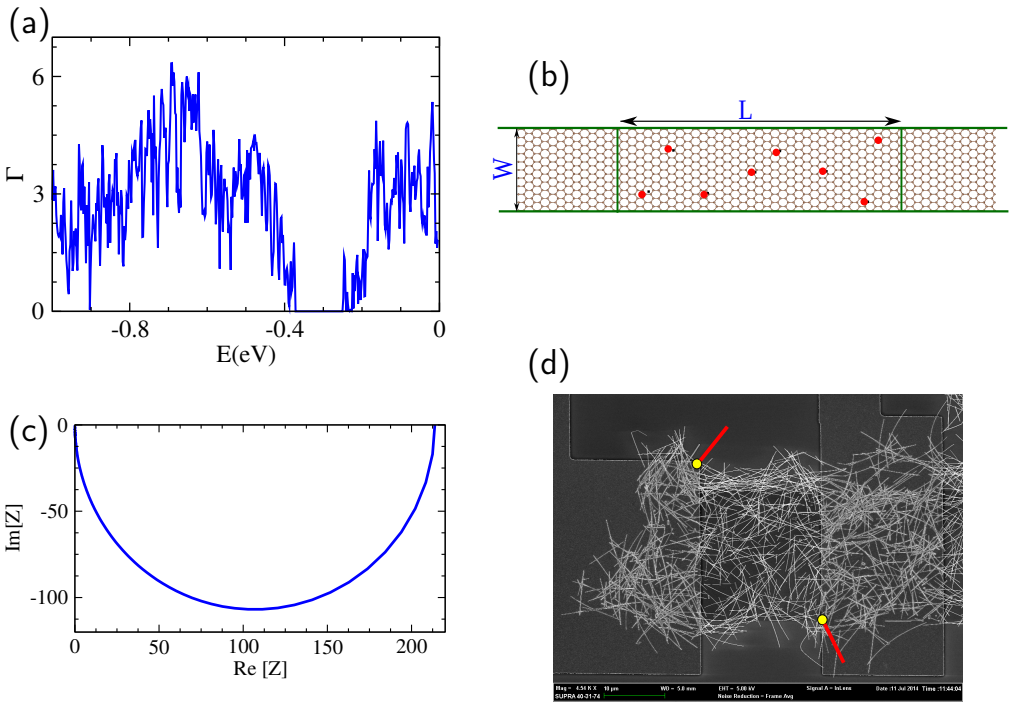

Figure 1.2: Panel(a) depicts the transmission signature of a graphene-based quantum device with nitrogen atom embedded in it. Panel (b) shows the schematic of a graphene nanoribbon system with impurities indicated with red dots. (c) Frequency dependent impedance data of a nanowire network. Panel (d) shows the STM image of a randomly distributed silver nanowire network. Electrodes are connected to the network at yellow colour positions.

tal structural information of quantum devices and nanomaterial networks from corresponding electronic signatures.

1.2 QUANTUM DEVICES

The expansion of computational power and characterisation techniques over the past few decades is unquestionably one of the key reasons for the unprecedented level of accuracy in material development [39–42]. It is a straightforward task to find the electronic properties of a quantum device by directly solving Schrödinger's equation that governs a wave function of the quantum system under study. The Development of quantum transport methodologies in micro-systems is the focus of extensive research. Advancements in the fabrication of nanoscale devices whose dimensions

are smaller than mean free electron path has gone beyond the predictions of Moore's law.

The introduction of disorders is one way of modifying the electronic properties of nanodevices [43–45]. For instance, transition metal dichalcogenides (TMDs) show remarkable electronic and mechanical properties and has been in focus during the last decade for various applications [46–50]. Due to the type of atomic bonding in monolayer TMDs, the structural disorder in the form of vacancies is one common type. However, presence of vacancies gives rise to new properties such as local magnetic moments and converting the compound into p or n type semiconductors [51–53]. Graphene is another extremely versatile material which shows exciting mechanical and electrical properties. We use graphene devices extensively in this thesis to present the inversion methodology. The high charge mobility offered by graphene is a coveted aspect in nano-electronics [54]. The simple electronic structure of graphene introduces a significant level of mathematical transparency to describe its properties. Graphene devices ranging from field effect transistors to sensors are widely studied. Carbon nanotubes and graphene nanoribbons are promising candidates as a sensing material [45, 55]. They can be produced with high level of purity and foreign material have an impact on the physical and electronic properties of the host material which makes them an ideal candidate for sensing purposes. Electronic response of the sensors and other devices is key to various applications. DC Conductance of the device is one of the critical quantities of our interest.

1.3 NANOMATERIAL NETWORK

Another wide area for research in nanoscience relates to the engineering of novel nanowire or nanosheet materials. Nanomaterials possess very different properties from their bulk counterparts. Due to the confinement of electrons, electronic properties are governed by quantum mechanics. When arranged randomly over a flat surface the system forms a mesh or network of nanomaterials. Such network possess the properties of individual element modulated by the many body physics. Mesh or

network of highly conductive thin-films with high optical and electrical properties randomly spread on the surface is one fine example of a nanomaterial network with the applications ranging from transparent displays to neuromorphic devices [56–59]. Fabrication techniques of such networks are scalable and inexpensive. Over the last few decades complexity of such networks has evolved from simple capacitors to thin film transistors [60]. Different electrical, mechanical and optical properties can be engineered by using different types of nanomaterials and connectivity of the network . Many examples of nanomaterial network based sensors, fuel cells and transparent heaters are found in the literature. Silver nanowires bent upto 160 deg can remain conductive and returns to the original sheet resistance when induced stress is removed [61].

Another exciting aspect of metallic nanowire networks is the memristive behaviour of the network [62]. Memristive devices are resistors but with a dynamic relationship between current and voltage applied to it. A highly connected Memristive nanowire network has wide range of applications ranging from the neuromorphic computing architectures to analog devices. Modelling of such devices to examine the electrical properties can be done using network theory in an analogous way to the quantum devices. The weighted adjacency matrix plays an analogous role to the hamiltonian of quantum device encodes network properties. Randomness and connectivity associated with the distribution of nanowires/nanosheets plays an important role in defining the network properties [63–65]. There are different techniques available to tune the junction parameters to specific applications. This makes study of nanowire/nanosheet networks a good candidate to study for IP. To obtain the connectivity and distribution of nanowires and nano-flakes accurately is a difficult task. Scanning electron microscopy is used to obtain the connectivity of network. However, deriving connectivity and junction properties of a random nanomaterial becomes a tedious task with increase in the dimensions of systems. Deciphering impedance data to determine the distribution and connectivity of nanomaterials in the network can provide an alternative to the traditional characterisation techniques

Fig. 1.2(a) shows the transmission signature of graphene nanoribbon as a function of energy derived from the hamiltonian corresponding to the schematic presented in panel (b). Similarly, Fig. 1.2(c) depicts the frequency dependent AC impedance of the network shown in Fig. 1.2(d). Such IP are not well defined in condensed matter physics but common and widely used in other areas of science. Extracting information about the underlying hamiltonian is a coveted task in quantum mechanics. The argument we are trying to make is that the information about scattering centres present in the system is encoded in the transmission signal. *Can we define the inverse problem using conductance signatures of a device?* This thesis is structured around defining two inverse problems. The first half of this work defines the IP for nanodevices using its DC conductance spectra. Disorder is ubiquitous in mesoscopic systems and detrimental to the IP. For instance, due to quantum interference electronic transport properties show universal fluctuations at low temperature in ballistic and diffusive transport regimes. Extracting information about the underlying hamiltonian from universal signatures is particularly challenging. The methodology presented in this thesis uses disorder to its benefit to extract information about the underlying hamiltonian. As conductance depends delicately on the spatial mapping of scattering centres in the conducting channels. The next question in the inverse problem we propose is *can we extract spatial mapping of scattering centres in the system?* In the second half of the thesis we try to define the IP using randomly distributed nanowire/nanosheet networks. Electronic transport at nanoscale and micro scale is fundamentally different in nature. The IP defined for the NWNs deals with the AC impedance signature of the device. We define the IP to determine the junction properties of network which governs the electronic transport properties of the network.

1.4 LAYOUT OF THESIS

The work presented in this thesis is focused on defining the inverse problem which revolves around the questions posed in the earlier section. This work comprises 3 major projects constituting 5 chapters. They are organised as below:

1.4.1 *Mathematical methods*

Chapter 2 presents the general theoretical framework necessary to define the forward and inverse modelling techniques. Conductance of a quantum device depends on the electronic structure of the host material and disorders associated with it. The chapter introduces Green function (GF) formalism, one of the most versatile tools available to describe an electronic system. GF can be derived from the chosen hamiltonian and provide direct access to the density of states. We then demonstrate the Dyson equation and one of its application in form of recursive algorithm. Dyson equation can be used to not only connect the unit cells of host material but also to describe the perturbed system. Disorder is central to the IP defined in this thesis. We present a simple application of Dyson equation with substitutional type of disorder. The single particle Green functions are extensively used throughout this thesis. In particularly to calculate the DC conductance and AC impedance of nanodevices and complex networks respectively. Green's function-based methods have played a central role as a theoretical tool to study electronic and transport properties of nanoscale systems [66]. We introduce the basics of electronic transport in nanodevices with the help of the Landaur-Büttiker formalism using graphene nanoribbons as the host material.

1.4.2 *Disorder information from conductance*

In this chapter we present fundamentals of the inverse problem for nano systems. We address question posed earlier. It is important to differentiate between the forward and inverse problem. Forward modelling schemes are by necessity well defined techniques. These are versatile methods that can be used to obtain the conductance of complex low dimensional materials, including disordered ones [67–76]. We present the kubo formalism to derive the conductance of two terminal system [77]. We define the basic elements of IP with the help of systems with simple electronic structure. We define onfigurational average (CA) in the next section using the Kubo formalism. Mathematical construct of this IP is defined with the help configurational averages. CA brings the forward modelling aspect necessary to every IP. We study the effect of disorders in the form of randomly distributed impurities on the electronic transport properties. In this section we analyse the statistical significance of disorders on the conductance of nano systems. The misfit function is defined in the next section which uses the conductance spectrum to obtain concentration(number) of impurities present in the system. In the following sections we prove that the method is indeed material independent with the help of graphene nanoribbons, carbon nanotubes and hexagonal boron nitride. Using multi-variable misfit functions we demonstrate that it is possible to extract other structural information about underlying hamiltonian. This section shows misfit function is equipped to estimate information about more than one type of impurities along with their scattering strengths. We also go on to show the robustness of IP to extract information about a system described using realistic hamiltonians calculated within density functional theory. The chapter concludes with the error analysis of the misfit to determine the scope as a function of the disorder concentration.

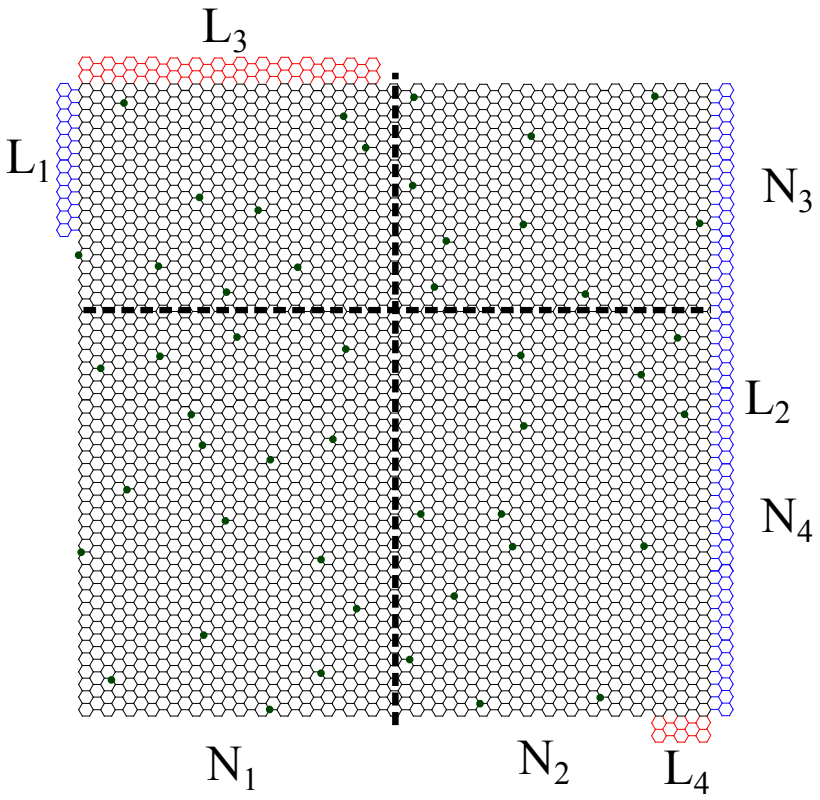

Figure 1.3: A schematic of graphene flake embedded with impurities and 4 different electrodes connected to the system. Black dashed line resolves the device in 4 virtual regions defined for the inversion.

1.4.3 *Sudoku Problem*

Chapter 3 outlines the IP which can extract fundamental structural information about the hamiltonian in form of occupation and type of disorders present in the system. This chapter outlines an algorithm to map the position of disorders using the misfit function formalism aiming to address question 1.3.

The inversion methodology can be written in terms of various degrees of freedom. A multi-terminal approach is not only viable for the experimental set-ups but also allows to interrogate the system in various ways. Within the Landauer-Büttiker formalism we show that IP is independent of choice and arrangement of electrodes. This also provides a new avenue to interrogate the system in creative ways. An example arrangement is shown in Fig. 1.3 , Graphene flake connected with 4 electrodes can resolve the occupation of impurities in 4 regions defined by the

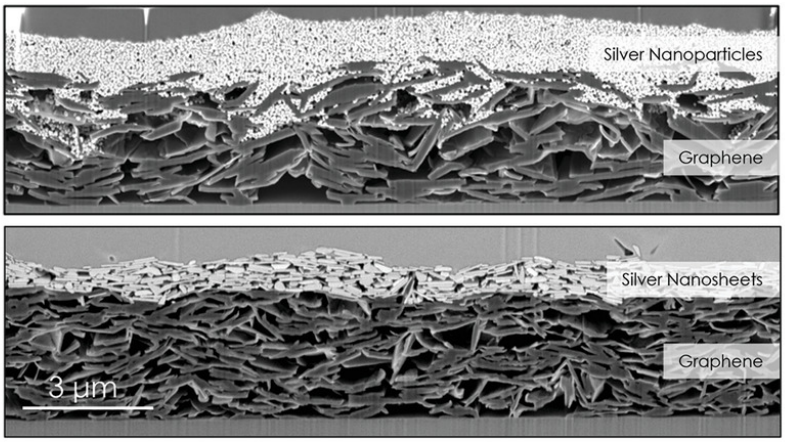

Figure 1.4: Cross section of graphene nano sheet network with silver nanoparticles and nanoflakes coated on top of it.

dashed black lines. The 1-D misfit function accurately predicts occupation of disorders present in the device for any two electrode pairs. Multivariable misfit function allows us to resolve the occupation of impurities in $N_1, .., N_4$, where N_1 is the number of impurities present on the left part of vertical dashed line and N_4 is the number of impurities on the bottom part of the horizontal dashed line. To find occupation in each cell we need to solve a system of linear equation defined with the help of $N_1, .., N_4$. For a graphene flake of dimensions $D_x = 30\sqrt{2}a$ and $D_y = 50a$ we show that it is possible to extract occupation of impurities in region defined by $D_x^R \approx 7a$ and $D_y^R = 10a$. The mapping of device in such grid like structure to find the exact concentration of impurities highly resembles a Sudoku puzzle.

1.4.4 *Network Inversion*

In chapter 4, we aim to define the IP for macroscale systems in form of nanowire and nanosheet network. We present the necessary theoretical modelling techniques required for the simulation of random nanowire-nanosheet networks. In this part we briefly introduce network theory and establish necessary greens functions formalism to model the AC impedance data of the network. For the quantum inversion problem we defined the energy dependent conductance spectrum as the input function, but

in the case of netwroks impedance spectrum can be used. We show that the ergodic hypothesis remains valid for the macroscale systems. The disorder in manifests in the form of connectivity and junction properties in the case of networks. The inverse problem presented in the chapter aims to decode this information with the help of misfit functions. Fig 1.2(d) is an SEM image of randomly distributed nanowire network. However to extract connectivity of a nanosheet network is still a task. Fig. 1.4 shows the cross section of graphene network with Silver nanoparticles and silver nano-flakes deposited on top [78] [1]. We show that misfit function can extract 6 different bits of network information in form of junction properties by analysing the impedance data. For systems whose electrical properties are dominated mainly by the junction parameters, We define a general behaviour of the impedance function within the framework of misfit function which can be used as an alternative way to identify the junction properties or connectivity. We conclude the chapter with error analysis of the inversion procedure.

1.4.5 *Future work and Summary*

In the final chapter 6, we aim to address last question proposed to define the IP. Inverse problem defined in this work relies on the two point correlation functions, DC conductance and AC impedance of a nanodevice and nanowire network respectively. Other quantities such as magnetic susceptibilities, optical conductance or thermal conductance. The inversion methodology can extract basic structural information about the underlying hamiltonian of complex media using these quantities. In the first section of the chapter, we define the problem characterisation of the disorders present on either edges of the graphene nanoribbon from the spin-polarised conductance of the system. For zig-zag edged graphene nanoribbon we show that spin-polarised conductance encodes the information about disorder in the lower energy region. In the next section we discuss the possible characterisation of Winner takes all (WTA) random nanowire systems.

1 Image is obtained from Adam kelly et al [78]

We now start with an introduction to the mathematical methods that we will use throughout this work.

2

MATHEMATICAL METHODS

This chapter will introduce the mathematical tools and methods necessary to define and solve inverse problems (IP) presented in this thesis. We will introduce the elements required to understand electronic transport properties of materials. Because most of the quantities used in this thesis are developed using Green Function (GF) formalism which we introduce first, followed by the description of Dyson equation and recursive algorithm. We see how these techniques can be used to model nanoscale systems, particularly disordered systems. As mentioned in the introductory chapter we use transmission signature of a device to define the IP. The subsequent section will introduce Landauer-Büttiker formalism for two terminal and multiterminal systems to calculate the transport signatures of quantum devices.

2.1 GREEN FUNCTION

In 1828, a self taught mathematical physicist named George Green published "An essay on the application of mathematical analysis to the theories of Electricity and Magnetism" where he introduced Green functions (GF). GF formalism is a versatile mathematical tool available to solve a variety of problems in physics. GFs are solutions to linear differential equation that are used to relate the response of a system to source function. Many problems in condensed matter physics revolve around solving Schrödinger's equation describing the quantum states of the system. Feynman used GF to define propagation of electrons in quantum electrodynamics to study the scattering of particles for a perturbation. Synonymously many transport methods are developed using the GF formalism [79–84]. As we shall see in following sections of this chapter, GF are closely related to the description of electronic

structure and density of states of solids. Solving the Schrödinger equation for a given Hamiltonian itself can be tedious task for complex system and worse in presence of disorders. GF are extremely useful in order to incorporate disorders in the system. Throughout this work we will present electronic transmission signatures of numerous disordered Hamiltonian calculated using GF. Although our calculations do not explicitly consider the electron-electron interactions in Hamiltonian, this can be easily included if necessary. For practical purposes here we shall focus on the single particle GF. We first present a generic differential equation defined for a linear and hermitian operator $\hat{J}$ as

$$\hat{J}x(a) = f(a) \tag{2.1.1}$$

The Green function, $\hat{G}(a,b)$ for the linear operator $\hat{J}$ is defined as

$$\hat{J}\hat{G}(a,b) = \delta(a-b) \tag{2.1.2}$$

Note that b is the dummy variable which allows us to construct $f(a)$ by adding together all the delta functions as

$$f(a) = \int_0^\infty dbf(b)\delta(a-b) \tag{2.1.3}$$

The complete solution to Eq. 2.1.1 is given as

$$x(a) = \int_0^\infty db\hat{G}(a,b)f(b) \tag{2.1.4}$$

This allows us to solve the differential equation by working out $\hat{G}(a,b)$ of the system and then integrating over b to get the solution $f(a)$. It is important to note that $\hat{G}(a,b)$ needs two arguments. The first one (a) is the variable of interest and the second (b) decides the position of delta function that we use to define the GF

in Eq. 2.1.1. In case of the Schrödinger equation we can define GF for a given Hamiltonian $\hat{H}$ describing the system as

$$\hat{G} = \lim_{\eta \to 0} [(E \pm i\eta)\hat{I} - \hat{H}]^{-1}, \tag{2.1.5}$$

Here, $\hat{I}$ is the identity operator, E is the energy and η is a small positive imaginary part added to obtain well defined GF around the eigenvalues of Hamiltonian. Limits taken for the + and - corresponds to the retarded and advanced GF respectively. Retarded (G^R) and Advanced (G^A) GF define the propagation of particle away from the site and towards the site respectively. Note that GF is a general quantity defined by the Hamiltonian of system. Comprehensiveness of the GF is reflected from the Hamiltonian it corresponds to. This allows us to use GF to describe numerous material properties. To begin with in the next section we introduce the derivation of Density of States (DOS).

2.2 DENSITY OF STATES

To derive the DOS, we define a Hamiltonian in the basis set with eigenvalues ϵ_a and eigenstates $|\psi_a\rangle$ as

$$\hat{H} = \sum_a |\psi_a\rangle \epsilon_a \langle\psi_a| \tag{2.2.1}$$

Using Eq. 2.1.5 we can write,

$$\hat{G} = \lim_{\eta \to 0} \sum_a |\psi_a\rangle \frac{1}{E + i\eta - \epsilon_a} \langle\psi_a| \tag{2.2.2}$$

In the basis of $|x\rangle$, we can write the GF as,

$$G_{x,x'} \equiv \langle x|\hat{G}|x'|\rangle = \sum_a \langle x|\psi_a\rangle \frac{1}{E + i\eta - \epsilon_a} \langle\psi_a|x'\rangle, \tag{2.2.3}$$

Multiplying numerator and denominator of Eq. 2.2.3 with $(E - i\eta - \epsilon_a)$ we can write,

$$G_{x,x\prime} \equiv \langle x|\hat{G}|x\prime|\rangle = \lim_{\eta\to 0} \sum_a \langle x|\psi_a\rangle \frac{E - i\eta - \epsilon_a}{(E-\epsilon_a)^2 + \eta^2} \langle \psi_a|x\prime\rangle, \tag{2.2.4}$$

Taking the imaginary part we are left with,

$$Im(G_{x,x\prime}) = \lim_{\eta\to 0} \sum_a \langle x|\psi_a\rangle \frac{-\eta}{(E-\epsilon_a)^2 + \eta^2} \langle \psi_a|x\prime\rangle, \tag{2.2.5}$$

for $x = x\prime$

$$Im(G_{x,x}) = \lim_{\eta\to 0} \sum_a \langle x|\psi_a\rangle \frac{-\eta}{(E-\epsilon_a)^2 + \eta^2} \langle \psi_a|x\rangle, \tag{2.2.6}$$

and using the definition of Dirac delta function

$$\delta(x) = \frac{1}{\pi} \lim_{a\to 0} \frac{a}{x^2 + a^2} \tag{2.2.7}$$

We can write the local density of states, $\rho_x(E)$ as

$$\rho_x(E) = \frac{1}{\pi} Im(G_{xx}) = -\sum_a \langle x|\psi_a\rangle^2 \delta(E - \epsilon_a) \tag{2.2.8}$$

Eq. 2.2.8 is the defination of the local density of states(LDOS) at site x. Summing over x, gives the total density of states. For that we can write

$$\rho_{total}(E) = \frac{1}{\pi} \sum_x Im(\hat{G}_{xx}) = -\sum_x \sum_a \langle x|\psi_a\rangle^2 \delta(E - \epsilon_a) = -\frac{1}{\pi} Im(Tr(\hat{G})) \tag{2.2.9}$$

where "Tr" represents the trace operator. Density of states is a fundamental quantity in condensed matter physics and can be used to express many important properties such as number of particles, total energy, conductivity among others.

2.3 DYSON EQUATION

In the previous section we showed how DOS are closely connected to the GF of a system. In case of unperturbed (translational-invariant) systems GF formalism prescribed before is valid. Using Bloch theorem we can derive $|\psi_a\rangle$ of the system with the knowledge of eigenstates $|\psi_a\rangle$. However, translational invariance is broken when impurity (perturbation) is introduced to the system. In that case Bloch wavevectors are no longer the eigenvectors of system. There are two ways to obtain the GF of perturbed system, either by diagonalizing the new Hamiltonian or using Dyson equation [85–87]. Dyson equation provides a more intuitive and simpler way to find the GF of the perturbed system with relatively easy rearrangement of Eq.2.1.5.

Let's assume that we have $\hat{G_0}$ defined for unperturbed Hamiltonian $\hat{H_0}$ as,

$$\hat{G_0} = ((E + i\eta)\hat{I} - \hat{H_0})^{-1} \tag{2.3.1}$$

For perturbation $\hat{V}$ we can write the new Hamiltonian as $\hat{H} = \hat{H_0} + \hat{V}$. The corresponding GF are given as,

$$\begin{aligned} \hat{G} &= ((E + i\eta)\hat{I} - \hat{H})^{-1} \\ &= ((E + i\eta)\hat{I} - (\hat{H_0} + \hat{V}))^{-1} \\ &= (\hat{G_0}^{-1} - \hat{V})^{-1} \end{aligned} \tag{2.3.2}$$

Solving Eq. 2.3.2, we can write,

$$\hat{G} = \hat{G_0} + \hat{G_0}\hat{V}\hat{G} \tag{2.3.3}$$

Above equation allows us to write the perturbed GF $\hat{G}$ in terms of its unperturbed part ($\hat{G_0}$) and the perturbation (V). This form of Dyson equation is still not very useful to many applications as the unknown perturbed GF term is on the RHS also. There are a few different ways, we can tackle this problem,

1. We can expand the Eq.2.3.3 as

$$\hat{G} = \hat{G}_0 + \hat{G}_0\hat{V}\hat{G}_0 + \hat{G}_0\hat{G}\hat{G}_0\hat{G}\hat{G}_0 + ... \tag{2.3.4}$$

For a weak perturbation $\hat{V}$ we can discard the higher order terms and calculate perturbed $\hat{G}$ from the unperturbed $\hat{G_0}$ and $\hat{V}$ directly.

2. With slight rearrangement of the terms in Eq.2.3.2 we can write

$$\hat{G} = (\hat{I} - \hat{G}_0\hat{V})^{-1}\hat{G}_0 \tag{2.3.5}$$

Using Eq.2.3.3 we can write,

$$\hat{G} = \hat{G}_0 + \hat{G}_0\hat{V}(\hat{I} - \hat{G}_0\hat{V})^{-1}\hat{G}_0 \tag{2.3.6}$$

We can now write this in terms of T-matrix as $\hat{T} = \hat{V}(\hat{I} - \hat{G}_0\hat{V})^{-1}$

$$\hat{G} = \hat{G}_0 + \hat{G}_0\hat{T}\hat{G}_0 \tag{2.3.7}$$

This allows us to define perturbed GF in terms of $\hat{V}$ and $\hat{G_0}$ without putting any constraints on it.

Dyson equation is built around describing a system in terms of host material and the perturbation which can be substitutional impurity, an adatom, or combination of different systems. In the next two subsection we will demonstrate how Dyson equation provides necessary tools to calculate GF for

1. A substitutional impurity embedded in a linear chain of atoms.
2. A linear chain of atoms, *i.e.* GF of the host material using a recursive technique,

This will be useful in the subsequent calculations and the method will be expanded to describe disordered 2-D materials.

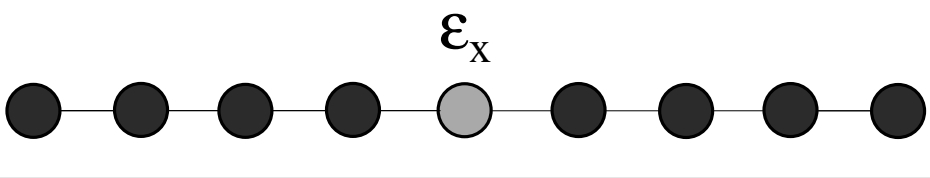

Figure 2.1: A substitutional impurity at site x labelled with different onsite energy ϵ_x.

2.3.1 *Substitutional Impurity*

Modelling substitutional impurity involves replacing a host site atom with another element. We can model this by changing the on-site energy term describing the relevant orbital at a particular site. The energy orbitals of the substitutional impurity atom differs from the host system as shown in Fig. 2.1. We can also modify the hopping integral terms between host and impurity, however in the first approximation we assume that there are no fluctuations in hopping integral terms in the system and a single orbital on the impurity atom.

We can define the perturbation as

$$V = |x\rangle \epsilon_{imp} \langle x| = |x\rangle (\epsilon_x - \epsilon_0) \langle x| \tag{2.3.8}$$

where, $\epsilon_{imp} = \epsilon_x - \epsilon_0$, and ϵ_x and ϵ_0 are the onsite energies of the substitutional atom and host site respectively. We can now use Dyson equation to obtain GF of the perturbed system. From Eq. 2.3.3 we can write

$$G_{a,b} = g_{a,b} + g_{a,x} V_{x,x} G_{x,b} \tag{2.3.9}$$

where g_{ab} is the pristine GF (unperturbed GF), defined for the indices a and b. Using Dyson equation again we can write

$$G_{x,b} = g_{x,b} + g_{x,x} V_{x,x} G_{x,b} = \frac{g_{x,b}}{1 - g_{xx}\epsilon_x} \tag{2.3.10}$$

Combining Eq. 2.3.9 and Eq. 2.3.10, we can write,

$$G_{a,b} = g_{a,b} + \frac{g_{a,x}\epsilon_x g_{x,b}}{1 - g_{x,x}\epsilon_x} = g_{a,b} + g_{a,x}T_{x,x}g_{x,b} \tag{2.3.11}$$

Where $T_{x,x} = \frac{\epsilon_x}{1-g_{xx}\epsilon_x}$. This allows us to describe the propagation of electrons between atoms a and b in the presence of substitutional impurity at x^{th} site. Note that here $g_{a,b}$ describe the propagation of electrons from site a and b of an unperturbed system. Scattering caused by of the substitutional impurity is given by the second term of the equation. In order to calculate the local density of states at the impurity site we can write,

$$G_{x,x} = g_{x,x} + \frac{g_{x,x}\epsilon_x g_{x,x}}{1 - g_{x,x}\epsilon_x} = \frac{g_{xx}}{1 - g_{x,x}\epsilon_x} \tag{2.3.12}$$

In this thesis we will often deal with systems with more than one impurity. We can extend the use of Dyson equation to define a system with more than one impurity. In case of two substitutional impurities placed at site "x" and "y", we can define the perturbation as

$$V = |x\rangle\delta_x\langle x| + |y\rangle\delta_y\langle y| \tag{2.3.13}$$

For an ensemble, N of such impurities we can write

$$V = \sum_{x\in N} |x\rangle\delta_x\langle x| \tag{2.3.14}$$

From Dyson equation we can write

$$G_{a,b} = g_{a,b} + \sum_{x\in N} g_{a,x}\delta_x G_{x,b} \tag{2.3.15}$$

Expressing $G_{x,b}$ like before we can write,

$$G_{x,b} = g_{x,b} + \sum_{y\neq x\in N} g_{xy}\delta_y G_{y,b} \tag{2.3.16}$$

Substituting back we can write

$$G_{a,b} = g_{a,b} + \sum_{x\in N} g_{a,x}\delta_x G_{x,b} + \sum_{x\in N}\sum_{y\neq x} g_{a,x}\delta_x g_{x,y}\delta_y G_{y,b} \tag{2.3.17}$$

Repeating the procedure of expanding $G_{y,b}$ for N scatterers until we can write the perturbed GF only in terms of unperturbed GF and onsite energies of the scatterers. It is obvious the method gets very complex with increase in the number of scatterers in the system. To get better understanding of the scattering properties we can also use the T-matrix. We can write T matrix as $T = V(I - gV)^{-1}$. Expanding in second term as a power series we can now write,

$$T = V + VgV + VgVgV + VgVgVgV + ... \tag{2.3.18}$$

In terms of single impurity T matrix we can write,

$$t_x = |x\rangle t_{xx}\langle x| = |x\rangle \frac{\delta_x}{1 - g_{xx}\delta_x}\langle x| \tag{2.3.19}$$

Using Eq. 2.3.18 and Eq. 2.3.19 we can write

$$T = \sum_{x\in N} t_x + \sum_{x\in N}\sum_{y\neq x} t_c g t_y + \sum_{x\in N}\sum_{y\neq x}\sum_{z\neq y} t_x g t_y g t_z + ... \tag{2.3.20}$$

The GF takes following form

$$G_{ab} = g_{ab} + \sum_{x\in N} g_{a,x}t_{aa}g_{x,b} + \sum_{x\in N}\sum_{y\neq x} g_{ax}t_{xx}g_{xy}t_{yy}g_{yb} + \sum_{x\in N}\sum_{y\neq x}\sum_{z\neq y} g_{ax}t_{xx}g_{xy}t_{yy}g_{yz}t_{zz}g_{zb} + ... \tag{2.3.21}$$

This shows that the scattering due to N impurities is not only sum of single scatterer effects but also consists of the higher order terms which are responsible for the multiple scattering events. These terms corresponds to the different propagation of electrons from one site to another. As we shall see in this thesis multiple scattering indeed plays a big role in the electronic transport properties. It is important to note

that Eq. 2.3.21 gives the exact GF of a perturbed system. However, it is evident that using these methods to study the realistic systems is extremely difficult and computationally expensive as higher order terms in Eq. 2.3.21 describes multiple scattering events. Such events play significant role in scattering phenomenons. Thus it is necessary to construct the system in such a way that we can extract necessary GF without dealing with infinite terms. In the following section, we introduce recursive GF technique which uses the effective dyson equation and allows us build the system in a piecewise fashion.

2.4 RECURSIVE ALGORITHM

In the previous sections we introduced the Green's Functions and Dyson equation. For a given Hamiltonian $\hat{H}$, we can write $\hat{G} = ((E + i\eta)\hat{I} - \hat{H})^{-1}$. This definition requires the direct inversion of the entire Hamiltonian matrix. However, the computational cost and difficulty increases with the order of matrix and size of the system as $O(n^3)$ where n are number of orbitals considered describing the system. For periodic systems, we can use Bloch functions technique to simplify the problem through integration in k-space. This technique states the eigenfunctions in for a system with periodic potential as $\psi(x) = e^{ikx}u_k(x)$, where k is wavevector and $u_k(x)$ defines the periodicity of the system. Introduction of random disorders is detrimental to this procedure thus an alternative approach is necessary. To model the transport properties of large periodic system with and without perturbation, we can use Dyson equation recursively to derive the necessary GF. The recursive method builds the system in a piecewise fashion and allows us to calculate only the necessary GF reducing computational memory costs [88, 89]. Each piece added to the system needs not to be exactly the same as Dyson equation generates perturbed GF of the system with the knowledge of perturbation. As a result recursive techniques offers great deal of advantage over Bloch function technique for disordered systems [80, 90]. In the next subsection we introduce a standard recursive approach.

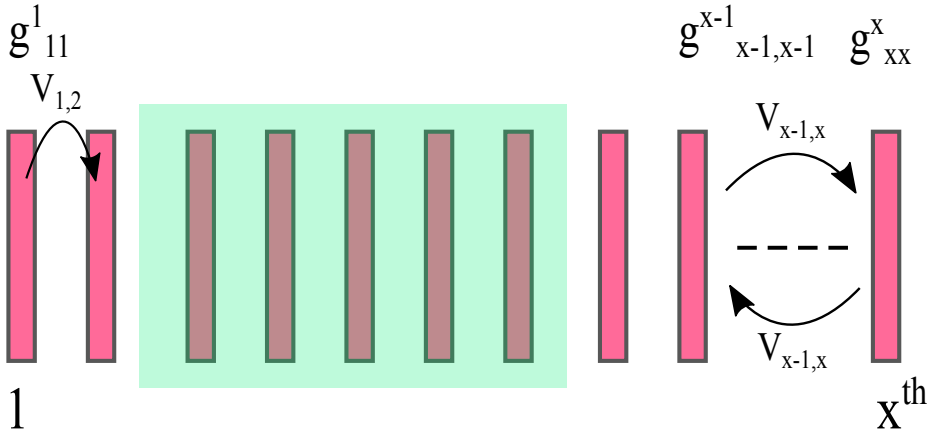

Figure 2.2: Standard recursive technique resolves the material in slices from 1 to x. g^x_{xx} is the GF of a connected system after x iterations. $V_{x,x+1}$ is the connection matrix between corresponding slices.

2.4.1 *Standard recursive approach*

To define the recursive approach we assume that the system is composed of i individual slices. Each slice consisting of n_i orbital atoms, *i.e* n atoms constructing the slice. Fig. 2.2 provides a schematic illustration of how the recursive method works. Recursive algorithm considers a region where connected slices are next to a slice that is disconnected from the rest. The act of connecting these parts corresponds to the perturbation potential V. This enables us to describe a disordered system by simply using Dyson equation repeatedly. Let's define the necessary GF: $g^x_{x,x}$ is the GF of the x^{th} slice of the connected system as where x indicates the position of unit cell and $g_{x,x}$ is the GF of isolated x^{th} slice.

It is important to note that $g_{x,x}$ is a matrix of size $n_i \times n_i$ containing all GF describing the isolated x^{th} slice. To maintain the generality we do not restrict the unit cells to be identical. Each unit cell can consist of different number and type of atoms. $V_{x,x+1}$ and $V_{x+1,x}$ describes the hopping parameter connecting x^{th} and $x+1^{th}$ unit cells. In case of different dimensionality of x^{th} unit cell the connection matrix takes the dimensions $n_x \times n_{x+1}$ so $V_{x,x+1}$ is not necessarily square. Recursive approach starts with unit cell labelled $x = 1$ and connects following slices one after

another with the help of Dyson equation. We initialise the algorithm at x^{th} slice. Dyson equation defines GF of the x^{th} slice as,

$$g^x_{x,x} = g_{x,x} + g_{x,x} V_{x,x-1} g^x_{x-1,x} \tag{2.4.1}$$

Using Dyson equation we can write,

$$g^x_{x-1,x} = g^{x-1}_{x-1,x-1} V_{x-1,x} g^x_{x,x} \tag{2.4.2}$$

Combining Eq. 2.4.1 and Eq. 2.4.2, we can write

$$g^x_{x,x} = (I - g_{x,x} V_{x,x-1} g^{x-1}_{x-1,x-1} V_{x-1,x})^{-1} g_{x,x}, \tag{2.4.3}$$

With a small rearrangement ,

$$g^x_{x-1,x-1} = (I - g^{x-1}_{x-1,x-1} V_{x-1,x} g_{xx} V_{x,x-1})^{-1} g^{x-1}_{x-1,x-1} \tag{2.4.4}$$

In transport calculations for a simple two terminal setup as shown in Fig. 2.2, device is connected with two semi-infinite leads. Surface GF of a lead defines the possible channels available for the transport of electrons through a quantum device. We can calculate the surface GF of the semi-infinite lead using Eq. 2.4.3 for $x \to \infty$. Numerically, a lead may be considered semi-infinite if there is no change in the total density of states,

$$Tr(Im[g^{x-1}_{x-1,x-1}]) \approx Tr(Im[g^x_{x,x}]). \tag{2.4.5}$$

Eq. 2.4.4 allows to connect two semi-infinite leads to obtain GF of the infinite system.

$$G_I = (I - G_R . V_{RL} G_L . V_{LR})^{-1} G_R \tag{2.4.6}$$

$G_{L/R}$ are the surface GF of the semi-infinite systems.

2.5 ELETRONIC TRANSPORT

Conductance of a device of classical dimensions follows Ohm's expansion law as $G = \sigma\frac{W}{L}$, where W and L are the width and length of the device. However, this relation does not remain valid as the size of the system becomes smaller. In the quantum realm conductance does not change linearly as a function of width W and interface resistance is independent of length L. Conductance depends on the number of transverse modes in the system, resulting in the discrete changes in the transmission function. Landauer formula defines the conductance on the basis of number of transmission modes. We can write the conductance and current flowing through the device attached between two leads at electrochemical potentials μ_1 and μ_2 as

$$G = \frac{2e^2}{h}M\bar{T}, \tag{2.5.1}$$

Here, M are the number of transverse modes and $\bar{T}$ is the average probability that an electron injected from the left lead transmits to the right lead. At zero temperature current flows completely between the leads with electrochemical potential μ_1 to μ_2. We can write the current flowing between leads L_1 and L_2 as

$$I = \frac{2e}{h}MT[\mu_1 - \mu_2] \tag{2.5.2}$$

Eq. 2.5.1 is defined at the zero temperature so that the transport takes place only from the left lead to the right not from the right lead to the left lead. The Current, carried by the single energy channel around the Fermi energy is defined as

$$I(E) = \frac{2e}{h}M(E)T(E)[f_1(E) - f_2(E)] \tag{2.5.3}$$

$f_1(E)$ and $f_2(E)$ are the Fermi functions associated with leads L_1 and L_2 such that

$$f(E) = \frac{1}{exp^{\frac{(E-\mu)}{k_B T}} + 1} \tag{2.5.4}$$

For $M_2(E) = M_1(E)$, we can write Eq. 2.5.1. However, in the linear response regime both contacts are at the same electrochemical potentials, *i.e.* $\mu_1 = \mu_2$. For this, the equilibrium state current becomes proportional to the applied bias. That allows us to write,

$$\delta I = \frac{2e}{h} \int ([\bar{T}_{equ}(E)]\delta[f_1 - f_2] + [f_1 - f_2]_{equ}\delta[\bar{T}(E)])dE \tag{2.5.5}$$

Second term $= 0$, and expanding the first term we can write the conductance of a system as

$$G = \frac{2e^2}{h} \int \bar{T}(E)(\frac{\delta f_0}{\delta E})dE \tag{2.5.6}$$

where $\bar{T}(E) = M(E)T(E)$. Using Fisher-Lee relation we can define the transmission function as [91],

$$T(E) = Tr[\Gamma_L G^R \Gamma_R G^A] \tag{2.5.7}$$

here, "Tr" is the trace of the scattering matrix, $\Gamma_{L,R}$ representing self energy terms of the leads accounting the injection and lifetime of the states in left and right contact. $G^R(G^A)$ are retarded and advanced GF of the connected system. We can calculate these quantities using recursive algorithm detailed in the previous section. We can write the self energy term as

$$\Gamma_{L,R} = i[\Sigma^R_{L,R} - \Sigma^A_{L,R}] \tag{2.5.8}$$

$\Sigma^R_{L,R}$ are the retarded self energy terms of the leads, *i.e.* imaginary part of the surface GF of the leads. $\Sigma^A_{L,R}$ are the hermitian conjugate of the retarded self energy. Note that the most significant contribution to the integral in Eq. 2.5.6 comes from the transmission $\bar{T}(E)$ at energies close to the chemical potential (Fermi level) μ. For that reason, throughout this work we shall use the dimensionless energy-dependent transmission coefficient $\bar{T}(E)$ as a proxy for the conductance between electrodes.

It is important to state that transmission $\bar{T}(E)$ is model independent, once the Hamiltonian is known one can find the corresponding Green function and obtain energy dependent conductance of the system [92]. Büttiker extended Landauer formula for multiterminal set-up. Using the total current conservation we can define it as

$$I_i = \frac{2e}{h} \sum_j [T_{ji}\mu_i - T_{ij}\mu_j] \tag{2.5.9}$$

I_i is the current from lead i summed over terminals j. For $V = \frac{\mu}{e}$ we can write

$$I_i = \sum_j [G_{ji}V_i - G_{ij}V_j] \qquad G_{ij} = \frac{2e^2}{h}\bar{T}_{ij} \qquad \bar{T}(E) = M(E)T(E) \tag{2.5.10}$$

It is important to note that Büttiker formula provides a way to measure the local conductances. Using gauge invariance and current conservation it is possible to describe the conductance matrix G_{ij} created from the different combination of electrodes in the form of R_{ij} and V_{ij}.

2.6 ELECTRONIC STRUCTURE

Greens functions formalism introduced in the previous sections are independent of the electronic structure modelling schemes. Landauer formalism can only capture details of a material in conductance spectra as per the totality of the Hamiltonian used to describe material. Thus capturing the electronic structure accurately is essential in order to model conductance of the system. Tight binding (TB) modelling scheme provides a relatively simple description of the electronic structure of material. Accuracy of TB scheme depends on the overlap between wave functions defined for neighbouring atoms. In TB scheme the wavefunctions are expressed in the combination of localised atomic orbitals. If the overlap is large the TB modelling scheme fails to describe the electronic structure accurately. However, for a simple crystalline lattice structure TB approach provides good description of electronic

distribution. In this work we will use different materials to present the inverse problem with graphene as the main material of interest. It is worth mentioning that the TB model provides an excellent description of graphene based materials.

Graphene, a planer sheet of carbon atoms arranged in a hexagonal lattice structure is shown in Fig. 2.3. The σ bonds are formed between the neighbouring carbon atoms with the sp^2 hybridised orbitals. Three out of four available electrons, *i.e.* hybridised orbitals form in planar bonds with another neighbouring carbon atoms. Electron remaining in the $2p_z$ orbital forms π bonds with other neighbouring carbon atoms giving rise to the energy bands near the Fermi energy. As we shall see graphene is found to be a zero-bandgap material with unique electronic structure where the valance and conduction band connect each other at discrete points. Graphene nanoribbons shows variety of interesting electronic structures depending on the width and the edge structures. In this study, we use transmission signatures of graphene flake and ribbons to define the inverse problem. To do so first we introduce tight binding approach for the graphene and then present transport scheme for Graphene nano-ribbons.

2.6.1 *Tight Binding Model*

We can write the Hamiltonian describing a system as

$$\hat{H} = \sum_i |i\rangle \epsilon_i \langle i| + \sum_{i,j} |i\rangle t_{ij} \langle j| \tag{2.6.1}$$

Here $|i\rangle$ represents atomic orbital centred at lattice site i, and ϵ_i is the onsite energy of the site i. t_{ij} is the hopping integral between the orbitals situated at i to j. In this section, we will derive the dispersion relation for graphene. The unit vectors are given by

$$\hat{a}_1 = \frac{\sqrt{3}}{2} a\hat{x} + \frac{a}{2}\hat{y} \tag{2.6.2}$$

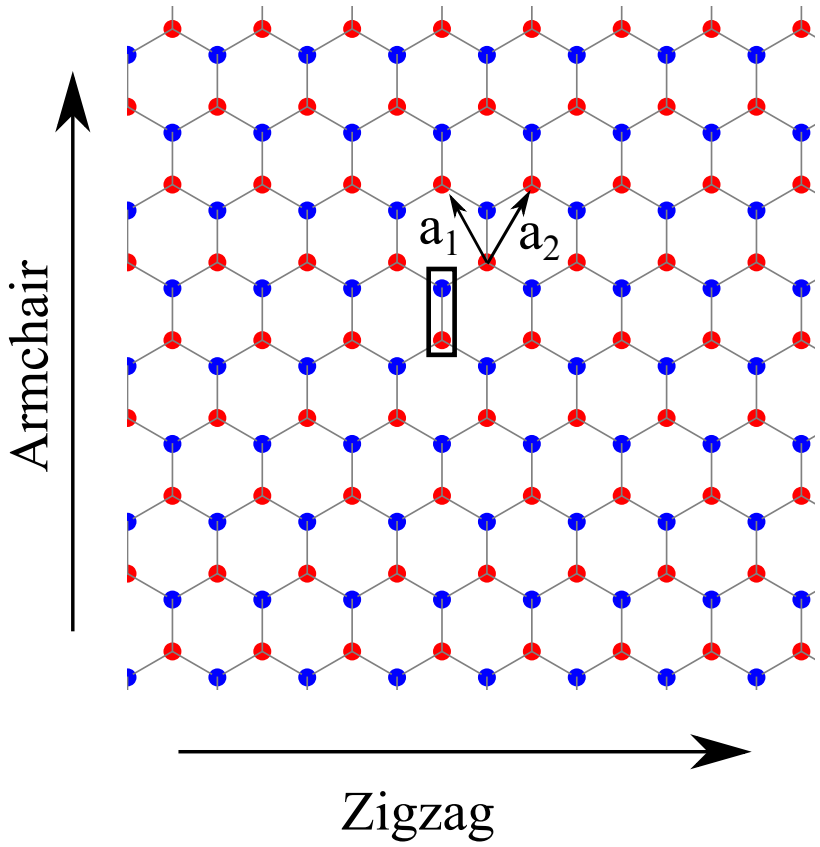

Figure 2.3: A section of the honeycomb graphene. The rectangle encloses a unit cell containing one site from each sub-lattice with lattice vectors $\mathbf{a}_1$ and $\mathbf{a}_2$. The arrows highlights the armchair (A) and zigzag (Z) directions in the lattice.

and

$$\hat{a}_2 = \frac{\sqrt{3}}{2}a\hat{x} - \frac{a}{2}\hat{y} \tag{2.6.3}$$

Reciprocal lattice vectors can be defined as

$$\hat{b}_1 = \frac{2\pi}{\sqrt{3}a}\hat{x} + \frac{2\pi}{a}\hat{y} \tag{2.6.4}$$

$$\hat{b}_2 = \frac{2\pi}{\sqrt{3}a}\hat{x} - \frac{2\pi}{a}\hat{y} \tag{2.6.5}$$

We can define a Bloch function to form the basis in the reciprocal space composed of atomic orbitals with coefficient ϕ^k as

$$|k\rangle = \frac{1}{\sqrt{N}} \sum_j e^{ik\cdot\mathbf{r}_j} \phi^k |j\rangle \tag{2.6.6}$$

Here, r_j is the position vector of the lattice site j. We can find eigenstate using time independent Schrödinger equation,

$$\hat{H}|k\rangle = \epsilon(k)|k\rangle \tag{2.6.7}$$

Projecting this onto different basis we can write

$$\epsilon(k) \sum_j e^{ik\cdot\mathbf{r}_j} \phi^k |j\rangle = \sum_j e^{ik\cdot\mathbf{r}_j} \phi^k H|j\rangle \tag{2.6.8}$$

Taking scalar product with $\langle i|$, we can write,

$$\epsilon(k) \sum_j \langle i|e^{ik\cdot\mathbf{r}_j} \phi^k |j\rangle = \sum_j e^{ik\cdot\mathbf{r}_j} \phi^k \langle i|H|j\rangle \tag{2.6.9}$$

Applying the condition of orthogonality we can write,

$$\epsilon(k)\phi^k = \sum_j e^{ik\cdot(\mathbf{r}_j - \mathbf{r}_i)} \cdot \phi^k \langle i|H|j\rangle \tag{2.6.10}$$

We can solve this for eigenvalues $\epsilon(k)$ and eigenstates $|k\rangle$ using matrix method to solve the eigenvalue problem. Any unit cell can be located using linear combination of $\mathbf{a}_1$ and $\mathbf{a}_2$. We can write $\mathbf{r} = m\mathbf{a}_1 + n\mathbf{a}_2$. The orbital basis set used to calculate electronic structure is denoted by $|r, n\rangle$, where r gives the distance of unit cell and $n = 1, 2$, for blue and red sites respectively. Switching to reciprocal space we can write Bloch waves as

$$|k, n\rangle = \frac{1}{\sqrt{N}} \sum_r e^{ik\cdot r} |r, n\rangle \tag{2.6.11}$$

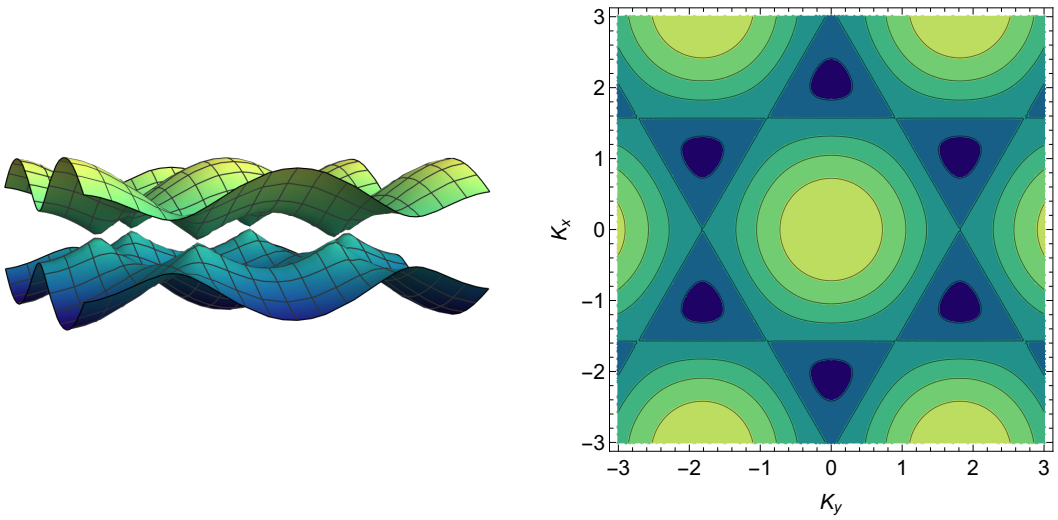

Figure 2.4: Tight binding band structure of graphene along with the Contour plot describing the Fermi surface.

Each atom on the lattice site has three nearest neighbours the hopping probability for nearest neighbours in graphene is known to be $-2.7eV$. For the sake of simplicity, we will assume the onsite potential as zero and hopping integral (t) . We can write the Hamiltonian matrix as

$$H = \begin{pmatrix} 0 & tf(k) \\ tf^{\dagger}(k) & 0 \end{pmatrix} \tag{2.6.12}$$

here, $f(k)$ is calculated by summing over the phase terms coming from nearest neighbouring site. From either red or blue site, we can write

$$f(k) = \sum_{i=1}^{3} e^{ik\cdot\mathbf{r}_i} \tag{2.6.13}$$

$$f(k) = e^{\frac{ik_x a}{3}} + 2e^{\frac{-ik_x a}{2\sqrt{3}}} \cos\frac{k_y a}{2} \tag{2.6.14}$$

To solve the following determinant for the eigenvalues $\epsilon(k)$ we can write,

$$\begin{vmatrix} 0-\epsilon(k) & tf(k) \\ tf^{\dagger}(k) & 0-\epsilon(k) \end{vmatrix} = 0 \tag{2.6.15}$$

we get,

$$\epsilon_{\pm}(k) = \pm t\sqrt{1+4\cos^2(\frac{k_y a}{2})+4\cos(\frac{k_y a}{2})\cos(\frac{\sqrt{3}k_x a}{2})} \tag{2.6.16}$$

This is the dispersion relation for graphene. The corresponding eigenstates are given as

$$|k,\pm\rangle = \frac{1}{\sqrt{2N}}\sum_{r} e^{-ik\cdot e}(|r,1\rangle \pm e^{-i\phi(k)}|r,2\rangle), e^{-i\phi(k)} = \frac{f^{\dagger}(k)}{|f(k)|} \tag{2.6.17}$$

Note that the p_z orbitals in carbon contain one electron, the band is half full. This is where two bands touch and density of states vanishes. Graphene is thus a zero band gap semiconductor or a semi-metal. Many interesting properties belonging to graphene arise due to the shape of the bands near Fermi energy. The band structure near the Fermi energy is linear [93]. This results in electrons and holes having zero effective mass and behaving like relativistic particles which can be described using the Dirac equation from quantum electrodynamics [94].

2.6.2 *GNRs*

Trimming graphene sheet to specific widths gives rise to interesting electronic structure. Ribbons with parallel zigzag edge geometry are metallic in nature whereas armchair edged ribbons are found to be semiconducting. With the help of Landauer formula we can now define the transport properties of graphene ribbons. To do so we need to calculate GF of the relevant system. We present a case study of 9 atom wide armchair edged graphene ribbon(AGNR) and 6 atom wide zig-zag edged graphene nanoribbon(ZGNR) system.

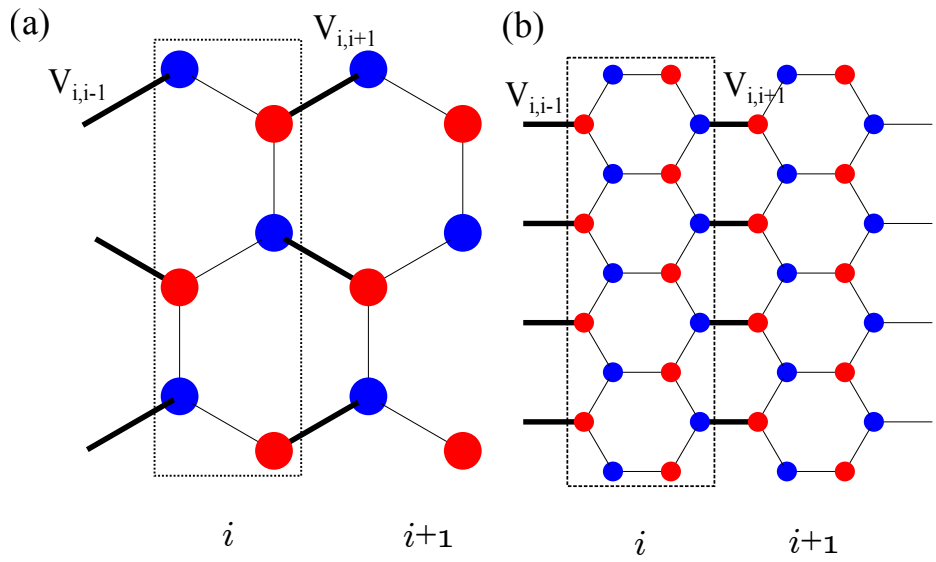

Figure 2.5: Schematic of 7 and 9 atom wide zigzag and armchair edge graphene unitcell respectively. Dark black lines indicates the connection between two unit cells, modelled in matrix V_{ij}.

In AGNR, unit cell consists of two vertical parallel lines with carbon atoms connected at every second place as shown in Fig. 2.5(b). Repeating this structure along the horizontal direction generates the armchair edged nanoribbon system. In case of Zigzag edged nano ribbons(ZGNRs) we follow similar procedure to define the unit cell. However, in this case unitcell consists of a straight line of carbon atoms. The connection matrix maintains bipartite nature of carbon sublattices as shown in Fig. 2.5(a). In such ribbons one type of sublattice on one edge and other sublattice occupies opposite edge. This type of arrangement gives rise to interesting magnetic properties which are not common to the AGNRs [80, 89].

Recursive algorithm uses same approach to calculate GF of full system,*i.e.*, connects one unit cell after another to obtain ribbon. To do so first step is to generate GF for the disconnected unit cell first. Eq. 2.1.5 defines GF of a unit cell as g_{00} as $g_{00} = ((E \pm i\eta)\hat{I} - \hat{H})^{-1}$. In case of 9-AGNR, Hamiltonian is a 18×18 matrix as unit cell consists of 18 atoms as shown in Fig. 2.5(b). Connection matrix $V_{i,i+1}$ and $V_{i,i-1}$ defines the connections between i^{th} cell with its adjacent cells such that $V_{i,i+1} = V_{i,i-1}$. Hamiltonian for 6 atom wide ZGNR unit cell takes the similar form.

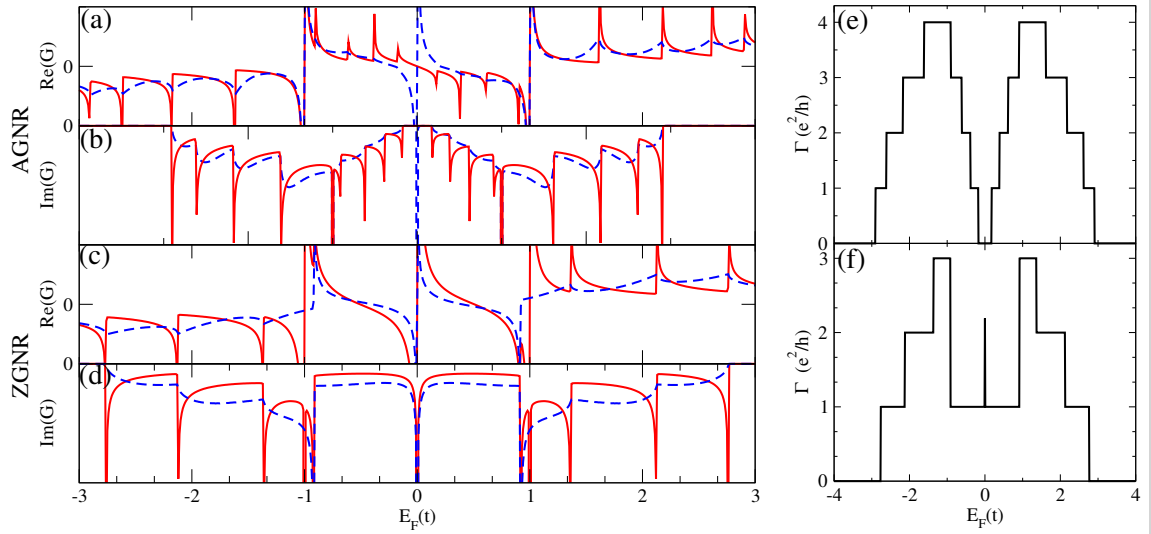

Figure 2.6: Left column shows real and imaginary part of the surface greens functions of semi-infinite system (Dashed blue) and Infinite system (Red) for 6-ZGNR and 9-AGNR systems. Panels (e) and (f) shows the transmission coefficients of 9-AGNR and 6-ZGNR respectively.

However connection matrix $V_{i,i+1}$ and $V_{i,i-1}$ are not identical but complex conjugate of one another, $V_{i,i+1} = V^{\dagger}_{i-1,i}$.

Using recursive algorithm and Eq. 2.4.4 we can calculate the surface GF of leads. Connecting semi-infinite leads to one another using Dyson equation allows us to model an infinite system. In Fig. 2.6(a), real part of the surface GF of semi-infinite and infinite armchair nanoribbon system is plotted in blue and red colour respectively. DOS of leads indicates the number of modes injected in the device at a particular energy. Panel (b) depicts the imaginary part, *i.e.* DOS of semi-infinite and infinite systems again in blue and red curves respectively. Similarly, panels (c) and (d) depicts the real and imaginary parts of the surface GFs of 6-atom wide zig-zag edged graphene nanoribbon systems. Blue dashed line plotted as a function of energy corresponds to semi-infinite system. In the right column, transmission coefficient is plotted as a function of energy for AGNR and ZGNR systems in panel (e) and panel (f) respectively. The transmission steps can be easily understood from the energy dispersion relation of graphene in infinite ribbons [95]. It basically is the number of bands crossing the Fermi energy E. Just looking at

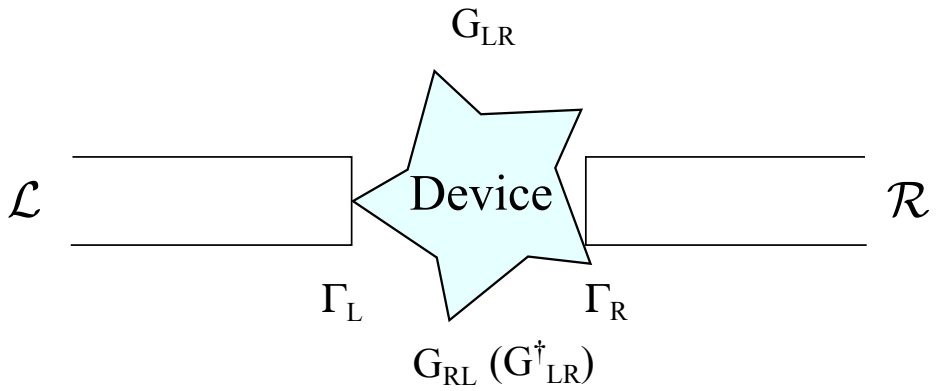

Figure 2.7: A standard two terminal set-up for transport measurement. Leads $\mathcal{L}$ and $\mathcal{R}$ are connected to the device at centre.

transmission signatures and density of states we can extract valuable information about the underlying system. Note that in panel (d) the density of states for zigzag edged infinite graphene nanoribbon system shows sharp dip at $E = 0$, and it changes drastically as we move away from $E = 0$. In panel (f), this translate into the transmission coefficient. At $E = 0$ most of the current transmits mainly from the edge states. In armchair case presented in panel (e), current transmits mainly through the bulk and bandgap is translated into the zero transmission region near $E = 0$.

2.7 SUMMARY

This chapter introduces basic mathematical infrastructure needed to define the transport problem considered in this thesis, namely the electronic transport calculations. The GF formalism is model independent and capable of handling very general systems, both ordered and disordered. Flexibility of the formalism can be used very eloquently to describe the perturbed and unperturbed systems with the help of Dyson equation as presented in sections 2.3 and 2.3.1.As a result, this formalism is ideal to describe numerous properties of the disordered structures. We define the inverse problem with the help of transmission signature of devices. The Landauer

formula introduced in section 2.5 uses the GF quantities of the perturbed systems to calculate transmission. We can summarise the algorithm as below

1. Connect leads to the left and right side of the device as shown in Fig. 2.7. Surface GF of leads are defined using the recursive algorithm. $\Gamma_{L/R}$ are the line width functions of the leads.

2. Calculate GF using recursive algorithm by connecting slices of the deviceto the left lead and then attaching to the right lead, G_{LR} and G_{RL}.

3. Calculate transmission of system using Landauer formula $\bar{T}(E) = Tr[\Gamma_L(E)G^R(E)\Gamma_R(E)G^A(E)]$.

Finally we briefly implement these techniques for graphene nanoribbons in section 2.6.2. In the next chapter we will use these modelling techniques to define the inverse problem using the transmission spectra of a device.

3

DISORDER INFORMATION FROM CONDUCTANCE SIGNATURE

3.1 INTRODUCTION

Ability to manipulate the surroundings to achieve a desired functionality is the basis of human engineering nature. Modelling, Fabrication and Characterization are the three basic stages of any engineering processes. Ever increasing complexity demands advancements in these interlinked stages. Modelling a system requires understanding of the causal elements that constitute together to generate desired result. It can be characterized in two ways (1) Forward and (2) Inverse modelling schemes. Forward modelling (FM) techniques use this information to derive subsequent effects for defined processes. In condensed matter physics, most of the problems consists of solving Schrödinger's equation in one form or another. For example, to derive the wavefunction of an electron in a 1-D potential well we can write the wave-equation as,

$$-\frac{\hbar^2}{2m}\frac{d^2\psi}{dx^2} + V(x)\psi = E\psi \tag{3.1.1}$$

In equation 3.1.1, ψ is the wave-function, $V(x)$ defines the potential along x and E is the eigenenergy of electron. Forward method revolves around deriving the wave-function ψ (effect) for potential well $V(x)$ (cause). Whereas, Inverse modelling (IM) uses the effect to extract information about the underlying causal factors ($V(x)$). In quantum mechanics such problems are mainly defined to understand the precise Hamiltonian of the system. A forward modelling scheme consists of solving the Schrödinger equation with Hamiltonian containing multiple parameters until the

solution closely matches with the effect. Because of such a large variance in the phase space finding correct parameters can be computationally expensive. Advances in high-performance computing and optimization algorithms are available to decode the parameter phase space in electronic structure problems. However these are large scale simulations that generate volumes of data thus they can be less intuitive to implement.

As stated in Chapter 1, we define the inverse problem (IP) for quantum devices using transmission signatures. A significant portion of electronic structure community is well versed with the Greens function based methods to calculate the transport properties of materials. Electronic transport through nanodevices has been studied extensively over the last three decades. Adding disorders to a material is an effective technique to manipulate the electronic structure of the material. Position, concentration and type of dopants gives rise to unique transmission spectra. The conductance fluctuations contain very little system specific informations. Depending on the disorder they can even have a universal character. A number of studies shows that defining IP for such devices can be very tricky for pristine materials. Disorder makes description of the problem extremely complex even for 1D systems. The aim of this chapter is to introduce a mathematically transparent inversion technique capable of extracting fundamental information about the underlying Hamiltonian by looking at its energy dependent transmission signatures.

The chapter is structured as follows: To begin with we introduce the inversion technique for a variety of materials using a traditional two terminal transport set-up. In subsequent sections we test the flexibility of this methodology for more than one degree of freedom and realistic Hamiltonians calculated using Density Functional Theory (DFT). The chapter is concluded with the error analysis of the inversion technique.

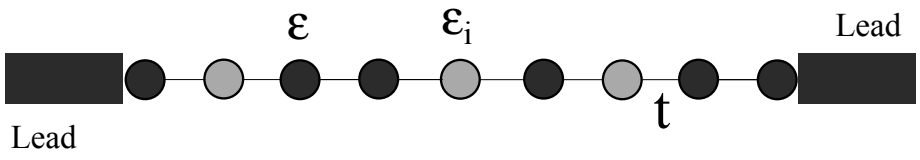

Figure 3.1: Schematic representation of two-terminal setup with a device sandwiched between two leads. In case of 1-D system black(gray) sites represents host(disorder) material with on-site potential $\epsilon(\epsilon_i)$. Hopping between two sites is t . In 2D devices each site represents a unit-cell describing the host material and disorders attached to it.

3.2 FORWARD MODELLING

The setup to implement the inversion methodology presented in this work can be very easily realised with current nanoscale fabrication techniques. Multiterminal experiments have played a key role in understanding of the electronic transport properties for a variety of materials. Landauer-Büttiker (L-B) formalism approach is commonly used to derive electronic conductance of a two terminal and multi-terminal systems. Kubo formalism is another way to derive the transmission of the device. It can be shown that in DC case the Kubo and L-B formalism are equivalent [92]. For two terminal systems Kubo technique is computationally less costly as it only requires to store the surface GF of two adjacent layers of the device. For this chapter we focus on two terminal devices as shown in Fig. 3.1, system consists of two electrodes connected to the scattering region, *i.e.* device. We can write the Kubo formula as

$$\Gamma(E_f) = \frac{4e^2}{h} Tr(G_{ii} V_{ij} G_{jj} V_{ji} - V_{ij} G_{ji} V_{ij} G_{ji}) \tag{3.2.1}$$

Where, $G_{ij} = \frac{1}{2i}(G^R_{ij} - G^A_{ij})$ and $G^R(G^A)$ are retarded and advanced GF respectively, i and j indicates two arbitrary but adjacent layers of the system derived at Fermi energy [77].

Modern fabrication methods allow great control over the addition of disorders to a material. Different characterization techniques are in place to investigate properties

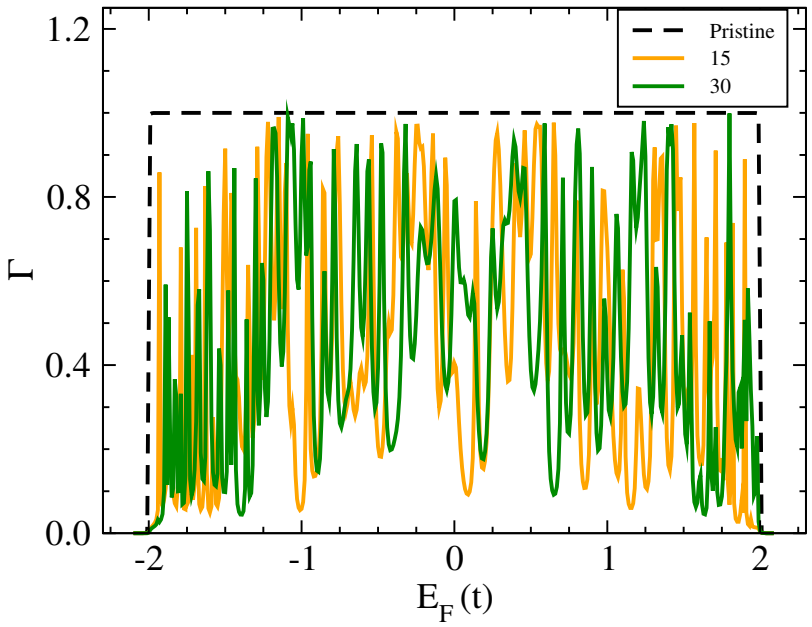

Figure 3.2: Transmission spectrums are plotted in Orange and green colour for one dimensional 100 atoms wide systems with randomly distributed N = 15 and N = 30 number of impurities respectively. Black dashed line shows the pristine case transmission signature of the same system, *i.e.* in the absence of impurities.

of such devices. One of the properties that is particular to our interest is the electronic transport *i.e.* conductance of disordered systems. From experimental point of view, traditional hall bar set-up can be used to observe conductance of the system and from computational modelling perspective once the underlying Hamiltonian is fully specified it is an easy task to derive the energy or gate voltage dependent conductance of the system. In this work we introduce the inversion methodology by using the latter as a proxy for the former, *i.e.* calculated transmission signature representing their experimental equivalent.

The expression for transmission in both Eq. 3.2.1 is model independent. Once the Hamiltonian is known we can calculate the necessary GF and derive the energy dependent transmission. First we focus on system with relatively simple electronic structure. Fig. 3.1 illustrates a typical two terminal setup with linear chain of atoms as a system with hopping t , onsite potentials of host (disorder) site $\epsilon(\epsilon_i)$ and length L. For simplicity we will consider substitutional type of disorders in the system. It is worth mentioning that disorders in the form of adatoms can also be considered in

the Hamiltonian without any fundamental changes in our approach. We can write tight binding Hamiltonian of such system as

$$\hat{H} = \sum_i (|i\rangle t\langle i+1| + |i\rangle t\langle i-1| + |i\rangle \epsilon\langle i|) + \sum_j |j\rangle \epsilon_i \langle j|, \tag{3.2.2}$$

where i and j are integers labelling the atomic sites, $|i\rangle$ represents electronic orbital centred at site i with onsite potential ϵ and t is the hopping integral between nearest neighbour sites only. ϵ_j represents the onsite potential of an impurity site located at j. We assume the hopping term between impurity site and parent material is same as the inter-material hopping.

1-D system presented in the Fig. 3.1 can be described as an infinitely long host containing N randomly distributed impurities confined to a finite sized region. For a device size $L = 100$, *i.e.* 100 atoms defining the scattering region. A fixed number of impurities are randomly distributed in the system. It is important to note that while defining the Hamiltonian exact location and number of disorders is required. Fig. 3.2 depicts transmission spectra of one such configuration with 15 impurities in green colour. Dashed black line signature shows the transmission coefficient of pristine case and in orange another signature with 30 randomly distributed impurities in the system. The task in hand is to extract fundamental information about the underlying Hamiltonian of the device. Only looking at input spectra reconstruction of $\Gamma(E)$ using forward modelling requires guessing the concentration(N), onsite potential and position of disorders. This brute force approach is not viable as the number of configurations required to analyse are too large for practical purposes.

Transmission spectra is a result of complex scattering processes which are strongly dependent on the position of disorders. Extracting exact spatial mapping of disorders is a very difficult task even with the existing computational techniques. However it is possible extract concentration and other properties of disorders. To do so we use forward modelling to realise as many disorder configurations as possible to derive the average transmission of the system.

3.2.1 *Configurational Average*

We define the configurational average (CA) transmission as the average over M different configurations with the same concentration(n) and type of disorders(ϵ) present in the device. It is important to note that every configuration used is unique in the location the of scattering centres. We can write

$$\langle \Gamma(E, n, \epsilon) \rangle = \frac{1}{M} \sum_{j=1}^{M} \Gamma_j(E) \tag{3.2.3}$$

Where, j labels the different configurations. M is the number of realizations used with disorder concentration n with onsite potential ϵ. Throughout this work we will use concentration in forms of N of impurities as the total number and n is the concentration of disorders defined as $n = 100 \times \frac{N}{N_{Total}}$, N_{Total} is the total number of atoms in the device. Throughout this work we will use concentration n and number N interchangeably.

A simple combinatorial analysis shows that the possible number of configurations that a fixed number of disorders can take in the device are very large. For example in case of 1-D system of 100 sites 10 disorders can arrange themselves in 1.7×10^{13} ways. Fluctuations in $\langle \Gamma(E, n, \epsilon) \rangle$ depends on the choice of M. With increase in the number of M fluctuations corresponding to the average decreases. In case of strong disorders, a large number of configurations are required to obtain statistically accurate averages. However, in case of weak disorders, universal conductance fluctuations allows us to obtain accurate results for $\langle \Gamma(E, n, \epsilon) \rangle$ at modest values. Universal conductance fluctuations (UCF) are characteristic of metals and at low temperatures are of order e^2/h. These fluctuations are a result of quantum interference when inelastic diffusion length is larger than the device size. UCF fingerprints are visible in ballistic, diffusive and chaotic systems [96–98]. Lee *et. al* [97] reported that the UCF are independent from the degree of impurities present in the system and device size at zero temperature. To bring the degree of fluctuations to an acceptable level the number of configurations required are in the order of 10^3. It is important to

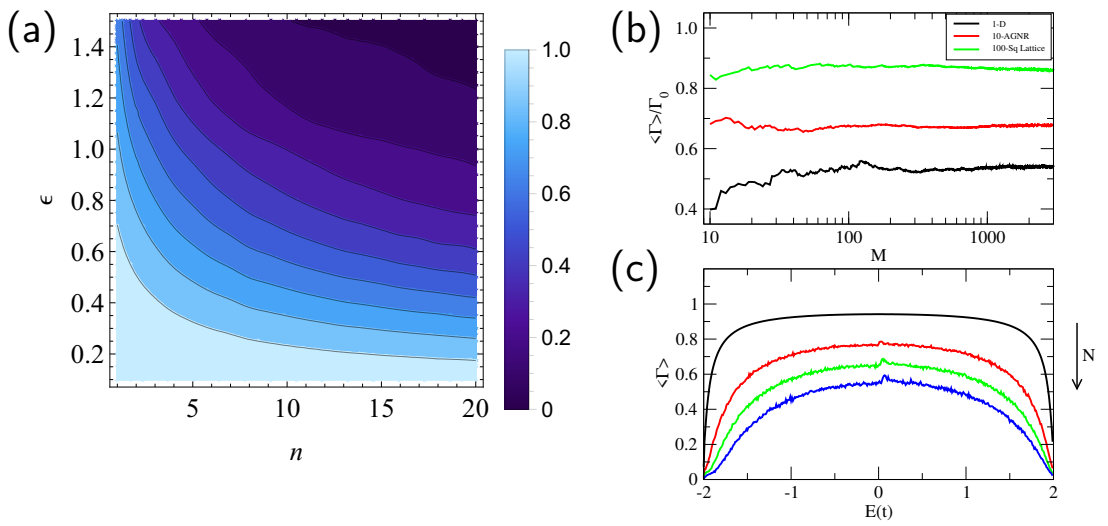

Figure 3.3: (a)2-D contour plot of configurational averaged transmission for linear chain system of size 100 atoms as a function of concentration N and strength ϵ of disorders. Panel(b) shows the number of configurations required to converge configurational average for different system sizes. Black curve depicting the ca for 1D system requires large number of configurational space than other quasi-1D systems, Γ_0 is pristine case transmission.(c) Configurational average transmission of 1D system with different concentration of disorders. As disorder concentration increases the average transmission drops exponentially.

note that the dimensionality of system plays vital role in the choice of M. One dimensional system with corresponding smaller mean dimensionless transmission require higher number of configurations to achieve required statistical significance [99, 100]. In case of 2-D systems, with larger mean transmission coefficients number M drops down with increase in the width of ribbon due to the self-averaging effects.

The CA transmission in Eq. 3.2.3 is defined using the concentration n and strength of the disorder encoded in on site potential ϵ_{imp}. Kubo formula defined in Eq. 3.2.1 depends on the Green Function of device encoding the concentration and properties of disorders in the transmission signature. Note that transmission fluctuations at a certain energy contain very little system specific information however the mean directly depends on the concentration and strength of disorders. Introduction of disorders leads to transmission suppression and changes in the electronic structure of the material. In case of 1-D systems in diffusive regime interference between scatterers leads to the compression of transmission. Fig. 3.3 depicts changes in the

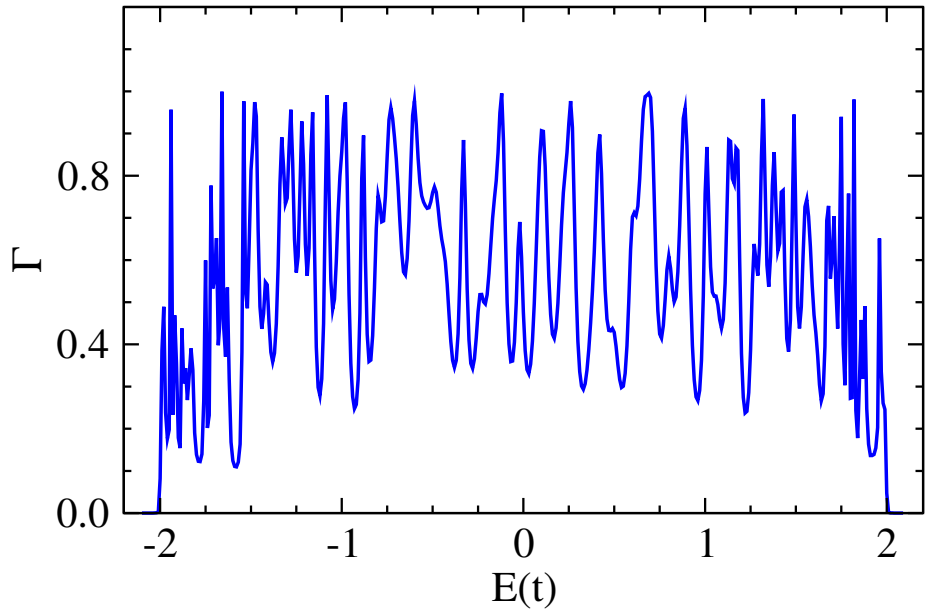

Figure 3.4: Transmission spectra calculated for a system of linear chain of 100 atoms with $N = 10$ impurities randomly distributed in the system.

average transmission due to introduction of scatterers in the system at $E_f = 0$ and $t = 1$. This is a brute force technique and there are a few machine learning based techniques to accelerate the derivation of CA [101, 102]. Alternatively, Coherent phase approximation (CPA) technique replaces the disorder concentration with effective medium can be used to obtain CA transmission spectra upto certain degree of accuracy [103]. CPA with Vertex correction is more accurate but effective for low concentration of disorders in the system. We use a simple interpolation technique presented in the Appendix (I) to calculate the CA for smaller increment in concentration. In the next sections we introduce basic elements of the inversion technique.

3.3 INVERSION TECHNIQUE

In the previous section, we derived the configurational average transmission of 1-D system. These are quantum features found by solving the Schrödinger equation once the system Hamiltonian is known. To define the inversion technique, we

introduce a system with N randomly distributed substitutional impurities in 1-D chain of 100 atoms. Enforcing only one degree of freedom with the variable N, objective is to identify the disorder concentration information in the underlying Hamiltonian. We encode the strength of impurity using onsite potential as $\epsilon_{imp} = 0.5$ for $t = 1$. It is important to note that configurational averages are defined over multiple configurations as a function of concentration N and ϵ. By treating N as a variable we can look for minimization trends in the $\Delta\Gamma$ for known value of ϵ_i. The transmission signature depicted in Fig. 3.4 acting as the input function for the inversion procedure which corresponds to an unknown concentration and unique arrangement of impurities.

The deviation between average transmission and input signature(Γ_{in}) is given as

$$\Delta\Gamma(E, N) = \Gamma_{in}(E) - \langle\Gamma(E, N)\rangle \tag{3.3.1}$$

Difference between input transmission signature and the CA spectra at a fixed energy does not indicate any system specific feature. Fig. 3.5 depicts the deviation absolute $\Delta\Gamma$ for different energy points. Wide error bars hides the system specific signatures, because the transmission fluctuations are universal. In case of 1-D system, first term on the R.H.S. is the effect of scattering in the sample. Second term is the average response of the system for given concentration, thus we observe somewhat flat mean absolute deviation in Fig. 3.5.

3.3.1 *Misfit Function*

Analysing the deviation between transmission spectra, *i.e.* input sample ($\Gamma_{in}(E)$) and CA($\langle\Gamma(E, N)\rangle$) at a fixed energy does not reveal any system specific information. However, much cleaner trends are seen when $\Delta\Gamma$ is used in the form of a functional

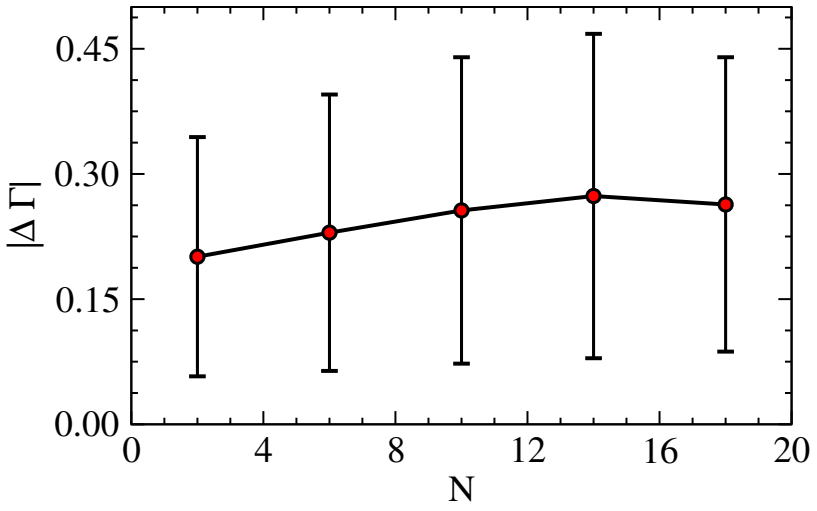

Figure 3.5: Absolute value of the transmission deviation as a function of disorder concentration N at $E = 0$ for a system of linear chain 100 atoms.

that measures how good a match $\Gamma(E)$ and $\langle\Gamma(E,N)\rangle$ are. We define the misfit function $\chi(N)$ as

$$\chi(N) = \int_{\mathcal{E}_-}^{\mathcal{E}_+} dE\ [\,\Gamma_{in}(E) - \langle\Gamma(E,N)\rangle\,]^2\ , \tag{3.3.2}$$

where $\mathcal{E}_-$ and $\mathcal{E}_+$ establish the energy window over which the integration takes place. Using the same input depicted in Fig 3.4 the misfit function can be plotted with concentration as the variable. Fig. 3.6(a) shows χ as a function of N and displays a more distinctive trend when integrated over energy. The plot indicates that there is a sweet spot in impurity concentration for which the integrated deviation is minimal. Remarkably, this agrees with the actual number of disorders used in the calculation of $\Gamma(E)$. Such a coincidence suggests that it might be possible to use $\chi(N)$ as an inversion tool to find the number of impurities in a quantum device from simple transmission measurements. When repeated for 1000 different configurations inversion method indicates great accuracy from the size of error bars. The energy integration limits are $\mathcal{E}_- = 0$ and $\mathcal{E}_+ = t$, impurity strength $\epsilon = 0.5 * t$. Note that energy integration plays a significant role in identifying the real impurity concentration from from $\Gamma(E)$. Misfit function takes the form of deviation for $\mathcal{E}_- = \mathcal{E}_+$ generating featureless trend. Integrating over energy probes

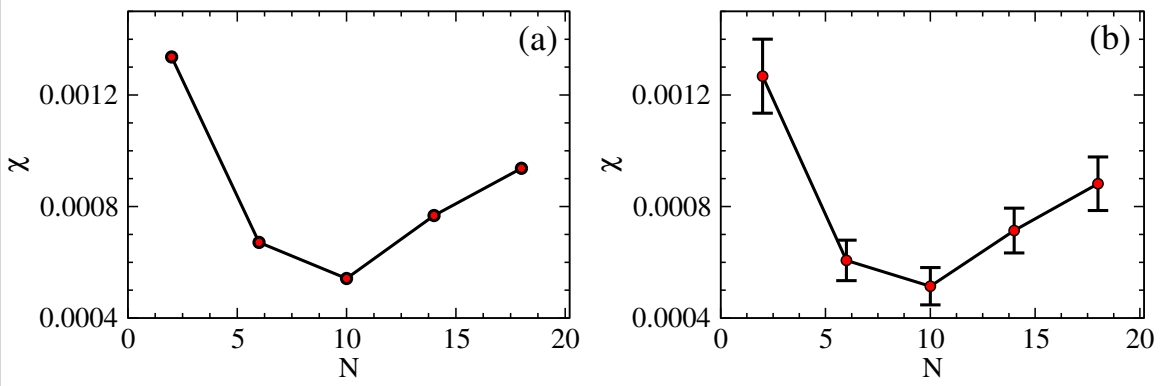

Figure 3.6: Panel (a) depicts the misfit function defined for input transmission plotted in Fig. 3.4 developing minimum at $N = 10$. Panel(b) shows the misfit function for 1000 input transmissions with 10 disorders present in each configuration. Misfit functions in both panels are generated with energy window defined by $\mathcal{E}_- = -1$ and $\mathcal{E}_+ = 1$ and disorders with $\epsilon_i = 0.5$.

closest configurational average signature by minimizing the deviation. This suggests that accuracy of the inversion largely depends on the integration limits.

The misfit function χ depends on the integration limits $\mathcal{E}_+$ and $\mathcal{E}_-$, that is, the averaging energy window. Fig. 3.7 plots the inversion error $\alpha = (N_{misfit} - N)/N$ as a function of $(\mathcal{E}_+ - \mathcal{E}_-)/Z$, where Z is the bandwidth. Note that α is large for very narrow energy windows, in perfect agreement with the single-energy featureless results of Fig. 3.5. When the energy window is broadened beyond 20% of the bandwidth, $\alpha \leqslant 0.2$ in the case of $n = 4\%$. In practical situations, it can be a difficult task to obtain the transmission spectrum over a significant portion of the bandwidth. We argue that small values of α can be already obtained with smaller averaging windows. The idea of averaging is to eliminate the universal transmission fluctuations from the misfit function χ. Hence, the averaging window has to be sufficiently broad to contain a large number of oscillations of $\Gamma(E)$. More precisely, $\Delta E/\delta E_{cor} \gg 1$, where δE_{cor} is the transmission autocorrelation length. Fortunately, the transmission fluctuations in mesoscopic systems are characterized by δE_{cor} that are typically much smaller than the band width Z. Theory shows that δE_{cor} depends essentially on the mean level density and on the average transmission $\langle \Gamma(E, n) \rangle$ [104, 105].

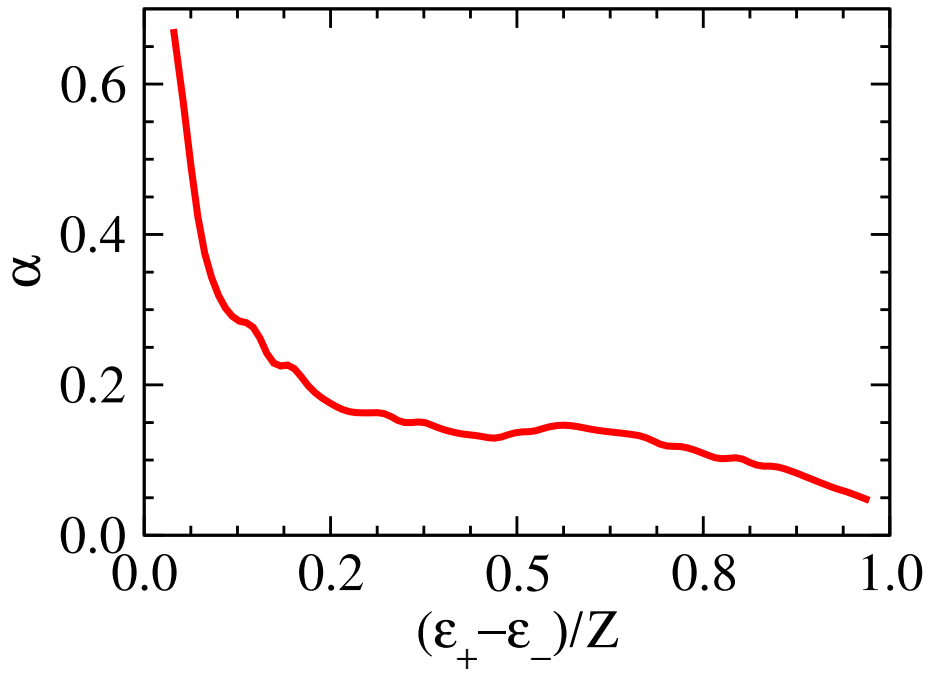

Figure 3.7: Inversion accuracy α as a function of averaging energy window considered for inversion technique. Averaging is carried out with 1000 different configurations of $L = 100$ unit cells, each one of them containing 4% of impurities.

The accuracy of misfit function mainly depends on the bandwidth of integration and number of configurations used to generate the CA spectra(M). In the previous sections we have established that the conductance fluctuations contains very little system specific information and the average transmission smoothly depends on energy. To obtain accurate averages from a data set of the conductance as a function of energy we use ergodic hypothesis. For conductance we can write that

$$< \Gamma(E) >= \frac{1}{\Delta E} \int dE \Gamma(E), \tag{3.3.3}$$

here $\Gamma(E)$ is an ensemble average and right hand side of the equation stands for running average. Note that the misfit function defined in Eq. 3.3.2 is similar to a running average and corresponds to the considering a large number of disorder realizations in the configurational average part of the calculation.

More specifically the ergodic hypothesis states that conductance fluctuations of a single sample versus energy are related to sample to sample fluctuations at fixed

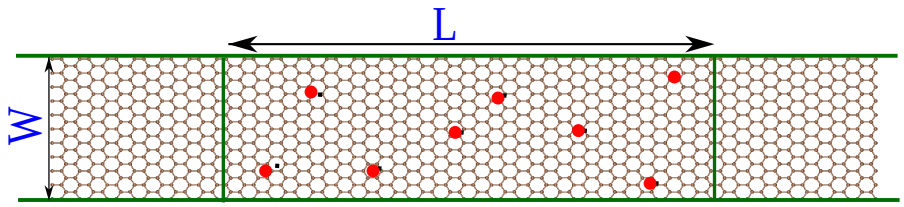

Figure 3.8: A schematic representation of two terminal graphene nanoribbon setup of width *W* and length L. Red dots in the device region represents presence of disorder in the system.

energy. Integrating over a continuos parameter (energy) is equivalent to sampling different configurations. The energy integration is analogous to considering a wider universe of disorder configurations in the CA procedure. As a result misfit function naturally induces the distinctive minimum for large enough bandwidth and statistically accurate CA. We do not present full mathematical analysis of ergodic hypothesis however it can be proven exactly for certain models of disordered systems [106, 107]. The continuous parameter used in the procedure is energy. However, there is no fundamental difference in the methodology for magnetic field or gate voltage as a continuous parameter. It is worth mentioning that detailed mathematical analysis of the ergodic hypothesis is not main focus of this work but in the next section we provide a simple mathematical method to calculate the concentration of disorders .

We now proceed to introduce realistic systems mainly in form of graphene nano ribbons, nanotubes and Hexagonal boron nitride ribbons.

3.3.2 *Graphene*

To demonstrate the inversion technique for graphene nano ribbons we keep the same setup used for 1D case. Schematic 3.8 shows the graphene nanoribbon device connected with graphene electrodes in a traditional two-terminal setups of width *W* and length of the device L. Concentration $n(\%)$ (N/N_{Tot}) of disorders are randomly

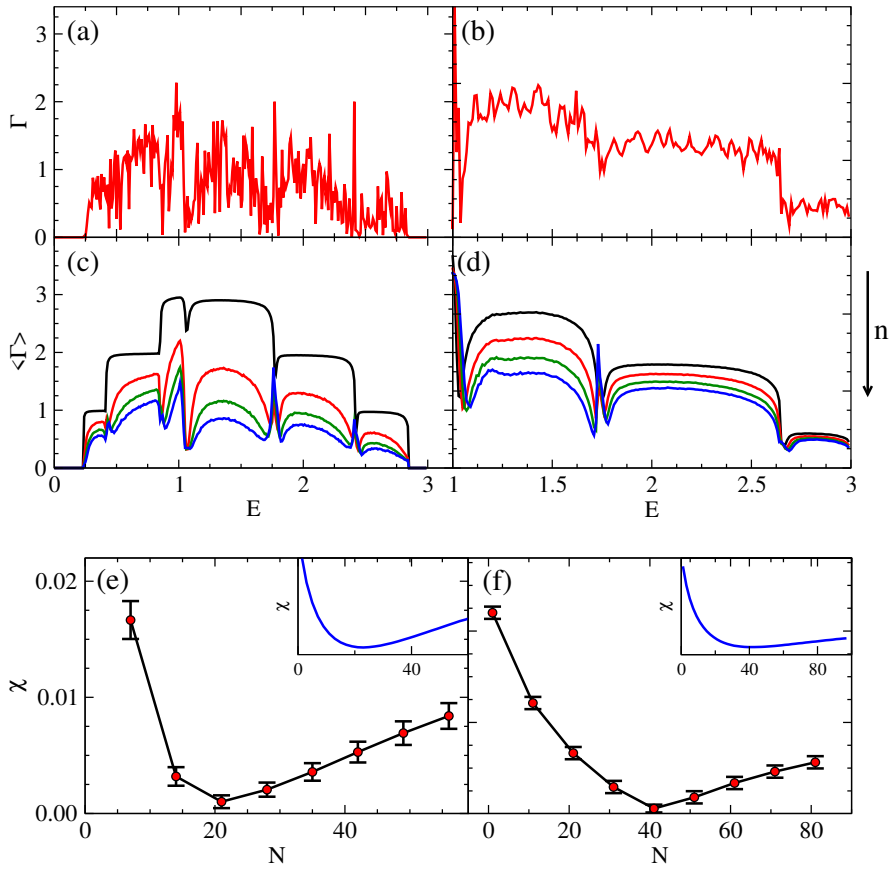

Figure 3.9: In panel (a) and (b), Calculated conductance of a system made of graphene nanoribbon and nanotube respectively of length L = 100 unit cells a function of chemical potential for t = 1 with 3% and 2% of disorders present in them modelled for $\epsilon_i = 0.5$. Panel (c) and (d) shows the configurationally average conductances for graphene nanoribbon and nanotube system, with increase in impurity concentration average conductance drops. Corresponding misfit function of the transmission signatures presented in panel (a) and (b) are depicted in the insets of (e) and (f). The error bars are generated over testing the inversion over 1000 configurations.

distributed in the system. In nearest neighbour tight-binding Hamiltonian we encode the disorders as substitutional type of impurity in case of nanotubes and ad-atom in nano-ribbons [108, 109]. Both type of disorders are of strength $\epsilon_{imp} = 0.5t$ with host material sites $\epsilon = 0$. Fig. 3.9(a) shows energy dependent transmission for a 7 atom wide armchair graphene nano-ribbon of width $W = 3a$, $a = 2.7\text{Å}$ being the lattice parameter adjacent panel(b) depicts the transmission for 10 atom wide radius of carbon nanotube with N disorders randomly distributed in the system. Fig. 3.9(c) and (d) shows configurationally averaged CA transmissions for ribbon and nanotube systems of length L = 100 unit cells respectively.

Transmission signals depicted in panels of Fig. 3.9(a) and (b) acts as the input to the misfit function defined in Eq. 3.3.2. Insets of Fig 3.9(e) and (f) shows the corresponding misfit function for armchair edged graphene nanoribbon and carbon nanotube system developing minimum at $N = 20(2\%)$ and $N = 42(3\%)$ respectively. Minima developed in panel (e) and (f) correctly coincides to the actual concentration of disorders present in the system. Note that no prior information about concentration of disorder was necessary to correctly invert the transmission signature. Error bars in panels (e) and (f) are generated by carrying out the inversion over 1000 different configurations with same number of disorders.

For both systems the integration limit is $\mathcal{E}_- = 0$ and $\mathcal{E}_+ = 1.5$ and the onsite potential of the disorders is $\epsilon_{imp} = 0.5$, however this bandwidth is not a strict criteria for the inversion. The number of configurations used to derive CA are $M = 1500$ for both type of systems plotted in Fig. 3.9(c) and (d). Another important aspect to note that the resolution of misfit function depends on the CA transmission. In the presented cases CA is a function of discrete values concentration from $n = 0\%(N = 0)$ to $n = 7\%(N = 150)$. At higher concentration the CA curves are closer to one another due to saturation of transmission in quantum devices. Later in the chapter we will investigate accuracy of the misfit function in terms of concentration, integration window and number of configuration considered for CA, *i.e.* M. This proves that the inversion procedure is indeed independent of material type.

The inversion methodology presented in the previous section extracts fundamental information about the underlying Hamiltonian. Misfit function describes the concentration of disorders present in the system. This characterization is carried out by minimizing deviation between transmission signature of the device with configurational average. In this section we provide mathematical structure to the misfit function. Following analysis is carried out for 7-AGNR host system. Fig. 3.10(a) shows CA transmission at different energies for low concentration regime we can write the CA transmission to linear order of n as [110]

$$\langle \Gamma(E, n) \rangle = \Gamma_0(E) - \beta(E)\, n \tag{3.3.4}$$

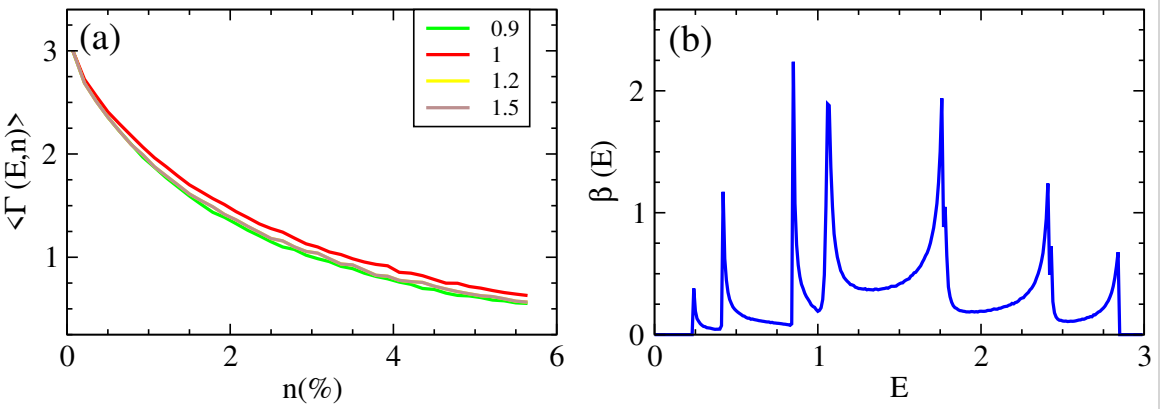

Figure 3.10: Panel (a) shows the CA transmission as a function of concentration(n%) at different energies. Panel (b) the $\beta(E)$ is plotted for the 7-AGNR system at $n = 0\%$, $\beta(E)$ has the maximum area under cure at $n = 0\%$.

Here, $\beta(E)$ is derivative of $\langle\Gamma(E)\rangle$ evaluated at $n = 0$, we can write

$$\beta(E) = \frac{\partial\langle\Gamma(E,n)\rangle}{\partial n}|_{n=0} \tag{3.3.5}$$

$\Gamma_0(E)$ is transmission signature for the pristine system. Substituting Eq. (3.3.4) in Eq. (3.3.2), we can write

$$\chi(n) = \int_{\mathcal{E}_-}^{\mathcal{E}_+} dE(\Gamma(E) - \Gamma_0(E) + \beta(E)n)^2 \tag{3.3.6}$$

Differentiating equation 3.3.6 with respect to n we can write,

$$\frac{\partial\chi}{\partial n} = n\int_{\mathcal{E}_-}^{\mathcal{E}_+} dE\,\beta^2(E,\epsilon) - \int_{\mathcal{E}_-}^{\mathcal{E}_+} dE\,\beta(E)(\Gamma_0(E) - \Gamma(E)) \tag{3.3.7}$$

The misfit function will naturally develop a minimum at $n^* = -B/A$, where

$$A = \int_{\mathcal{E}_-}^{\mathcal{E}_+} dE\,\beta^2(E,\epsilon) \tag{3.3.8}$$

and

$$B = \int_{\mathcal{E}_-}^{\mathcal{E}_+} dE\,\beta(E,\epsilon)\,(\Gamma(E) - \Gamma_0(E)) \tag{3.3.9}$$

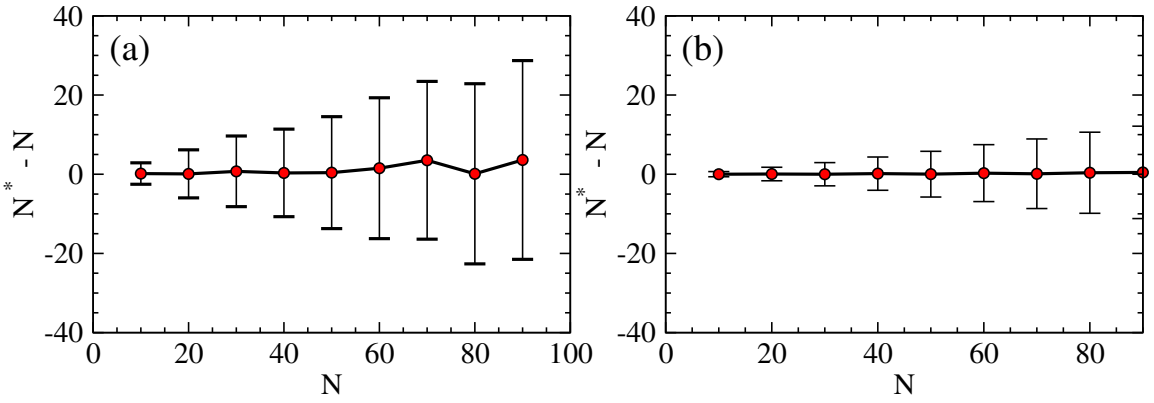

Figure 3.11: Panel (a) and (b) shows analytical solution of the misfit function calculated using non-recursive and recursive techniques respectively. 50 configurations of each disorder occupation are reflected in the error bars.

$$n^* = -\frac{\int_{\mathcal{E}_-}^{\mathcal{E}_+} dE\, \beta(E,\epsilon)\,(\Gamma(E) - \Gamma_0(E))}{\int_{\mathcal{E}_-}^{\mathcal{E}_+} dE\, \beta^2(E)} \tag{3.3.10}$$

The expression for n^* provides a simple way of identifying the minimum of misfit function to the point that Taylor expansion is valid.

The first order approximation of CA transmission generated a minimum in the misfit function located at $n^* = -B/A$. Both A and B result from integration whose integrands involve the function $\beta(E)$ defined in the main text as derivative of CA transmission evaluated at $n = 0$. While this is an excellent approximation for $n \leqslant 3\%$. It can be extended to higher concentrations (up to 7%) if we adopt the following recursive procedure. We must redefine $\beta(E)$ as the n-derivative of the CA transmission evaluated at an arbitrary concentration n and follow the steps below:

1. Evaluate $\beta(E)$ at $n = 4$.
2. Calculate n^* with the β function evaluated in step 1.
3. Substitute the value of $n*$ calculated in step 2 in the β function, *i.e.* $n = n^*$ and evaluate β function.
4. Calculate n^* with β evaluated in step 3.

5. Iterate the first 4 steps until n^* converges.

The expression for n provides a simple way of identifying the minimum of the misfit function.

3.4 MULTIVARIABLE MISFIT FUNCTION

In the previous section we defined the misfit function to extract disorder concentration. However, inversion methodology is flexible enough to accommodate more than one degree of freedom. Transmission spectra of a device is a result of multiple factors not just the concentration of disorders. In many cases different types of scattering centres are present in the system giving rise to unique scattering processes. We can generalise the misfit function to write,

$$\chi(n_1, ...n_i) = \int_{\mathcal{E}_-}^{\mathcal{E}_+} dE[\Gamma(E) - \langle \Gamma(E, n_1, ...n_i)\rangle] \tag{3.4.1}$$

Note that to calculate the misfit function we must compute the CA transmissions with i variables, *i.e.* different properties of the scattering centres. It is straightforward to state that increase in the number of variables increases the computational cost drastically as CA will generate n^i transmission datasets accounting to n points and i variables. In this section we focus on two cases for which the misfit extracts more than one variable.

Following the same algorithm presented in the previous section we begin with an arbitrary transmission signature, however without any knowledge about the concentration n and strength of disorders ϵ. For the same 7-AGNR host material consisting 100 unitcells with parameters $\epsilon = 0$ and $t = 1$. Fig. 3.12(a) shows the transmission signature of such device which acts as the input to the misfit function which takes form

$$\chi(n, \epsilon) = \int_{\mathcal{E}_-}^{\mathcal{E}_+} dE[\Gamma(E) - \langle \Gamma(E, n, \epsilon)\rangle]^2, \tag{3.4.2}$$

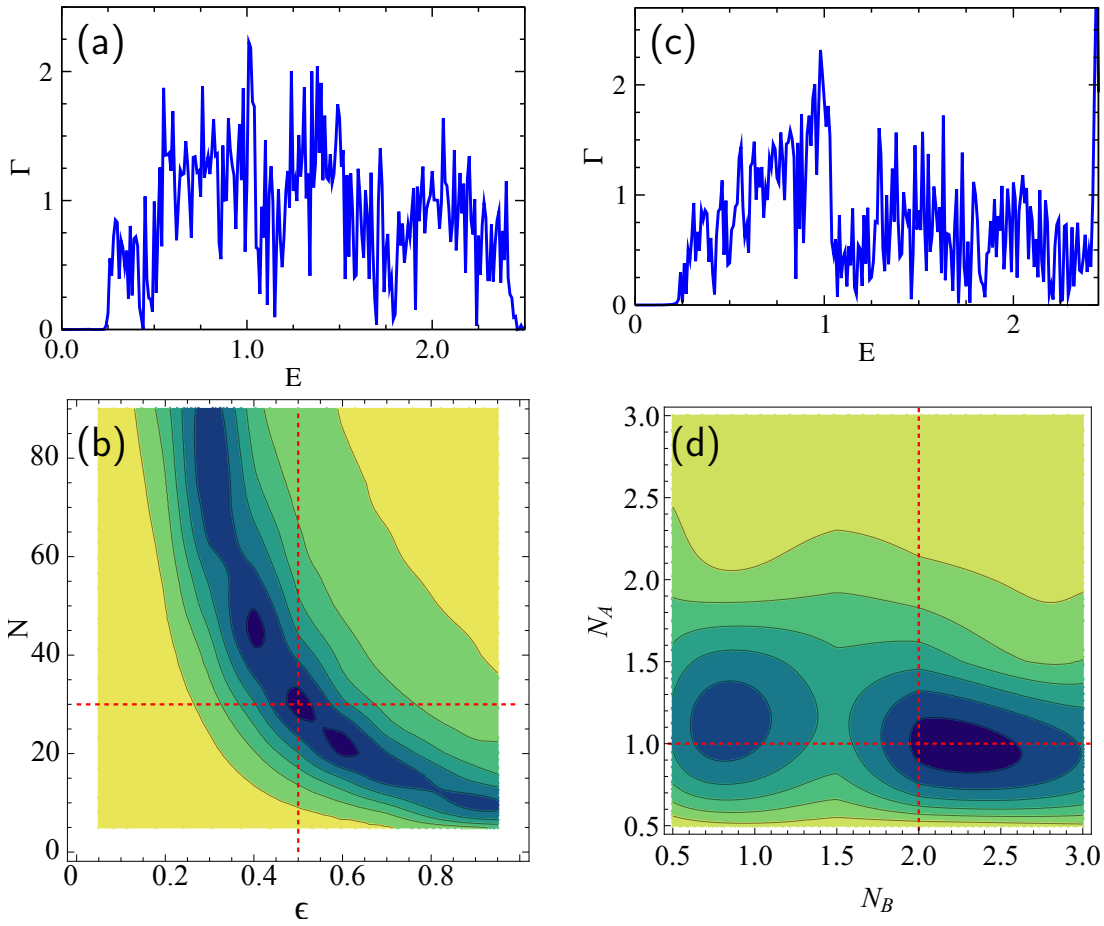

Figure 3.12: Panel (a) shows the transmission signature of a device with N = 30 disorders of onsite potential $\epsilon_i = 0.5$ used as an input to the misfit function plotted in panel (b). A 2-D contour plot of the misfit function developing minimum at N = 30 and $\epsilon = 0.5$. Dashed lines indicate the values of the respective quantities used in the underlying Hamiltonian. Similarly panel (c) corresponds to the input transmission function with 2 different types of disorders.(d) The 2-D misfit function correctly generating global minimum at the actual occupation of disorders present in the system at 1% for type A and 2% for type B.

Note that CA and misfit are function of both concentration and strength of the disorder. A 2D contour plot of misfit function χ is shown in the Fig. 3.12(b). A distinctive minimum is visible in the figure, coinciding with the actual number and strength of disorders present in the input transmission function. Consequently, misfit function can extract both the concentration and strength of the disorders from energy dependent transmission signal.

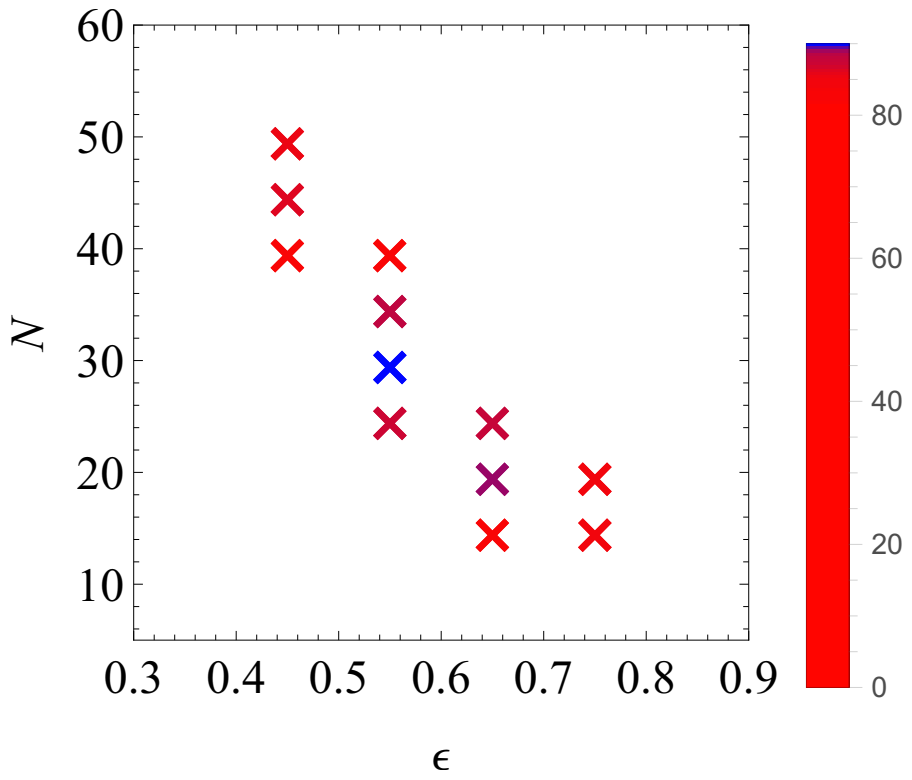

Figure 3.13: Accuracy of the inversion procedure when carried out for 200 configurations. Each configuration consists of 30 substitutional disorders with onsite potential of 0.5. Each cross corresponds to the minimum obtained from the inversion.

Note that in Fig. 3.12(b) misfit function points at 3 local minimums visible in dark blue regions. However, the global minimum corresponds to the actual values of concentration and strength of impurities. It is also interesting to see that the blue region follows the similar trend we see in the CA procedure in Fig. 3.3(a). CA signatures corresponding to the points in this region are closely packed to one another and as a result the misfit function is relatively flat. Thus extracting the occupation and strength of disorders requires larger bandwidth to obtain same level of accuracy for single variable inversion. To test accuracy of methodology, we carried out for 200 different configurations with randomly distributed disorder occupation of 3%(N = 30) with strength $\epsilon = 0.5$ for integration limit $\mathcal{E}_- = 0$ and $\mathcal{E}_- = 1.5$. Scatter plot in Fig. 3.13 shows accuracy of inversion coded with colour. Note that misfit function correctly points out both of the disorder properties in most of the cases.

CA calculation are carried out for the concentration of disorder varying in units of $N = 5$. We can always improve this resolution by calculating the CA transmissions in smaller steps. The interpolation scheme explained in Appendix 2 becomes a useful tool to generate the CA transmissions at a smaller disorder steps, *i.e.* increasing the resolution of of the inversion procedure.

In order to test the inversion methodology, keeping the same degrees of freedom we now adopt multi-impurity model.Keeping the same 7-AGNR as the host system with 2 different types of disorders randomly distributed in it with concentration N_a and N_b respectively. For simplicity disorder type A and B are modelled as substitutional impurities with on-site potential ϵ_A and ϵ_B. We can now define the misfit function in terms of N_A and N_B as

$$\chi(N_A, N_B) = \int_{\mathcal{E}_-}^{\mathcal{E}_+} dE[\Gamma(E) - \langle \Gamma(E, N_A, N_B)\rangle]^2, \tag{3.4.3}$$

Fig. 3.12(c) shows input transmission signature of such device with onsite potential of disorders $\epsilon_A = 0.3$ and $\epsilon_B = 0.8$ without any information about concentration. Again a 2D contour plot of misfit χ is plotted in Fig. 3.12(d) with dashed red lines representing for the actual concentration N_A and N_B. Minimum in the misfit function correctly coincides with actual disorder concentration. This allows us to define the misfit function in various ways to accommodate multiple degrees of freedom. With increase in number of variables misfit function requires better optimization techniques. Flexibility of this inversion methodology allows to write misfit function in a variety of ways. One simple approach is to first calculate the total concentration as occupation of type A and type B are constrained by $N = N_A + N_B$.

3.4.1 *Hexagonal Boron Nitride*

The ribbon is infinite in length but, in its doped form, impurities are spread over a section of $L = 100$ layers long. The tight-binding Hamiltonian for the hBN host uses three distinct on-site energy values to model B and N atoms on the host and C atoms as impurities of the system: $\lambda_B = -6.64$ eV, $\lambda_N = -11.47$ eV, and $\lambda_C = -8.97$

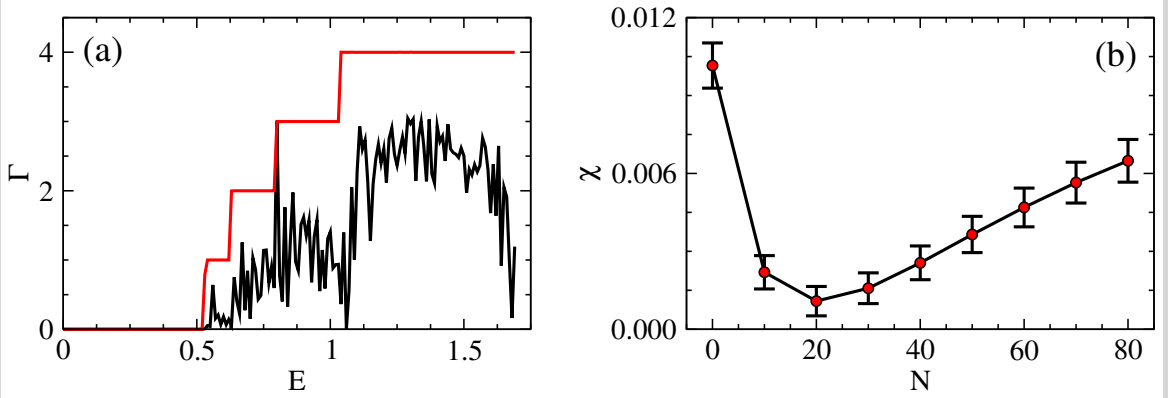

Figure 3.14: (a)A section of input transmission function of hexagonal boron nitride system is depicted in black with $N = 20$ carbon atoms randomly distributed in the system. Red curve represents pristine signature corresponding to parameters $\epsilon_c = 0.8$, $\epsilon_B = 0.664$, $\epsilon_N = 1.1$ and $t = 0.617$.(b) Misfit functions generated over 50 configurations with $N = 20$ carbon atoms in them.

eV [111]. Hopping terms were parameterized as $t = -6.17/a^2$ [111, 112] with a being the pair-wise bond length. For a boron-nitrogen bond, $a = 1.43$ Å and, for the sake of simplicity, we consider that boron-carbon and nitrogen-carbon bond lengths do not change significantly from that value. The noisy conductance curve in Fig. 3.14(a) corresponds to the parent system of a hBN ribbon doped with $n_i = 2\%$ of substitutional impurities and the red curve is the conductance of the pristine hBN nanoribbon. The misfit function shown in Fig. 3.14(b) acquires a minimum at $n_{min} = 2\%$, evidencing that the method predicted correctly the concentration of the parent system.

Another way to prove the generality of our methodology is to extend its use to a multi-dimensional phase space. Till this point, the inversion procedure looked at one degree of freedom which was the impurity concentration. However, it is possible to extend this analysis to a two-dimensional phase space, e.g., as we are going to illustrate. This analysis turns particularly interesting if applied to the hBN case because impurities can replace two types of atoms on the host (N or B). This means we can decompose the concentration information into the two distinct sublattices. Considering that a total of N impurities can be substitutionally dope a segment length of an hBN nanoribbon, we can write that $N = N_B + N_N$ where N_B (N_N) is the number of boron (nitrogen) atoms replaced by an impurity. Therefore,

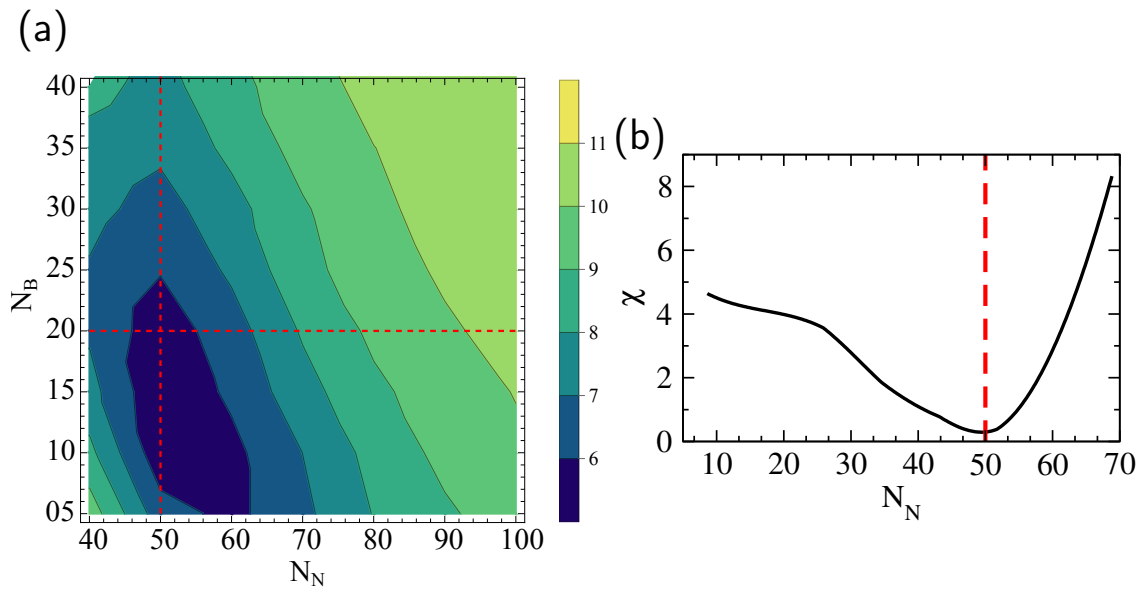

Figure 3.15: (Left panel) Misfit function (χ) surface plot taken for an armchair-edge hBN nanoribbon with 7 atoms along its width. The ribbon is infinite but carbon impurities were spread randomly over $L = 100$ unit cells along its length. The bar color express values of χ. The control parameters along x- and y-axis are N_N and N_B, respectively; those account for the number of carbon impurities replacing nitrogen (N_N) or boron (N_B) atoms. Dashed lines intersect at the characteristics of the parent system with $N_N = 50$ and $N_B = 20$. The minimum of χ correctly predicts the characteristics of the parent system as it lays within the region where $N_N = 50$ and $N_B = 20$. (Right panel) Curve of χ versus N_N taken from left panel by slicing the misfit surface plot horizontally at $N_B = 20$ (red horizontal dashed line). A distinctive minimum at $N_N = 50$ (red vertical dashed line) correctly finds the occupation of carbon impurities on nitrogen sites of the parent system. Bandwidth considered for inversion is 70% of the entire spectrum.

we can write the misfit function in terms of these two degrees of freedom to probe occupation of impurities on both boron and nitrogen sites as

$$\chi(N_B, N_N) = \int_{\mathcal{E}_-}^{\mathcal{E}_+} dE \, [\, T(E) - \langle T(E, N_B, N_N) \rangle \,]^2 \tag{3.4.4}$$

A certain number of C atoms are then spread over the hBN host in such a way that they can replace equal portions of B and N atoms or they can cause a sublattice unbalance. In other words, we can define a parameter δ as $\delta = N_N - N_B$ that can serve as a metric for this unbalance: if $\delta > 0$, C atoms majorly occupy the nitrogen sublattice, if $\delta < 0$, C atoms majorly occupy the boron sublattice, and

if $\delta = 0$, C atoms occupy both sublattices equally. A 2D contour plot of χ as defined in equation (3.4.4) is presented in Fig. 3.15 left panel. The global minimum correctly coincides with the occupation of impurities placed on boron ($N_B = 20$) and nitrogen ($N_N = 50$) sublattice of the parent system highlighted by the intersection of vertical and horizontal dashed red lines. The right panel in Fig. 3.15 corresponds to an horizontal slice taken from the surface plot at fixed $N_B = 20$ to visualize the dependency of χ with N_N and to highlight the minimum of χ at $N_N = 50$. The fundamental difference between boron and nitrogen sites allows to identify occupation of carbon impurities on corresponding sublattices. However, identifying the exact position of impurities still remains an elusive task. This example proves that extending the inversion methodology to inspect more than one degree of freedom does not affect its generality and robustness. Looking at more than one degree of freedom in the misfit function certainly increases computational cost and may generate multiple minima. Nonetheless, the method can serve as a first approach to determine the exact features of a parent system that can be described in a multi-dimensional phase space. In other words, results as the one depicted in Fig. 3.15(b) narrows down considerably the range of search for the optimum N_B and N_N values. A refinement in the range of values can be achieved by re-applying the inversion procedure within the reduced parameter range and with an increased number of CA samples, M, and/or by increasing the bandwidth established for the inversion procedure.

3.5 INVERSION USING DENSITY FUNCTIONAL THEORY

To show that this method is indeed model-independent we have also tested it in the case of a system whose electronic structure is fully described by Density Functional Theory (DFT). Misfit function depends on two main variables, bandwidth available for the inversion and the ensemble average $\langle \Gamma(E, n) \rangle$. There are basically

two options on how $\langle \Gamma(E, n) \rangle$ can be obtained. First option is to follow exactly the same steps explained above and calculate the transmission spectra of several different disorder configurations fully within DFT, something that may be laborious and time-consuming. Bearing in mind that the impurity concentration n must be kept as a variable parameter, the averaging procedure defined in Eq. (3.2.3) requires M different configurations for every single value of n, which indicates how computationally demanding this task might become if carried out entirely within DFT. The alternative option is to use the tight-binding (TB) model to carry out the CA calculation. Being computationally far less demanding than DFT, the TB model provides a fast averaging strategy without necessarily compromising in accuracy. In particular, DFT-based transmission calculations were performed for armchair graphene nanoribbons of sizes $L = 100$ unit cells and $W = 3a$ containing a specific spatial distribution of nitrogen atoms as substitutional impurities .

3.5.1 *DFT-based tight-binding Hamiltonian*

There are numerous ways of extracting effective tight-binding (TB) Hamiltonians from DFT calculations, all of which reproduce the corresponding band structures very accurately [113–115]. Combined with the help of quantum transport scripts [116], the TB parameters can be exported to highly efficient codes [117–119] that can handle quantum transport calculations of very large systems. Despite the wide availability of such DFT-based TB Hamiltonians, for simplicity, the illustrative examples in the study focus on single-band TB models. We stress, however, the following description is applicable to whichever TB-based model one chooses to adopt.

Instead of the usual band-structure fitting [120, 121], our adopted procedure consisted of comparing the transmission spectra calculated within DFT and tight-binding. For the sake of differentiation we refer to them as Γ_N^{DFT} and Γ_N^{TB}, where the subscript simply indicates the number of impurities contained in the device. From the impurity-free results, *i.e.* Γ_0^{DFT} and Γ_0^{TB}, it is straightforward to extract the

hopping parameter t that best captures the electronic structure of the pristine ribbon in question. To calculate the onsite potential of the impurity two initial calculations were done, namely for a pristine GNR, and for a nanoribbon of length $L = 7$ unit cells containing only a single nitrogen substitutional impurity. The impurity on-site parameter ϵ is easily found from Γ_1^{DFT}, which corresponds to the transmission in the presence of only a single impurity. It follows from a simple plot of the misfit function as a function of the impurity on-site potential, *i.e.*

$$\chi(\epsilon) = \int dE[\Gamma_1^{DFT} - \Gamma_1^{TB}(\epsilon)]^2 \tag{3.5.1}$$

In this case $\Gamma_1^{TB}(\epsilon)$ is the tight-binding transmission of a ribbon with a single impurity with on-site potential ϵ. The function $\chi(\epsilon)$ presents a very distinctive minimum, which we adopt as the value that best represents the scattering strength of the impurity. It is worth mentioning that it is not necessary to know the exact location of the impurity in the DFT calculation. In fact, this is automatically accounted for by evaluating the misfit function $\chi(\epsilon)$ for distinct impurity locations in the tight-binding part of the calculation. This is depicted in left panel of Fig. 3.16. The absolute minimum found for $\chi(\epsilon)$ corresponds to the impurity location used in the DFT-based transmission which also defines the value of the on-site potential to be adopted in the subsequent CA calculation.

Finally, it is also instructive to compare the transmission spectra Γ_1^{DFT} and Γ_1^{TB}, the latter being calculated with the on-site potential ϵ obtained as described above. Bearing in mind that the misfit function was obtained by an integration in the $0 - 0.2\,eV$ energy range, the agreement between the two results shown in right panel of Fig. 3.16(b) is yet another indication of the effectiveness of our inversion procedure since both curves were calculated separately and independently.

Here, we have selected the latter option and made use of the N-impurity DFT spectrum shown in Fig. 3.17(b) to identify suitable TB parameters that describe the nitrogen impurities inserted in a GNR of similar dimensions to the one shown in Fig. 3.17(a). The CA transmission $\langle \Gamma(E, n) \rangle$ is then generated within the TB

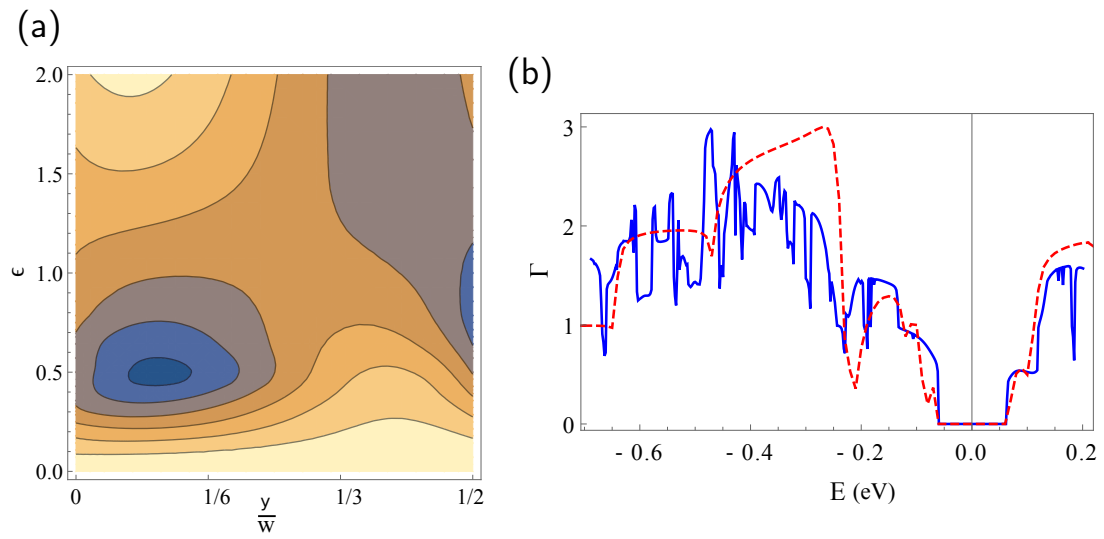

Figure 3.16: In panel (a), Contour plot of the misfit function χ to evaluate the impurity TB on-site energy ϵ. The single impurity sample transmission contains information about the location as well as the scattering strength of the impurity. The variable y/W indicates the impurity location, with $y/W = 0$ corresponding to the edge of the GNR and $y/W = 1/2$ marking its centre. In panel (b), Conductance as a function of the energy (in eV). The (blue) solid line represents Γ_1^{DFT} and the (red) dashed line corresponds to Γ_1^{TB}.

model employing $M = 2000$ realizations, leading subsequently to the misfit function $\chi(n)$ displayed in Fig. 3.17(c). Once again, $\chi(n)$ displays a distinctive minimum at exactly the same concentration of nitrogen impurities used to generated the input transmission $\Gamma(E)$ in the first place. Another indication that the inversion procedure works is to calculate the CA transmission evaluated precisely at the concentration that minimizes $\chi(n)$, shown as a dashed line in Fig. 3.17(b). Although it does not contain the short range fluctuations seen in the original signal $\Gamma(E)$, the CA transmission reproduces well all the key features of the input spectrum .

Now we will carry out the inversion procedure, *i.e.* CA part of the calculations and test transmission signature calculated entirely within DFT. From the Hamiltonians of the pristine ribbon and the one containing a single nitrogen, we assemble the N-impurity device by randomly distributing these building blocks over a fixed length and defect concentration. This is illustrated in Fig. 3.17(a) with the building blocks patched together to form the device containing a finite concentration of impurities. In this particular case, $N = 10$ impurities translates into a concentration

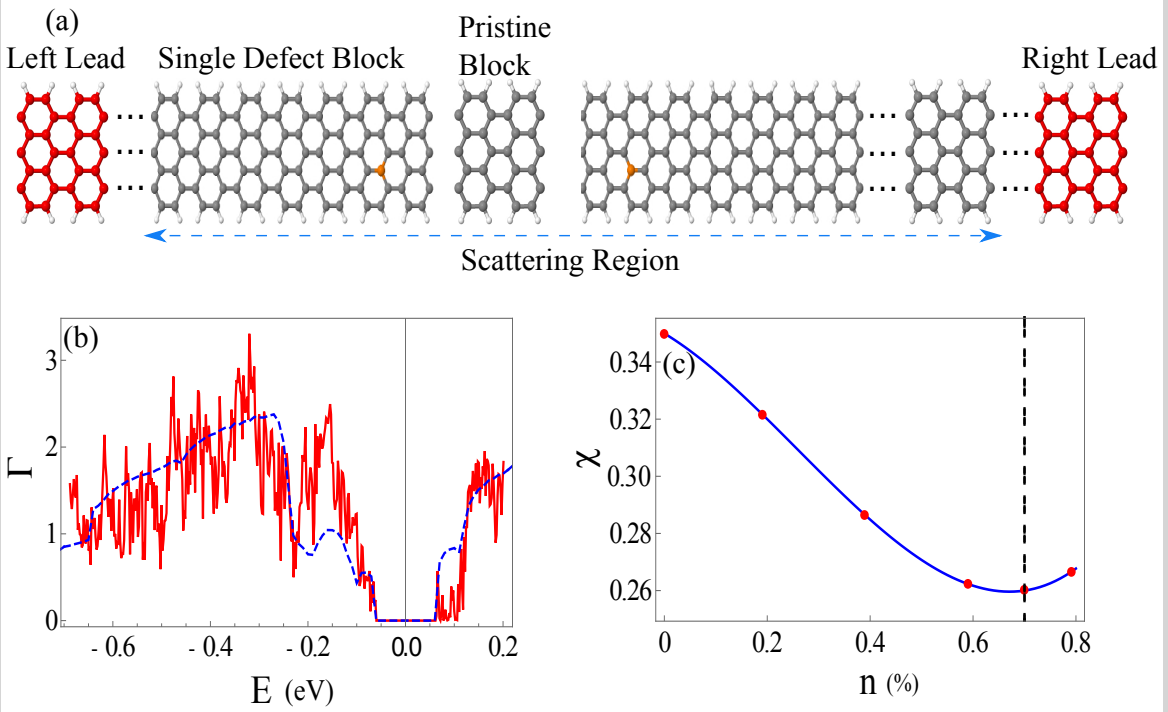

Figure 3.17: Inversion procedure of DFT-based results. (a) Illustrative diagram showing two different building blocks patched together at a random order to generate the finite-concentration device. The Hamiltonian of both blocks were obtained from DFT calculations (see text); (b) The (red) solid line depicts the transmission spectrum $\Gamma(E)$ obtained from a specific sequence of building blocks with $N = 10$ nitrogen substitutional impurities, *i.e.*, $\eta = 0.7\%$. The (blue) dashed line represents the CA transmission ($M = 2000$) calculated for the concentration that minimizes the misfit function χ, shown in (c) as a function of η (in percentage). The misfit function was generated with an energy window defined by $\mathcal{E}_- = 0$ and $\mathcal{E}_+ = 0.2\,eV$. Dashed line indicates the exact concentration used to generate the input transmission.

of $\eta = 0.7\%$. Given the localized nature of the basis orbitals, the full Hamiltonian for the disordered problem is block tri-diagonal. We can thus use a recursive method [122–125] to find the Green function matrix elements required to compute the Landauer transmission, Eq. (2.5.1). Following these steps we were able to obtain the transmission spectrum $\Gamma(E)$ of the system, shown in Fig. 3.17(b), which serves as the input transmission. For each concentration value, $M = 50$ different disordered configurations were considered, each one with 500 energy values. The obtained misfit function $\chi(\eta)$ seen in Fig. 3.18 displays the same distinctive trend seen previously and with a minimum at exactly the same value ($\eta = 0.7\%$) as the one depicted in Fig. 3.17(b). This clearly indicates that the inversion method can

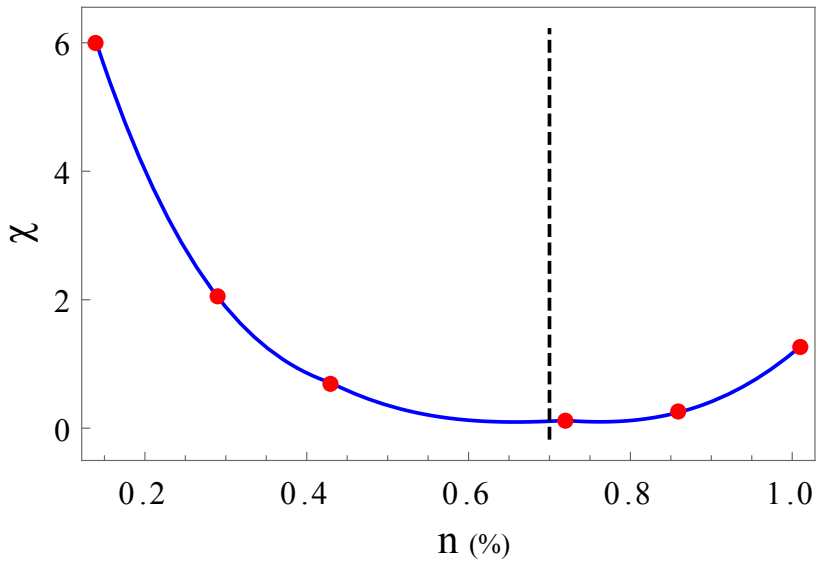

Figure 3.18: DFT based misfit function generated for an arbitrary configuration correctly indicates the minimum at 0.7% shown as a black dashed line.

decode the disorder signatures contained in the conductance signals regardless of the tool used to describe the underlying electronic structure. It is reassuring to find exactly the same answer using totally different tools.

3.6 ERROR ANALYSIS

Here we present a description of the inversion procedure implementation and an analysis of its accuracy. For that purpose we use the model system introduced in the Device section as an illustrating example. Our strategy relies on calculating the transmission spectra that is used as input functions of the inversion method simply because we can refer back to the Hamiltonian that generated them in the first place, allowing us to establish whether or not the inversion was successful. A simple test is to start from the Hamiltonian of an arbitrary specific configuration of N impurities randomly located and calculate the corresponding transmission spectrum. This translates into an impurity concentration n. The inversion works by

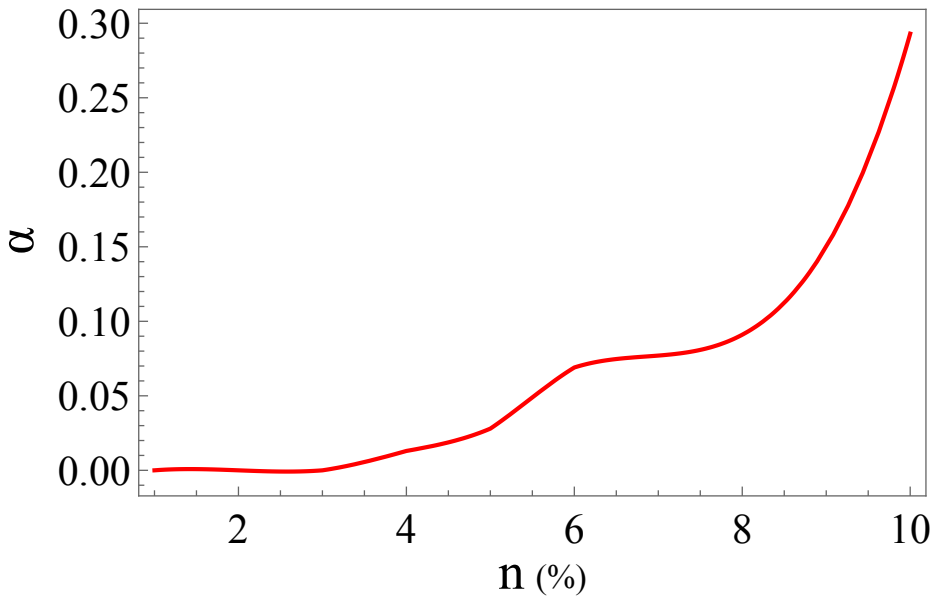

Figure 3.19: Inversion accuracy α plotted as a function of the impurity concentration n for a GNR with $W = 3a$ and $L = 100$ unit cells. The impurity on-site potential was arbitrarily chosen as $\epsilon = 0.5t$.

finding the concentration that minimizes the misfit function, which we call n_{min}. We then define the inversion procedure accuracy as.

$$\alpha = |n - n_{min}|/n \tag{3.6.1}$$

In the following section we analyse how α depends on a few essential parameters and show that a careful tuning of such parameters may improve the success rate of the inversion methodology .

3.6.1 *Concentration*

Fig. 3.19 shows that the inversion error is very small for all concentrations below 8%. It clearly indicates that it is a reliable inversion tool for dilute impurity concentrations. It is worth recalling that we can not only confirm what the real impurity concentration that generated the Hamiltonian is but also the exact locations of the randomly placed impurities. Interestingly, as the concentration increases we find a growing number of impurities that are adjacent to one another forming pairs that

may act as if they were isolated scatterers. For example, a randomly selected configuration of 15 impurities may have 13 of them well isolated whereas the remainder are clustered into a pair. In cases like that the inversion finds a concentration that would correspond to 14 impurities for the simple fact that the cluster may actually behave as a single scatterer. This explains why the inversion error also increases with the concentration. It is possible to reduce the error further by accounting for the probability of forming such pairs. In fact, we may adopt a similar strategy to the one used to produce Fig. 3.12, *i.e.*, we may treat impurity pairs as if they corresponded to a different class of impurities. In this way it is straightforward to discern between isolated and paired impurities, leading to a substantially improved error in the case of higher concentrations.

3.6.2 *M*

Regarding the number of configurations needed in the CA procedure, as standard, the higher the value of disorder realizations M the smaller the fluctuations in $\langle \Gamma(E, n) \rangle$. Universal transmission fluctuations (UCF) help one to obtain accurate results for $\langle \Gamma(E, n) \rangle$ at a modest value of M. Both for diffusive [97, 98] and chaotic ballistic systems [96], $\mathrm{var}(\Gamma) \approx 1$ is the main fingerprint of UCF. Hence, the CA relative statistical error is expected to scale with $[\sqrt{M} \times \langle \Gamma(E, n) \rangle]^{-1}$.

To bring the degree of fluctuations to an acceptable level and produce results that are statistically significant, we note that M is usually of the order 10^3. [99, 100]. One-dimensional (1D) systems, with corresponding smaller mean dimensionless transmission, require higher values of M to achieve statistical significance. Likewise, larger 2D systems and 3D ones, with larger mean transmission coefficients than those considered in this study, may require fewer configurations.

Fig. 3.20 confirms the earlier statement that $M = 10^3$ is sufficient to achieve statistical significance and reduce fluctuations to acceptable levels. In fact, the inversion error practically vanishes once M is of that order of magnitude.

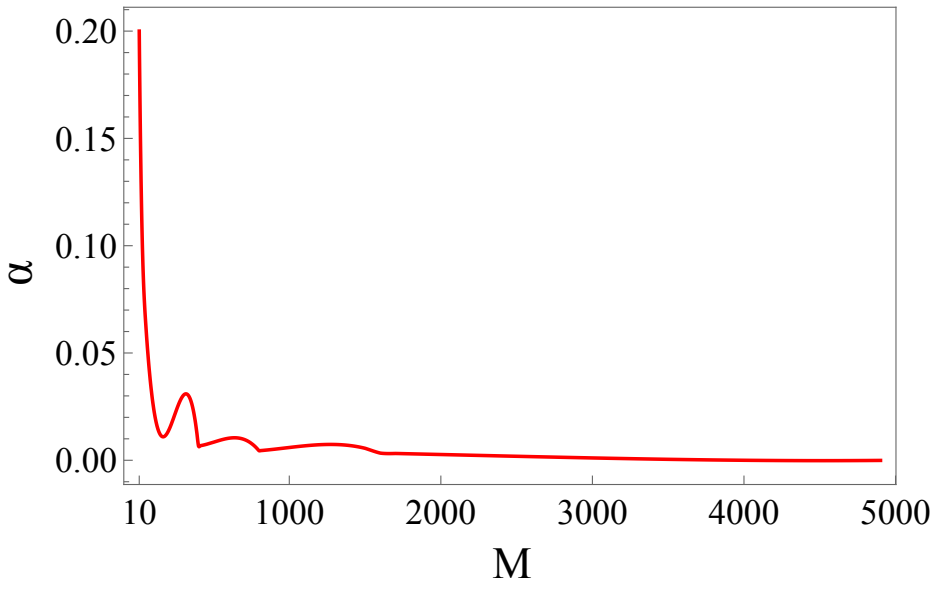

Figure 3.20: Inversion accuracy α as a function of M. Calculations are for a GNR of L = 100 unit cells, all of which containing 3% of impurities.

3.7 SUMMARY

All input spectra used in this study were directly calculated from a known Hamiltonian for the obvious reason that it would be straightforward to test whether or not the inversion method is successful . Ultimately, of course, inversions must be carried out in systems for which we do not have the capacity to check the Hamiltonian that originally produced the observations. This calls for an inversion tool that is reliable, general and robust. The fact that our inversion strategy works for systems whose electronic structures are described by simple single-band TB model, as seen in Fig. 3.9(e) and(f), as well as by the multi-band representations of DFT calculations shown in Fig. 3.17 is indicative of the generality and robustness of this methodology. Furthermore, it is worth stressing that the inversion tool can handle a variety of other systems that are in no way limited to 2D as shown in Fig. 3.6.

Regarding the question proposed in the introductory chapter 1 that disorder is beneficial rather than detrimental to this inversion procedure, note that this is particularly evident in the contrast between Fig. 3.5 and Fig. 3.6. The non-distinctiveness of the Fig. 3.5 curves suggests that when viewed at a fixed energy the deviation

between the input and CA transmission spectra is not strong enough to identify the exact concentration that generated the input spectrum in the first place. However, this changes in the case of misfit function because now the deviation is being integrated over a finite energy range, giving rise to significantly more distinctive features. It is worth noting that transmission fluctuations of a single sample versus energy can be regarded as a reflection of the large statistical fluctuations seen from sample to sample at a fixed energy. In other words, we use an ergodic hypothesis assuming that a running average over a continuous parameter upon which the transmission depends is equivalent to sampling different impurity configurations or doing an ensemble average. Here this continuous parameter is the energy but the concept can be extended to a range of other equivalent quantities such as an external magnetic field or an applied gate voltage, for example. The success of the inversion procedure will therefore depend on how wide the integration range is. In the cases considered here anything beyond 20% of the bandwidth leads to excellent success rates.

In summary, section 3.3 the inversion procedure presented here provides a transparent mechanism capable of identifying the composition of scattering centres in a quantum device by simply looking at the energy dependence of the two-terminal device transmission. Assuming that the impurity type within the device is known, the inversion tool provides an accurate way to establish the exact impurity concentration. Alternatively, in section 3.4 we prove that if no information is known *a priori* about the scatterers, the inversion can be used to identify their scattering strength and respective concentration. Finally, with a mixture of two different types of impurities we are also able to establish the fractional concentration of each component of the device. The inversion technique is extremely robust and versatile, being able to handle not only very simple electronic structure models but also more computationally-demanding and numerically-sophisticated calculations in 3.5. We argue that this versatility is indicative of a methodology that can be applied to a whole variety of systems and which can be used to extract structural and compositional information of quantum devices from standard conductivity

measurements. In the next chapter we take the next obvious step to extract spatial distribution of disorders in a quantum device using the misfit function inversion tool.

The work presented in this chapter was published as "Disorder information from conductance: A quantum inverse problem" (Physical Review B 102, 075409 (2020)) and "Decoding the conductance of disordered nanostructures: a quantum inverse problem" (J. Phys.: Condens. Matter 34 085901).

4

SUDOKU PROBLEM

4.1 INTRODUCTION

In the previous chapter we proposed an inversion technique procedure which accurately extracts structural information about perturbation present the in underlying hamiltonian of a quantum device. The misfit function minimizes at the correct values of parameters which in the first place are responsible for the input transmission function. Using the energy-dependent two-terminal conductance as the sole input, the misfit function identifies the exact number and properties of impurities within the disordered materials. Furthermore, it is particularly suitable to be used in carbon based, as well as in other 2D materials, it is very stable and works in the ballistic, diffusive as well as at the onset of the localised transport regimes. While the ability to determine the precise number of impurities in a device through conductance inversion is in itself a significant achievement, the misfit function is not able to capture the spatial distribution of impurities but only the average concentration between a pair of electrodes. Numerous machine learning strategies have been proposed to find the input configuration using the forward technique [30–38, 126]. In modelling the electronic transport using machine learning techniques, spatial and structural information about the impurities of numerous devices is required to define correct descriptor and model. ML models are defined around predicting conductance of the system correctly not the other way around. These models are definitely helpful in accelerating the search for the correct configuration corresponding to the input transmission. For instance, 7-AGNR system presented in chapter 3 with device size consisting of 100 unit cells counts to $N_{total} = 1400$ with $N_{imp} = 40$. The misfit function can extract concentration and strength of the scattering centres, *impurities*

present in the system. To obtain the spatial mapping of these 40 impurities the number of possible configurations necessary to compute are

$$\binom{1400}{40} = \frac{1400!}{40!100!} = 4.5 \times 10^{3592} \tag{4.1.1}$$

A viable inverse approach is thus necessary to obtain the spatial mapping of impurities in a nanodevice.

In this chapter, we demonstrate that the inversion technique presented in the previous chapter can be used to handle a multi-terminal disordered device to generate the spatial distribution of impurities in the nanodevice. This generalisation gives enormous flexibility to how a disordered structure can be interrogated and, in doing so, leads to an inversion tool that obtains spatial information about the impurity concentration. Remarkably, by resolving the impurity distributions into system partitions, that we call “cells", arranged in a grid-like geometry, the inversion procedure resembles a Sudoku puzzle in which the compositions of different sectors of a device are obtained by imposing that they must add up to specific values established for the grid rows and columns.

The experimental setup required to implement our proposal can be easily realised with current nanoscale fabrication techniques. Multi-terminal experiments have played a key role in the understanding of the electronic transport properties of graphene [127–130], as well as in a variety of 2D systems [131, 132] and surface states in topological insulators [129]. Through multiple measurements of local and non-local resistances [133], one can in principle experimentally determine the multiterminal conductance matrix. The possibilities have been vastly improved by techniques that enable to directly probe the local conductances at the nanoscale, some of them already applied to carbon based systems, such as scanning gate microscopy [134–137] and multi-probe scanning tunnelling spectroscopy [138, 139], to name but a few. These recent experimental developments provide extra motivation to explore what type of information can be obtained from a disordered device through selectively interrogating its transport properties, which is precisely the underlying idea behind this work.

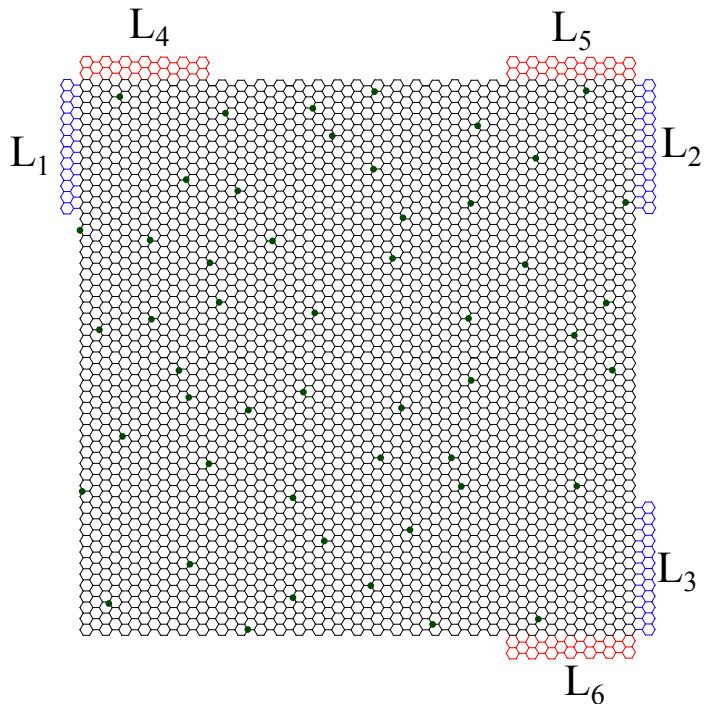

Figure 4.1: Schematic representation of a graphene sheet contacted to multiple electrodes. Electrodes are depicted as short coloured extensions of the honeycomb structure, labelled L_1 to L_6. The device possesses a number of randomly distributed impurities represented by solid dots.

This chapter is structured as follows, we begin presenting the inversion methodology in a multi-electrode framework and applying it first to an illustrative case in which the impurity concentration is captured as a whole but not spatially resolved. For the same device throughout this chapter, we demonstrate how the same inversion tool can be implemented to extract information about the spatial distribution of impurities from the conductance between terminals, sampling the electronic transport flow at different parts of the device. This will be done for a few different cases where the device is divided into a number of cells that determines the spatial resolution of the inversion.

4.2 MULTITERMINAL SET-UP

Fig. 4.1 shows a schematic diagram of the multi-terminal setup considered. It consists of a graphene system connected to multiple electrodes represented by the coloured stripes labelled L_1 to L_6 located on the edges of the device. Due to its relevance and model simplicity [108], we choose a graphene sheet as a case in point. We stress that the inversion methodology is also applicable to a variety of carbon-based materials and 2D systems as shown in the previous chapter. A graphene flake of dimensions $D_x = 30\sqrt{3}a$ and $D_y = 50a$, a being the lattice parameter of graphene is chosen as our case-study. Horizontal (Vertical) edges are chosen to be along the armchair (zigzag) direction. For simplicity, 6 electrodes connected to the device are placed at the corners of the flake. We stress that since the terminals are placed on both kinds of edge terminations, this arbitrary choice of boundary conditions has no impact on any of our findings. The graphene sheet contains a finite number of randomly distributed impurities represented by dots, here assumed to correspond substitutional atoms other than those of the host 2D material. Adsorbed impurities or vacancies can be easily considered as well[140, 141].

The transmission $T_{j,\ell}(E)$ is given by

$$T_{j,l}(E) = \mathrm{tr}\left[\Gamma_\ell(E)\mathbf{G}^r(E)\Gamma_j(E)\mathbf{G}^a(E)\right] \tag{4.2.1}$$

where $\mathbf{G}^r = (\mathbf{G}^a)^\dagger$ is the retarded Green's function of the full system, while Γ_l is the line or decay width matrix of the lead corresponding to the l-terminal. Both $\mathbf{G}^r$ and Γ_l are conveniently expressed in a discrete representation, typically a set of Wannier-like basis states. While $\mathbf{G}^r$ has the dimension of the number of Wannier-like states in the central region, the dimension of Γ_ℓ is the number of states at the l-lead-central region interface. The leads are considered as semi-infinite and the decay widths are computed by the standard prescription.

Multi-probe experiments measure the resistance $R_{j,l}$ and non-local voltages $V^{NL}_{j,l}$ between different pairs of electrodes [127]. Using gauge invariance and conservation

of current, Büttiker has shown that R and V^{NL} can be cast in terms of the conductance matrix [133]. In this case we can write

$$\begin{pmatrix} V_1 \\ V_2 \\ V_3 \\ V_4 \\ V_5 \\ V_6 \end{pmatrix} = \begin{pmatrix} R_{11} & R_{12} & R_{13} & R_{14} & R_{15} & R_{16} \\ R_{21} & R_{22} & R_{23} & R_{24} & R_{25} & R_{26} \\ R_{31} & R_{32} & R_{33} & R_{34} & R_{35} & R_{36} \\ R_{41} & R_{42} & R_{43} & R_{44} & R_{45} & R_{46} \\ R_{51} & R_{52} & R_{53} & R_{54} & R_{55} & R_{56} \\ R_{61} & R_{62} & R_{63} & R_{64} & R_{65} & R_{66} \end{pmatrix} \begin{pmatrix} I_1 \\ I_2 \\ I_3 \\ I_4 \\ I_5 \\ I_6 \end{pmatrix} \tag{4.2.2}$$

Hence, by taking different combinations of biased electrodes and voltage probes, one can reconstruct $\mathcal{G}_{j,l} = R^{-1}$, from experimentally obtained $R_{j,l}$ and $V^{NL}_{j,l}$ data. It is important to mention that the conductance $\mathcal{G}_{j,\ell}$ depends on the system-electrode contact resistances, but the multi-probe set up allows one to determine them and extract the system electronic properties [133].

The multi-terminal conductance expression, Eq. (2.5.6), is written in terms of Green functions and as such it is model independent. In other words, once the Hamiltonian is known one can find the corresponding Green function and subsequently obtain the energy dependent conductance of the system. For the sake of simplicity, we describe the electronic structure of the material within the tight-binding model. Once again, this is in no way a requirement of the inversion method, which has been proven to work also with other electronic structure models regardless of the number of atomic orbitals involved. We stress that the method does not rely on any specific property of the electronic structure calculation implementation.

4.3 MULTI TERMINAL MISFIT FUNCTION

The inversion procedure introduced in the previous chapter 2 allows one to obtain total number of impurities, N from transport measurements by combining Configuration-Average (ca) with the ergodic principle that associates average (en-

ergy) conductance of a single sample with sample-to-sample average at a fixed energy. More specifically, the ergodic hypothesis assumes that a running average over a continuous parameter upon which the conductance depends is equivalent to the ensemble average over different impurity configurations. In mathematical terms, the misfit function defined as

$$\chi_{j,j'}(N) = \frac{1}{\mathcal{E}_+ - \mathcal{E}_-} \int_{\mathcal{E}_-}^{\mathcal{E}_+} dE \left[T_{j,j'}(E) - \langle T_{j,j'}(E,N) \rangle \right]^2, \tag{4.3.1}$$

where the integration limits $\mathcal{E}_+$ and $\mathcal{E}_-$ are arbitrarily chosen energy values within the conduction band, provided $\mathcal{E}_+ - \mathcal{E}_-$ is much larger than the transmission autocorrelation width. The ca transmission $\langle T_{j,j'} \rangle$ is defined as

$$\langle T_{j,j'}(E,N) \rangle = \frac{1}{M} \sum_{m=1}^{M} T_{j,j'}^{(m)}(E), \tag{4.3.2}$$

where the superscript (m) labels the different realisations of disorder configurations. While both $T_{j,j'}$ and $\langle T_{j,j'} \rangle$ are functions of energy, the latter is also a function of impurity concentration N. When plotted as a function of N (or n), the misfit function is expected to display a minimum at a value that corresponds to the actual impurity concentration.

Fig.4.2(a) shows the calculated values of $T_{1,2}$ and $T_{4,6}$ of a system containing a total of $N = 50$ substitutional impurities, *i.e.* a concentration of $n \approx 1.5\%$, both plotted as a function of energy in red and blue colour respectively. In yellow the ca transmission spectrum is plotted as a function of energy for $N = 50$. Note that the actual number of impurities and how they are spatially distributed in the parent Hamiltonian are needed to generate $T_{1,2}$ and $T_{4,6}$, this information is not to be used in any part of the subsequent calculations but serves only as a reference to be compared against the final inverted results. Therefore, the conductance is the only input function for the inversion procedure.

Fig. 4.2(b) also displays the misfit functions $\chi_{1,2}$ and $\chi_{4,6}$ plotted as a function of the impurity number N. Both curves are obviously different but, reassuringly, possess distinctive minima at the same concentration value of $N = 50$, which coincides

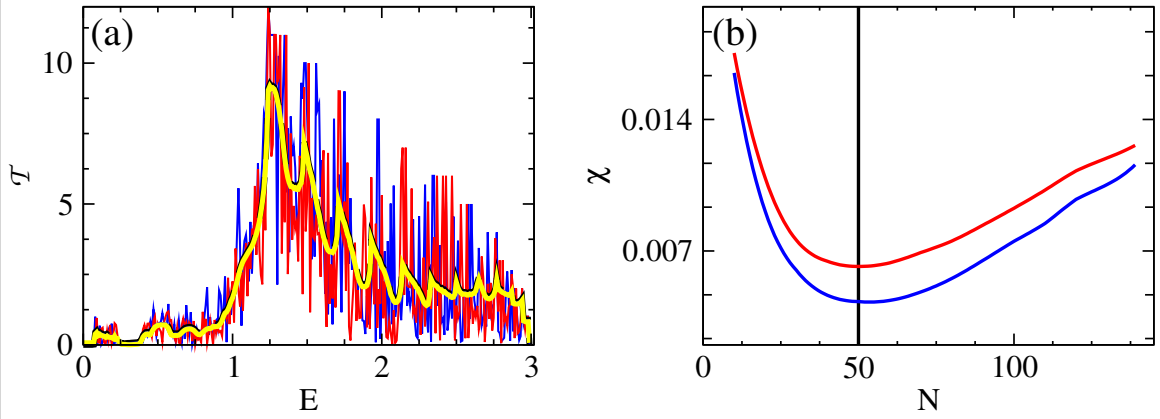

Figure 4.2: (a) Transmissions $T_{1,2}$ (blue) and $T_{4,6}$ (red) for a graphene sheet containing a total of 50 impurities, which translates into an overall concentration of $n = 1.5\%$, both plotted as a function of energy (in units of the electronic hopping integral t). Thick line in yellow represents the ca transmissions $\langle T_{1,2} \rangle$ for the same impurity concentration. $\langle T_{4,6} \rangle$ is not shown to avoid too congested a figure but it is very similar to $\langle T_{1,2} \rangle$. Panel (b) plots the concentration-dependent misfit functions $\chi_{1,2}(N)$ and $\chi_{4,6}(N)$, vertical black line is used as a reference to indicate the actual number of impurities present in the system.

exactly with the chosen impurity concentration that generated the transmission matrix elements T_{ij}. Furthermore, when plotting the ca transmissions $\langle T_{1,2} \rangle$ and $\langle T_{4,6} \rangle$ evaluated for the same impurity concentration we find very good agreement with the input functions $T_{1,2}$ and $T_{4,6}$ despite the fluctuations, as seen in Fig. 4.2(a). This is unmistakable evidence that the inversion method introduced in the previous chapter 3 can indeed account for the case of multiple electrodes. Another important aspect to note that the size of the electrodes does not affect the inversion procedure.

4.4 SPATIAL MAPPING

Since it was possible to obtain the total number of impurities in the device with only a single reading (either $T_{1,2}$ or $T_{4,6}$), we assume that the use of additional input functions might enable us to spatially resolve how these impurities are distributed. The multiterminal approach provides a way to interrogate the system to obtain

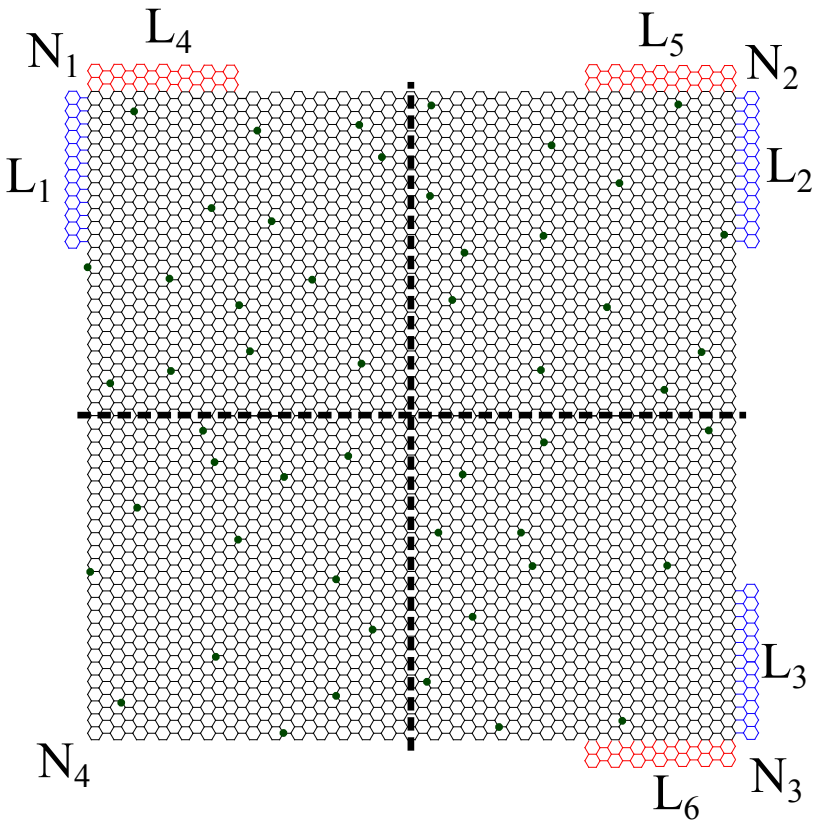

Figure 4.3: An extension of the Fig. 4.1. Dashed black lines resolves the device into 4 imaginary parts. The occupation of each block is assigned as N_1 to N_4.

multiple readings. We try to optimise the mapping procedure using minimum input readings.

4.4.1 *4 Cells*

With that in mind, we devise four partitions and assign the impurity numbers in each one of them as N_1 to N_4 as shown in the Fig. 4.3. t is important to stress that these are not physically built cells but simply a way in which we resolve the impurity number into smaller sections of the device. Vertical and horizontal dashed lines are drawn as a guide to the eyes in Fig. 4.1(a) delineating the four distinct cells. We follow the similar steps taken in regard to the ca conductances in order to obtain the misfit functions defined in Eq.(4.3.1) but this time the impurity numbers within the device may be broken into two separate parts: $N_T = N_1 + N_2$ and $N_B = N_3 + N_4$,

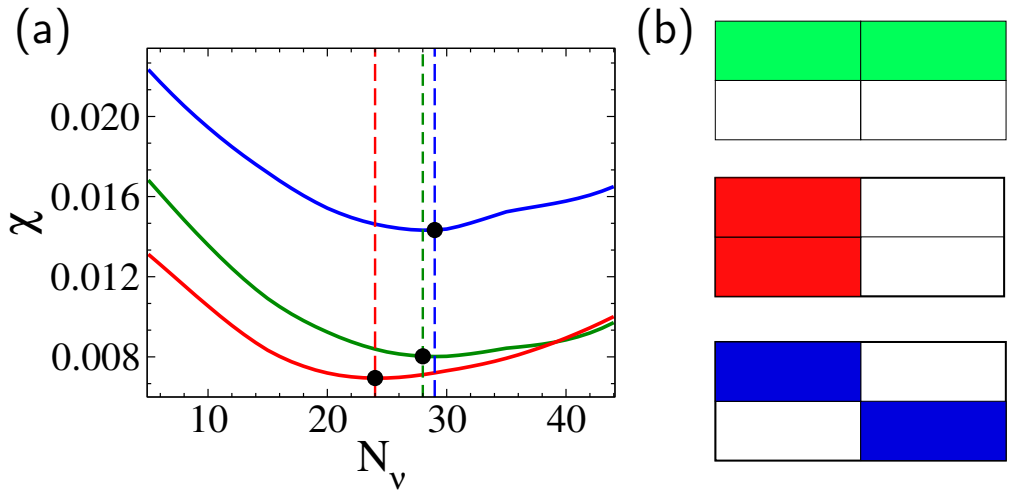

Figure 4.4: (a)Misfit functions $\chi_{1,2}$ (green), $\chi_{5,6}$ (red), and $\chi_{1,3}$ (blue) plotted as a function of a generic variable N_ν representing the number of impurities at different parts of the device. $N_\nu = N_T$ for the green curve, $N_\nu = N_L$ for the red curve and $N_\nu = N_{D'}$ for the blue curve. Vertical dashed lines indicate the distinctive minima seen in the misfit functions at $N_T = 28$, $N_L = 24$ and $N_{D'} = 29$ for the green, red and blue curves, respectively. Panel (b) shows area of the graphene flake associated with misfit function presented in (a) of same colour.

i.e., the top- and bottom-half values, respectively. N_T and N_B are constrained by the total concentration of impurities present in the system $N_T + N_B = N_{Tot}$. Note that we define the ca as a function of two variables, number of impurities placed in the top half and the total number of impurities placed in the system. This adds one extra degree of freedom to ca procedure and the misfit function which should now read $\chi_{1,2}(N_T, N_{Tot})$. Placement of the electrodes has little to none effect on the inversion procedure. This is useful as it allows us to resolve the device in symmetric regions, reducing the number of ca spectrums required. The misfit function $\chi_{1,2}(N_T, N_B)$ would in principle involve searching for minima of a two-variable function, but thanks to the previously obtained information about the total number of impurities in the device, we know that both variables are not independent but constrained to obey $N_T + N_B = N$. This is thus equivalent to a single-variable search.

In addition, the same can be done with horizontally placed electrodes. In this case $T_{5,6}$ corresponds to the conductance between the top and bottom electrodes on the right of the device. Once again, two new variables are defined, namely,

$N_L = N_1 + N_3$ and $N_R = N_2 + N_4$, which are the impurity numbers on the left and right halves of the device, respectively. The misfit function $\chi_{4,6}(N_L, N_R)$ is another two-variable function that in practice depends only on one of them because they are also constrained to satisfy $N_L + N_R = N$. Fig. 4.4 depicts the misfit functions $\chi_{1,2}$ and $\chi_{5,6}$ plotted as a function of N_T and N_L, respectively. Both curves display different minima located at values $N_T = 28$ and $N_L = 24$, respectively. Impurity numbers seen in Fig. 4.3 may differ slightly from the occupation obtained from a single misfit-function minimum. Combined with the previously obtained result of $N = 50$, in this case we may conclude that $N_B = 22$ and $N_R = 26$. Since N_T, N_B, N_L and N_R are not linearly independent quantities, knowing them is not sufficient to uniquely identify the impurity numbers in each one of the four cells. For that an additional inversion involving the conductance between diagonally opposite electrodes is required, which is achieved with $\mathcal{T}_{1,3}$. A similar procedure leads to the corresponding misfit function $\chi_{1,3}(N_D, N_{D'})$, where the variables $N_D = N_1 + N_4$ and $N_{D'} = N_2 + N_3$ refer to the impurity numbers along the two diagonals. Obviously, they must also obey that $N_D + N_{D'} = N$. Fig. 4.4 also shows $\chi_{1,3}$ plotted as a function of $N_{D'}$, with a clear minimum at $N_{D'} = 29$ ($N_D = 21$). The set of equations that cast these constraints is easily solved when expressed in matrix form, *i.e.*,

$$\begin{pmatrix} N_1 \\ N_2 \\ N_3 \\ N_4 \end{pmatrix} = \begin{pmatrix} 1 & 1 & 1 & 1 \\ 1 & 1 & 0 & 0 \\ 1 & 0 & 1 & 0 \\ 1 & 0 & 0 & 1 \end{pmatrix}^{-1} \begin{pmatrix} N \\ N_T \\ N_L \\ N_D \end{pmatrix} = \begin{pmatrix} 12.5(13) \\ 16.5(13) \\ 12.5(13) \\ 9.5(11) \end{pmatrix}, \tag{4.4.1}$$

which leads to the impurity numbers on each of the four cells. In this case, $N_1 = 12.5$, $N_2 = 16.5$, $N_3 = 12.5$ and $N_4 = 9.5$. The numbers in the bracket corresponds to the actual number of impurities present in the system. This is analogous to solving a Sudoku puzzle that starts from the conductance readings and finds the exact impurity numbers within each cell. The constraining information is that they must add up to the specific values N_T, N_L, N_B and N_D which are themselves determined through our inversion procedure.

Three input functions ($T_{1,2}$, $T_{5,6}$ and $T_{1,3}$) were needed to find the impurity number in each of the four cells, two extra readings when compared to the inversion for finding the total number. This not only proves our earlier assumption that additional readings would enable us to spatially resolve the concentration but also suggests that an even better resolution is possible by interrogating the system further. It is important to stress that additional readings must be used in a hierarchical fashion, *i.e.*, they provide new information about the device always availing of results obtained by pre-existing readings, also offering constraints for a next higher resolution inversion procedure. In this way we are able to increase the resolution without the need for excessive new input functions but keeping them to a minimum. Additional information, *i.e* readings can be used to define another set of misfit functions. This information can be used for the conditioning of the system of linear equations.

4.4.2 *9 Cells*

Following this path, we are able to go beyond the four-cell resolution. In this case a larger number of smaller cells is required, as seen in Fig. 4.5 where the same device is resolved in 9 cells. Dashed lines in Fig. 4.5 are used to delineate nine and sixteen cells, respectively, each containing a certain fraction of the total number of impurities. Our goal is to find the exact impurity number (concentration) in each one of these cells and the procedure is analogous to the case of four cells.

The difference lies primarily in how the cells are combined to carry out the inversion. While the results of Fig. 4.4 were obtained by combining cells into rows and columns, there are very many ways of selecting how the individual cells can be clustered. This gives an enormous degree of flexibility on finding the actual number of impurities in each cell.

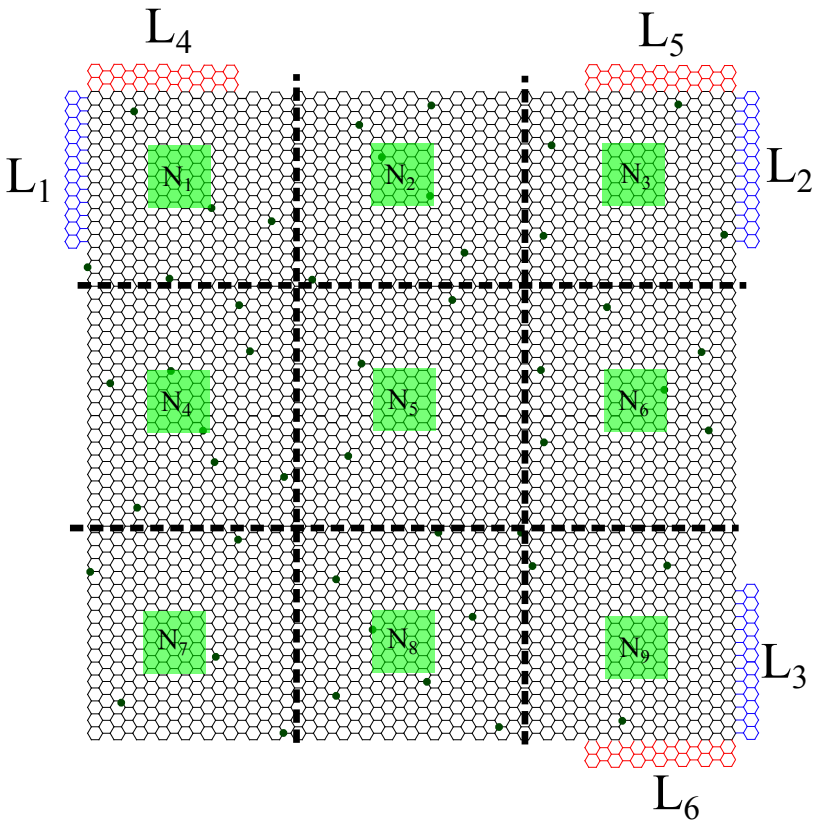

Figure 4.5: A schematic representation of graphene flake embedded with substitutional disorder with a six electrode setup labelled as L_i, with i running from 1 to 6. Dashed lines separate the flake into 9 cells and N_j represents the number of impurities contained in each of these cells.

To resolve the flake in 9 or 16 cells we need to define a system of linear equations which can be written in the form

$$AX - B = \lambda \,, \tag{4.4.2}$$

where A is a square matrix and the other elements are all single-column vectors whose size matches the number of cells. For example, in the case of 9 cells the equation takes the form of Eq.(4.4.2) with $\lambda = 0$. Matrix A contains information about regions chosen to define 9 misfit functions such that $detA \neq 0$. Variables N_i, with i running from 1 to 9, indicate the impurity occupation of the individual cells shown in Fig. 4.5(a) and M_i is the occupation of corresponding region obtained from the inversion. Note that we have flexibility on how we choose to interrogate the different parts of the flake, which means that the form of matrix A is not unique

but depends on that exact choice defined in the ca procedure. Eq. 4.4.3 shows one such choice of a system of linear equations for the given arrangement of electrodes.

$$\begin{pmatrix} 1 & 1 & 1 & 0 & 0 & 0 & 0 & 0 & 0 \\ 0 & 0 & 0 & 1 & 1 & 1 & 0 & 0 & 0 \\ 1 & 1 & 1 & 1 & 1 & 1 & 1 & 1 & 1 \\ 1 & 0 & 0 & 1 & 0 & 0 & 1 & 0 & 0 \\ 0 & 1 & 0 & 0 & 1 & 0 & 0 & 1 & 0 \\ 1 & 1 & 0 & 1 & 1 & 0 & 0 & 0 & 1 \\ 1 & 0 & 0 & 1 & 0 & 0 & 0 & 1 & 1 \\ 1 & 0 & 0 & 0 & 1 & 1 & 0 & 1 & 1 \\ 1 & 1 & 0 & 0 & 0 & 1 & 0 & 0 & 1 \end{pmatrix} \cdot \begin{pmatrix} N_1 \\ N_2 \\ N_3 \\ N_4 \\ N_5 \\ N_6 \\ N_7 \\ N_8 \\ N_9 \end{pmatrix} = \begin{pmatrix} M_1 \\ M_2 \\ M_3 \\ M_4 \\ M_5 \\ M_6 \\ M_7 \\ M_8 \\ M_9 \end{pmatrix} = \begin{pmatrix} 7(6) \\ 8(7) \\ 5(6) \\ 8(7) \\ 5(4) \\ 7(6) \\ 4(5) \\ 5(6) \\ 3(3) \end{pmatrix} \tag{4.4.3}$$

For example, the top-row identity from the matrix equation above reads that $N_1 + N_2 + N_3 = M_1$. By minimising a misfit function defined in terms of the variable M_1, we obtain the exact number of impurities in the top row of the flake, as shown in Fig. 4.5(a). The same must be done with other regions such that we find the values of all M_i in Eq.(4.4.3). Analogously to the four-cell case, the inversion is carried out with a few different readings. In this case, M_1, M_2 and M_3 are found from $T_{1,2}$; M_4, M_5 and M_6 are found from $T_{5,6}$; M_7 and M_8 are found from $T_{1,3}$; finally M_9 is obtained from $T_{4,6}$. The remaining task is to solve the sudoku-style puzzle of identifying the impurity numbers N_i of individual cells constrained to match the values of M_i. Solving Eq.(4.4.3) is an easy task for obtained values of M_i. The sudoku accurately predicts occupation of the impurities in relevant cells with a variance of 1 or 2 impurities. We must account for the possibility of error in the inversion procedure which would lead to the incorrect mapping of the disorder concentration. This can be alleviated by obtaining more information about the flake and availing of more misfit functions, which will then serve as extra constraints in Eq.(4.4.2). Constrained optimization methods like Lagrange multiplier or differential

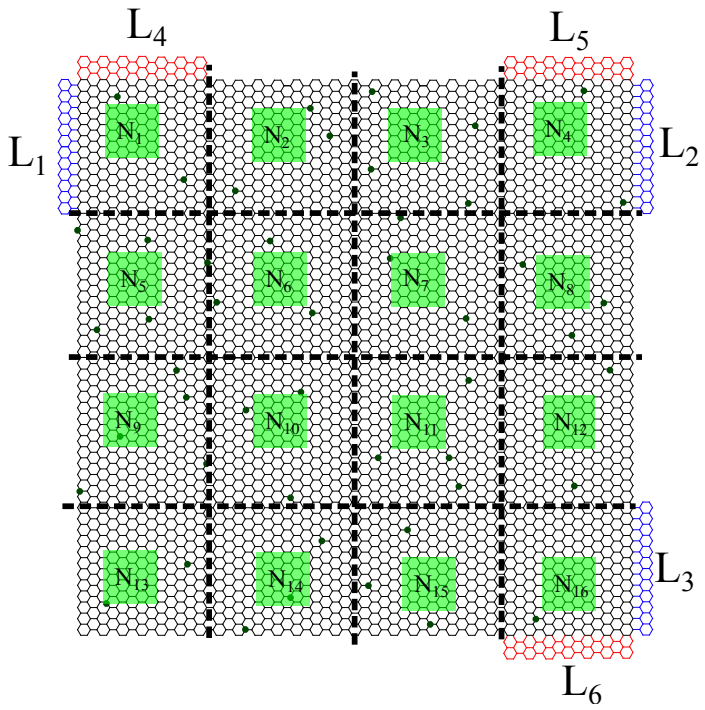

Figure 4.6: A schematic representation of graphene flake embedded with substitutional disorder with a six electrode setup labelled as L_i, with i running from 1 to 6. Dashed lines separate the flake into 16 regions and N_j represents the number of impurities contained in each of these cells.

evolution are very well established procedures and are suitable to be used here to find the values of N_j.

4.4.3 *16 Cells*

In the case of sixteen cells, the dashed lines of Fig. 4.6 delineate them together with the corresponding occupation numbers N_i, with i running from 1 to 16. Analogously to the previous cases considered and in line with Eq.(4.4.2), we must select regions based on which the misfit function will be calculated. Fig. 4.7 shows the regions selected for the inversion procedure. In panel (a) electrodes which are switched on are top left and right one., *i.e.* L_1 and L_2, for panel (b) L_1 and L_3. In the case of four quarters, $T_{1,2}$ served as input to the misfit function in order to extract information about top half of the flake. The same method can be implemented to obtain occupation of each of the four rows.

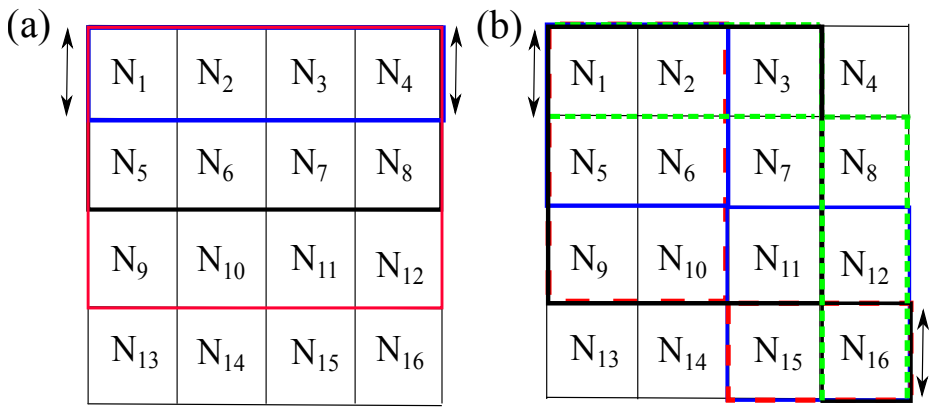

Figure 4.7: Flake is resolved into 16 cells with N_i running from 1 to 16 gives occupation of each cell of the flake.(a) Misfit function and corresponding ca is defined for the regions enclosed in blue, black and red lines for input signal generated from leads position presented in the form of double arrow lines. (b) For the leads positioned diagonally opposite of the flake dashed red green lines shows non-trivial consideration of region for the inversion.

We define such misfit function as $\chi_{1,2}(N_a, N_b, N_c, N_d)$ where N_a is the occupation of disorders in the first row, N_b second row and so on as shown in Fig. 4.7(a) with blue, black and red lines contouring respective area of the flake. Note that occupation in rows is constrained by $N_a + N_b + N_c + N_d = N$. Similarly, misfit function defined using the input in form of $T_{5,6}$ yields total occupation (N_e, N_f, N_g, and N_h) in each column of the flake in Fig. 4.5(b). The remaining equations needed to complete the system of linear equations come from the diagonal misfit functions. Diagonal misfit functions are defined using input transmission spectra from leads which are diagonally opposite to each other, namely $L_{1,3}$ and $L_{4,6}$.

We need to define a system of sixteen linear equations to obtain the occupation of each one of the cells. We have seven equations coming from $L_{1,3}$ and $L_{4,6}$. Two extra input signals from diagonally arranged leads will provide the remaining equations, namely $T_{1,3}$ and $T_{4,6}$. In Fig. 4.8, three misfit functions are plotted as a function of number of impurities. Misfit function in red is defined with variables enclosed by dashed red line shown in Fig. 4.7(b). Misfit function in blue is defined for region enclosed by black lines in the schematic representation seen in Fig. 4.7(b). It is worth mentioning that the misfit function is minimum at $N = 35$ and when compared with the actual distribution of impurities in the parent configuration the discrepancy

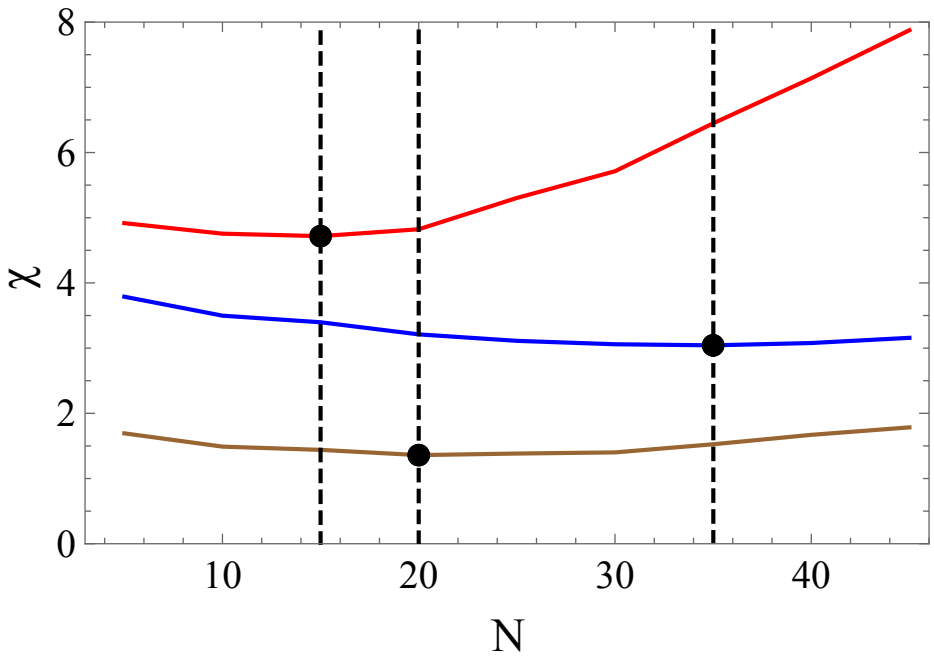

Figure 4.8: Misfit function in blue defined for region enclosed in the thick black line in Fig. 4.7(b) shows minimum at N = 35 which closely coincides with N = 37 actual number of disorders in region. Brown and red misfit curves locate the occupation of regions enclosed by dashed red line and dashed green line of Fig. 4.7, respectively.

does not exceed two impurities. Finally, the misfit function defined using the input signal $T_{4,6}$ completes the set of equations necessary to generate the system of linear equations. It is important to note that this is by no means the only way to resolve the device in sixteen cells. Different arrangement of leads may lead to different ways of mapping the impurities. Following our definition and choice for how the system was probed, the matrix A of Eq.(4.4.2).

0 (2)	2 (3)	5 (4)	3 (4)
7 (5)	4 (3)	1 (2)	3 (3)
5 (5)	2 (3)	6 (4)	2 (2)
3 (2)	2 (3)	3 (3)	2 (2)

Table 1: The table shows the real occupation of impurities for all sixteen cells together with the sudoku-style solutions. Numbers in brackets and blue colour are the actual occupation of impurities present in the system.

After solving this system of linear equations we can finally map the impurity distribution across the flake and this is shown on the right part of Table 1.

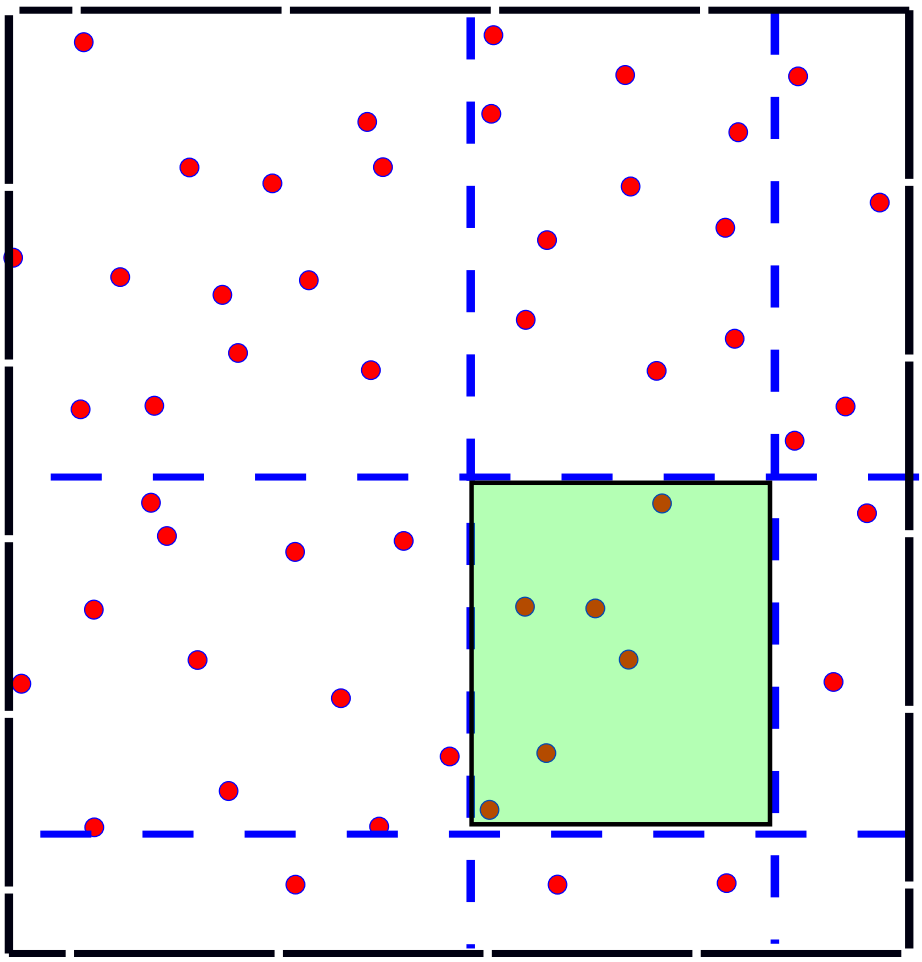

Figure 4.9: Green region represents a cell of arbitrary size and location within the device. Pink dots resembles the impurities present in the system. Blue dashed lines are used to resolve the device in initially in 4 parts.

4.5 GENERALISED PARTITIONS

In the previous sections, we presented a simple methodology to map the disorder of the system in the Sudoku-style structure of the flake. We resolved the flake into 4, 9 and 16 cells. Suppose that we are interested in establishing the impurity concentration within a certain sector of the device that does not coincide with any of the cells defined previously. In that case, instead of carrying out a full sudoku-style mapping which would involve defining a whole range of other cells, we may avail of the information obtained for the 4, 9 and/or 16 cells as a constraint in the search for the occupation in the cell of interest. That cells does not match with any other

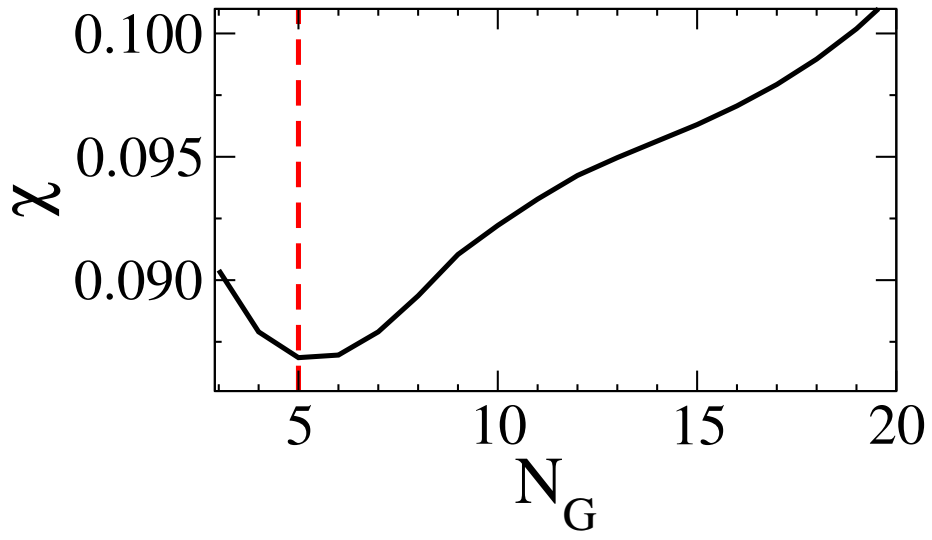

Figure 4.10: Misfit function defined for an arbitrary green region with N_G as the impurity number for that region. Minimum at $N_G = 5$ identifies the number of impurities for the green cell of Fig.3(c). The previously obtained input spectrum $\mathcal{T}_{1,3}$ was used to define the misfit function.

previously used cells but it is possible to find the impurity number N_G within that green cell by carrying out an additional ca calculation. This extra calculation is not particularly intense and simply involves a new misfit function that depends on N_G as its key variable but uses the information already obtained as constraints. Assuming that the green cell lies within one of the four sectors defined in the 2×2 case, whose solution is known from a previous inversion to be N_4, the misfit function that captures the problem at hand is $\chi(N_G, N, N_4)$. Using N and N_4 as constraints, we show in Fig. 4.10 this misfit function that displays a clear minimum at $N_G = 5$, which closely matches the actual number seen in Fig. 4.9. It is important to note that no additional input spectrum is needed to resolve the impurity concentration within an arbitrary region of the flake besides the readings already carried out.

4.5.1 *Role of the system-electrode geometry*

In the previous parts of chapter we showed how flexible this inversion technique is to the extent that we may obtain the spatial distribution of impurities on a 2D flake in a few different ways. With this in mind, we now illustrate yet another way in

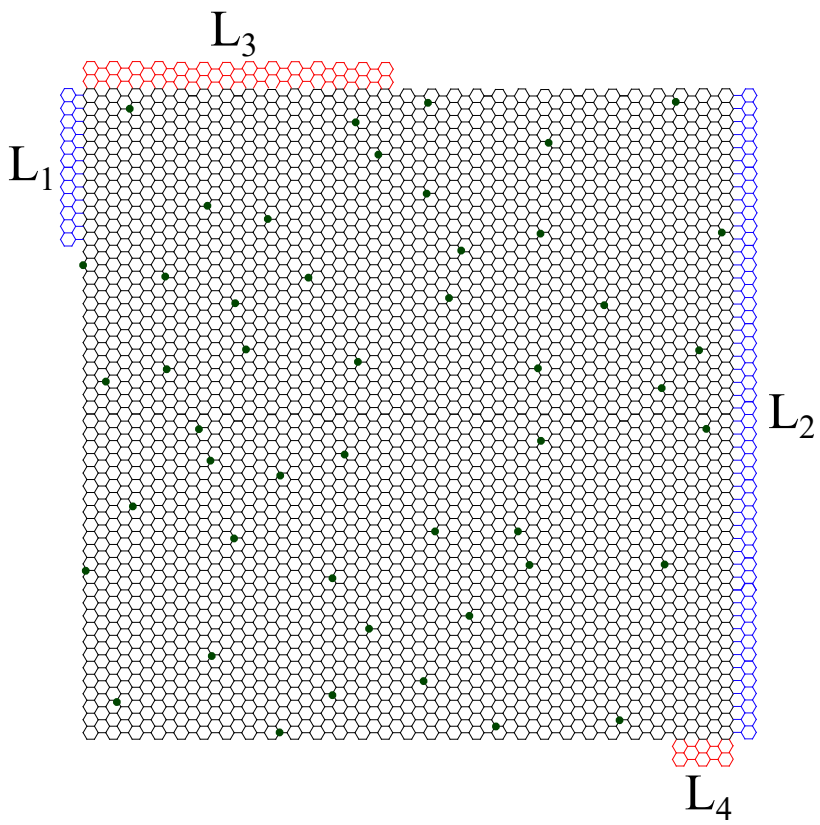

Figure 4.11: A schematic presentation of the hybrid approach where one lead spans entire width of the and other electrodes are of different lengths.

which the impurity distribution can be spatially mapped, this time using electrodes of different lengths. We considered a 6 electrode setup as shown in Fig. 4.11. We considered the case in which both injecting and extracting electrodes were of similar in size. All electrodes were of the quarter length of the side connected. We now relax this constraint and assume that electrodes have different dimensions, which we refer to as the hybrid approach.

A schematic representation of this can be seen in Fig. 4.11 where one lead spans the entire width of the flake whereas the other is either half, a quarter of the length of its counterpart or even shorter than the quarter length, as size of the electrode is not a critical factor in the IP.

It is important to stress that the exact setups, either the one shown in Fig. 4.1 or the one in Fig.4.11 here, are not unique regarding the positions and respective sizes of the electrodes being used. The two terminal set-up presented in the previous chapter fails to extract spatial information as the electrodes span the entire width of

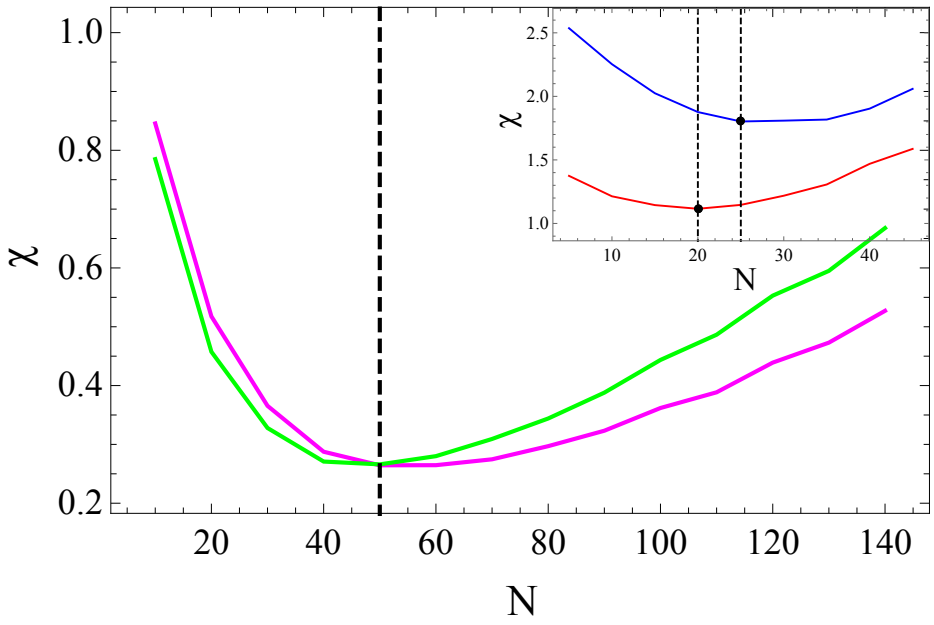

Figure 4.12: Misfit function plotted in blue colour is defined using input signal $T_{3,4}$ scans left half of the device. Misfit function defined using $T_{1,2}$ yields occupation of row constrained by pink leads and dashed blue lines .

the device. Such symmetric arrangement fails to quantify effect of spatial mapping of impurities in the system. The point here is to have them in a non-symmetric disposition. It is important to have such non-symmetric arrangement of leads.

In other words, the inversion success is not sensitive to the precise electrodes setup probing the conductance matrix. This makes the experimental realisation far less challenging than if it depended on the exact and precise placements of the electrodes. Here we follow similar steps to the ones taken previously and find exactly the same results as the ones found in Fig.4.1. In fact, Fig. 4.12 displays the misfit functions plotted as a function of impurity numbers in the entire flake using leads in magenta and green colors. Although the functions are different, both display a distinctive minimum at the same value of $N = 50$. In the inset another two misfit functions are plotted with minima indicating the occupation of the top row (red) and left half (blue) of the flake indicated with the dashed lines of Fig. 4.11.

4.6 ERROR ANALYSIS

The computational cost of calculating the misfit function depends on 3 main parameters. It contains (1) an energy integral as well as an (2) average involving M configurations of disorder, not to mention (3) the need to repeat the same procedure for a range of concentration values. Firstly, although expressed as an integral, the misfit function can be calculated as a discrete sum containing a reasonably small number of terms, usually 50 or more, without compromising in accuracy. Regarding the ca procedure, we find that by taking $M \approx 10^3$ configurations leads to results for the inverted concentrations with errors well below 5%, a remarkable achievement for a quantum inversion procedure as shown in the previous chapter. Finally, regarding the need to evaluate the misfit function for several concentration values, we adopt a smart interpolating scheme presented in the Appendix I that provides excellent resolution in $\chi_{1,2}(n)$ generated with only five distinct concentration values.

Another important aspect of the procedures is the number of input functions, *i.e.* readings. In case of 4×4 the sudoku requires 3 readings. As we increase the resolution of the sudoku system, required input data also increases. We implement the 3×3 problem with 4 input readings and 4×4 with 5 to obtain necessary accuracy. In all the cases presented in the chapter note that the agreement is very good and that discrepancies rarely exceed by a large amount. It is worth mentioning that natural uncertainties arise when impurities lie very close to the dashed lines separating the cells, since their scattering range may extend over more than one cell. This is particularly problematic as the cells are made smaller and the ratio between the cell perimeter and its area increases. Having mapped the concentration across the entire device in 3×3 or 4×4 cells, it is also possible to use this information to find the impurity number in a cell of arbitrary shape. The size and location of that specific cell highlighted in green does not correspond to any of the cells seen in panels (a) and (b) and yet, the number of impurities occupying that specific cell can be found by carrying out a single ca calculation using the same input functions already utilised previously. As this involves obtaining the minimum of a single-

variable misfit function which, as previously mentioned, is not computationally intensive.

To this point in this chapter, we presented a six electrode setup in Fig. 4.1(a) to resolve the device in different ways. A minimum of four input signals are required to resolve the flake into sixteen cells. By increasing the number of cells the resolution accuracy drops. Table 2 encapsulates how the accuracy changes as a function of resolution. Accuracy of the spatial mapping depends on three main parameters: (i) size of the system, (ii) impurity concentration and (iii) number of input readings. In the previous chapter we showed that the error decreases with larger device sizes and with a reduced impurity concentration. Therefore, increasing our device size will make the accuracy values seen in Table 2 significantly better. For example, device sizes in the range of μm are likely to present errors well below 20% when divided into the same sixteen cells. While there are no methodology limitations to considering devices sizes in this range, the computational cost of carrying out a full inversion in a system of that size makes this task unfortunately very challenging at this point in time. However, by increasing the number of electrodes one can generate more input signals which in turn can provide additional information about the spatial distribution of the disorder resulting in the improvement of the accuracy, similarly to the case of generic reconstruction algorithms.

We test the inversion accuracy by defining the error as

$$\alpha = \frac{1}{J} \sum_{j}^{J} \frac{|N_j^{min} - N_j^P|}{N_j^P}, \tag{4.6.1}$$

where N_j^P is the number of impurities in cell j of the parent (input) configuration and N_j^{min} is the corresponding value that minimizes the misfit function. α consists of an average over the total number of cells J, so that large values of J correspond to higher spatial resolution in the impurity distribution. Having considered the cases of $J = 1$, $J = 4$, $J = 9$ and $J = 16$, we may conclude that the inversion accuracy decreases as we attempt to increase the resolution, as seen in Table 2. These values are obtained out of repeated inversions from 100 different parent configurations in

order to achieve statistical significance. The higher the number of cells the higher

# of cells J	Error (α)
1	0.037
4	0.12
9	0.17
16	0.21
25	0.32

Table 2: Accuracy of the sudoku technique as a function of the number of cells used to resolve the device.

the resolution but, unfortunately, the lower the accuracy (roughly a $1/\sqrt{N}$ scaling, where N is the average number of defects in a cell). Given the diverse ways in which a device can be probed and interrogated, it is possible that by increasing the number of readings and/or by selecting more appropriate electrode setups, the accuracy can be further improved.

4.7 SUMMARY

In the previous chapter we presented the inversion tool which can decode the transmission signature of a quantum device to obtain fundamental structural information about the impurities present in system. The misfit function is able to extract occupation and strength of impurities present in the system, without any spatial information about the impurities. A different structural analysis is necessary in order to obtain the spatial mapping of the impurities. Multiterminal set-up allows us to interrogate the system in various ways.

In the first section 4.2, we showed that the misfit function(IP) is independent of the structural setup. This proves that the IP problem only depends on the two-point correlation function of the device and validity of the ergodic hypothesis. Other quantities that can be written in terms of two-point correlation functions are likely candidates to display similar characteristics in the presence of disorder and, therefore, may serve as potential input functions from which spatial mapping of

impurity concentration becomes possible. This may pave the way to using thermal conductivities, spin susceptibilities.

In the next section 4.4, we present a technique to extract spatial mapping of impurities. Multiterminal approach allows us to obtain more than one reading of the same device. By resolving the device in a grid like structure, we can define the misfit function for the specific regions of the device which leads to solving the set of linear equations. Solution to the set of linear equations corresponds to the occupation of disorders present in each cell. This very much resembles of solving a sudoku with the occupation in rows and column obtained from the misfit acting as constraints. To resolve the device in 4, 9 and 16 cells, input transmission spectra are generated by using different combination 6 electrodes. However we stress that this structural arrangement of electrodes and flake is not important to the inversion procedure. We also show that within similar construct misfit function can be used to identify the occupation of impurities in an arbitrary region. However this requires resolving the device in 4,9 and 16 cells. Following this path the sudoku analysis can obtain the spatial distribution of the impurities in the system with good accuracy.

In summary, we have shown that the inversion methodology is capable of identifying the global number of impurities from seemingly noisy two-terminal conductance signals of a 2D quantum device can be extended to determine how such impurities are spatially distributed. The impurity distribution can be resolved into smaller sections of the device, depending on how the local conductance is being probed.

The methodology present in the chapter have been published in the Reference [142].

5

JUNCTION PROPERTIES OF NANOMATERIAL NETWORK

5.1 INTRODUCTION

In chapter 3 and 4, we introduced an inversion technique which can extract fundamental structural information about the scattering centres present in the system. The misfit function tool identifies the occupation, strength and location of the impurities present in the quantum device from seemingly noisy DC conductance signature. We showed that the novel methodology works with great accuracy for various devices of nanoscale dimensions. In this chapter we move on from quantum devices to nanomaterial networks.

Adelung *et al* reported the first use of metallic nanowire network in 1991 [143]. In the report they showed that such devices can be very easily fabricated with speed and at large scale. This was an important achievement in material science. Reducing the bulk material to its one or two dimensional form can alter the material properties significantly [78, 144–146]. A much of the nanoscience deals with engineering of nanomaterials of different as properties. Due to the confinement of electrons quantum mechanics governs properties of material at individual level. When distributed on a flat surface such systems gives rise to the rich physics of electronic propagation between the wires or flake to flake. This adds an extra level of complexity beyond the description of transport across individual devices.

Ease in the fabrication aspect allows the researchers to mix the nanowires or flakes of different materials to derive novel and complex physics. As a result of which such systems have widespread applications from flexible electronics [147] to solar cell [148]. Another interesting application of random nanowire network is the memristive response to the current [62]. Such random nanowire architectures

resembles the brain like processing units called as neuromorphic devices. These networks consists of randomly placed metallic nanowires with dielectric coatings. As a result of which electrical resistance of the system depends on the past behaviour [149]. The electronic transport through nanowire/nanosheet networks depend on the many underlying parameters mainly on the junction properties, wire/flake resistances, connectivity of the network and density [150–154]. Characterization of these networks is normally carried out with the help various microscopy techniques with variety of success. In case of nanowire network SEM imges can provide connectivity of the network and well established modelling techniques can be used to obtain the electronic properties [155]. However, the same can not be said about the nanoflake networks. Formed by the collection of nanodevices, the networks are significantly larger than the devices that we considered previously. As a result, transport across such large-scale networks must be treated differently. Rather than solving the Schrödinger equation to obtain the electronic propagation across disordered devices, we must make use of kirchoff's law to describe the AC transport properties of such networks. More specifically, in this chapter, we study the electronic transport through nanowire/nanoflake network in terms of frequency dependent impedance signature.

The objective of this chapter is to present a tool that can use the impedance signature of a network. The chapter is structured as follows: In the next section we introduce necessary mathematical tools required to model a nanowire/nanosheet network with the help of network theory. We use modified nodal analysis to calculate the impedance between two electrodes from the corresponding Kirchoff matrix. In the following section we introduce the configurational average impedance as the necessary forward modelling aspect of inversion procedure presented in this thesis. We use misfit function to extract information about the junction capacitance mainly. The multivariable misfit function is then introduced which allows us to generalise the formalism to extract more than one bit of information about the underlying graph. The chapter is then summarised in the last section 5.6.

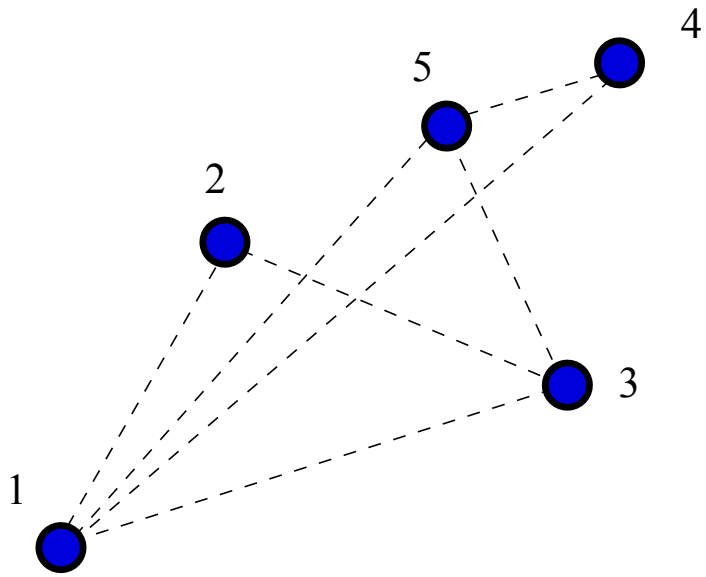

Figure 5.1: A sketch of a simple network. Nodes are represented by blue circles and are numbered 1 to 5. The dotted lines connecting nodes represent the network edges.

5.2 MATHEMATICAL METHODS

Network is a collection of nodes that are connected to one another in some ways. A many body system can be abstracted in the network with edges representing the inter-body interactions and the node defines properties of the individual entity. In this section we present a method to calculate resistance and impedance of an electrical network. Fig. 5.1, shows one simple example of network or graph. Graph is also defined as collection of N nodes and E edges [156]. One of the most interesting feature in graph theory is that nodes and edges can be labelled arbitrarily and independently. In the this section we will study the basic aspects of network theory

5.2.1 *Adjacency Matrix and Kirchhoff's Circuit*

The connectivity of the graph is defined using the adjacency matrix $\boldsymbol{A}$. It is defined as $A_{ij} = A_{ji} = 1$ if nodes i and j are connected, else $A_{ij} = 0$ where $i, j = 1, ..., N$.

Adjacency matrix stores information about the nearest neighbours. It can be defined for the graph shown in Fig. 5.1 as

$$\boldsymbol{A} = \begin{pmatrix} 0 & 1 & 1 & 1 & 1 \\ 1 & 0 & 1 & 0 & 0 \\ 1 & 1 & 0 & 0 & 1 \\ 1 & 0 & 0 & 0 & 1 \\ 1 & 0 & 1 & 1 & 0 \end{pmatrix} \tag{5.2.1}$$

The degree of i^{th} node is the number of neighbours each node has. We can obtain this easily from the matrix $\boldsymbol{A}$, to form corresponding diagonal matrix which describes the degrees of connectivity of a network such that

$$D_{ii} = d_i = \sum_{j=1}^{N} A_{ij} \tag{5.2.2}$$

We can write the Laplacian $\boldsymbol{L}$ as

$$L = D - A \tag{5.2.3}$$

and the Laplacian matrix of the graph 5.1 is given as

$$\boldsymbol{L} = \begin{pmatrix} 4 & -1 & -1 & -1 & -1 \\ -1 & 2 & -1 & 0 & 0 \\ -1 & -1 & 3 & 0 & -1 \\ -1 & 0 & 0 & 2 & -1 \\ -1 & 0 & -1 & -1 & 3 \end{pmatrix} \tag{5.2.4}$$

A weighted edge has a scalar value associated with it and the adjacency matrix takes a slightly different form. This form allows us to encode the network information.

$$A = \begin{pmatrix} 0 & g_{12} & g_{13} & g_{14} & g_{15} \\ g_{21} & 0 & g_{23} & 0 & 0 \\ g_{31} & g_{32} & 0 & 0 & g_{35} \\ g_{41} & 0 & 0 & 0 & g_{45} \\ g_{51} & 0 & g_{53} & g_{54} & 0 \end{pmatrix} \tag{5.2.5}$$

Here, g_{ij} is the weight associated with the edge. The corresponding Laplacian matrix is called as Kirchhoff matrix. In nodal analysis the problem of current transport is solved by identifying the edge weights g_{ij} as the conductance between voltage nodes i and j. calculating the resistance between arbitrary nodes has been long researched problem in science [157–159]. Cserti and collaborators presented a method [160] which uses the Green function technique to calculate the resistance between any arbitary site of a lattice. Remarkably, the problem of finding resistance across a network can be mapped into a tight-binding model used to describe the electronic structure of solids. Coincidently, this matches with what we did previously, since in 2^{nd} chapter we used lattice green function to derive transport properties of a nanodevice. In condensed matter physics this is a well developed and commonly used technique. They derived an expression for the equivalent resistance between any arbitrary two sites of an infinite resistive lattice in terms of the GF elements [161]. They also showed that the method can work equally well in presence of the perturbation with the help of Dyson equation. Another approach was presented by Venezian *et al* in [162] to calculate the resistance between two adjacent nodes on an infinite square grid of identical resistances. This method depends on the superposition of potentials and currents of two one-terminal configurations. The current enters and exits through one node only [163, 164].

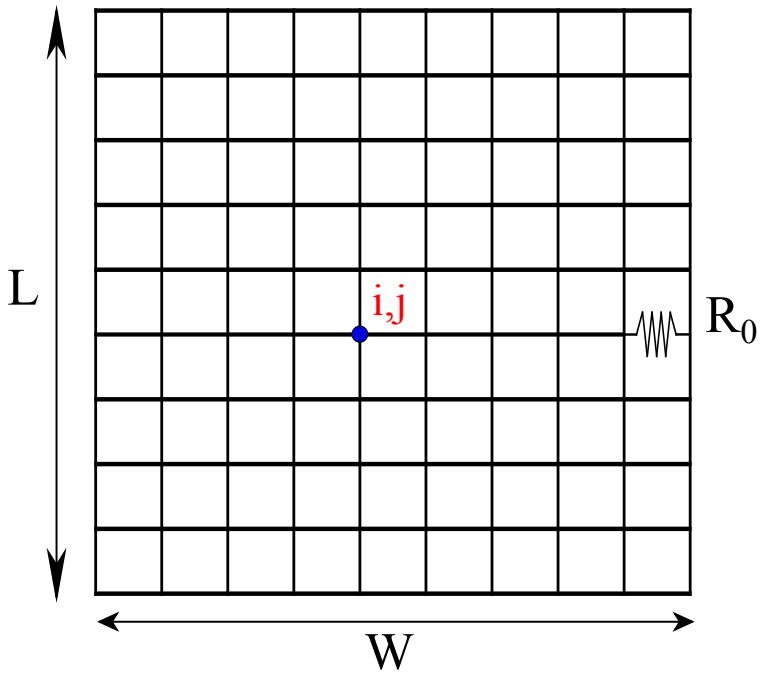

Figure 5.2: A simplified graph of square lattice representing a regular ordered network of dimensions $L \times W$. R_0 is the edge weight of the network representing junction properties of.

Fig. 5.2 shows network in form of a square lattice of length L and width W. Every edge in the lattice is assumed to be a resistor. Now current flowing through node (i, j) is given by the net flow of current from the neighbouring nodes as

$$\begin{aligned} I_{i,j} &= \frac{1}{R}[(V_{i,j} - V_{i+1,j}) + (V_{i,j} - V_{i-1,j}) + (V_{i,j} + V_{i,j+1}) + (V_{i,j} + V_{i,j-1})] \\ &= \frac{1}{R}[4V_{i,j} - V_{i,j+1} - V_{i,j-1} - V_{i+1,j}, V_{i-1,j}] \end{aligned} \tag{5.2.6}$$

$V_{i,j}$ is the electrical potential at node (i, j) and R is the resistance. We can generalise this form to write

$$I_x = \frac{1}{R_0}[\alpha_x V_x - \sum_{\sigma}^{\alpha_x} V_{x+\sigma}] \tag{5.2.7}$$

where, x is the position of site, σ represents the neighbouring nodes and α_x are the total number of nodes surrounding x. In matrix form we can write this as

$$I = \frac{1}{R_0} MV \tag{5.2.8}$$

where I is the current matrix with only two non-zero elements corresponding to injection and extraction of current. Matrix M defines the connectivity of network. To calculate the resistance between two sites i and j, we can write

$$R_{x,y} = \frac{V_x - V_y}{I} \tag{5.2.9}$$

This allows us to write

$$R_{x,y} = R_0(M^{-1}_{x,x} + M^{-1}_{y,y} - M^{-1}_{x,y} - M^{-1}_{y,x}) \tag{5.2.10}$$

Note that $R_{x,y}$ is the resistance between any random two nodes as long as we have information about the connectivity of the graph. Matrix M encodes connectivity of the network. This method of calculating equivalent resistances in networks is a special case of a more general method for calculating nodal potentials and current flows known as Modified nodal analysis [165]. Modified modal analysis method can also be used to accurately describe inductive and capacitive behaviour of the network when subjected to the alternating current as input. Throughout this chapter we will use this technique to calculate the AC response of the network.

5.2.2 *AC Impedance*

Motivated by our experimental colleagues studying the transport properties of nanosheet network, we took the challenge of implementing the inversion technique from impedance signals. Simulating nanowire/nanosheet network is particularly difficult due to the spatial randomness of elements in the network and their impact on network connectivity. To calculate the AC impedance, the random nanowire/-nanosheet network is mapped into the mathematical graph similar to the one presented in Fig. 5.2 [166, 167]. In this case, node weight represents network elements characterized into the junction and material properties. The flexibility offered by the technique presented earlier allows us to calculate the resistance or impedance between any two arbitrary points on the network very easily. Note that Eq. 5.2.10 is

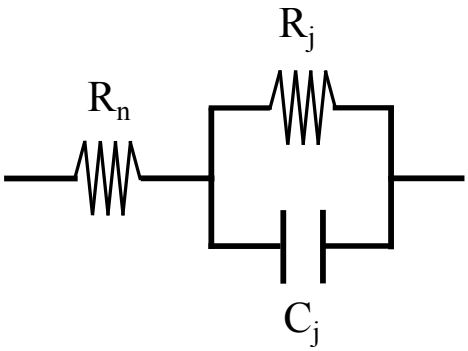

Figure 5.3: Edge in the network can be described using R-RC circuit. R_n is the node(material) resistance, R_j and C_j are the junction resistance and capacitances.

defined for the resistive circuits. However, the expression takes similar form for obtaining the impedance of a network by simply adding a capacitance (or impedance) in parallel to the resistance. Real and imaginary parts of impedance corresponds to the purely resistive and capacitive/inductive elements present in the system. In order to incorporate the capacitive properties of the network, edge resistance shown in Fig. 5.2 is replaced with a R-RC filter. In electrochemistry such circuits are referred as the Randles circuits as shown in Fig. 5.3.

Randles circuit constitutes of three basic elements junction resistance R_j, capacitance C_j encoding the junction information between to nanomaterials and node resistance R_n corresponds to resistance of the nanomaterial. When connected to an AC input source, capacitance exhibits similar form of opposition to the current called as reactance of the circuit $X(\omega)$, defined as

$$X(w) = \frac{1}{i\omega C} \tag{5.2.11}$$

We can write impedance of the equivalent Randles circuit as

$$Z(\omega) = R_n + \frac{R_j X_C(\omega)}{R_j + X_c(\omega)} \tag{5.2.12}$$

Using definition capacitive reactance, we can write

$$Z(\omega) = R_n + \frac{R_j}{1 + i\omega R_j C} \tag{5.2.13}$$

$$Z(\omega) = R_n + \frac{R_j(1 - i\omega R_j C_j)}{(1 + i\omega R_j C_j)(1 - i\omega R_j C_j)} \tag{5.2.14}$$

This leads us to,

$$Z(\omega) = R_n + \frac{R_j}{1 + \omega^2 R_j^2 C_j^2} - i\frac{\omega R_j^2 C_j}{1 + \omega^2 R_j^2 C_j^2} \tag{5.2.15}$$

Here, R_j, R_n and C_j are the junction and wire/sheet resistances and junction capacitances and ω is frequency of the AC supply.

We can now calculate the equivalent AC impedance of a network between two points with edges represented by the Randles circuit. First, we introduce an ordered graph where all the network elements are identical to one another. Each intersection point is mapped onto a voltage node connected by the randles circuit. Throughout this chapter we map the network onto a square lattice graph of dimensions 100×100 and the current is extracted from opposite corners of the graph. Fig 5.4 shows the impedance of such ordered network where $R_n = R_j = 100$ and $C_j = 100$. Panel (a) shows impedance calculated between the voltage nodes located at the opposite corners of an ordered graph resolved in the imaginary and real parts. From Eq. 5.2.15, at $\omega = 0$, the graph has purely resistive behaviour, in panel (b) the real part of the impedance approaches to the sum of wire resistance and junction resistance respectively.

The impedance spectrum derived in panel (a) is also referred as Nyquist plot or Cole-cole plot. Note that another interesting aspect of the impedance data related to an ordered graph is that the data forms semi-circle of radius $(R_n + R_j)/2$. In the next sections we study the effect of randomness and disorders within the network in order to build the inverse problem using impedance data.

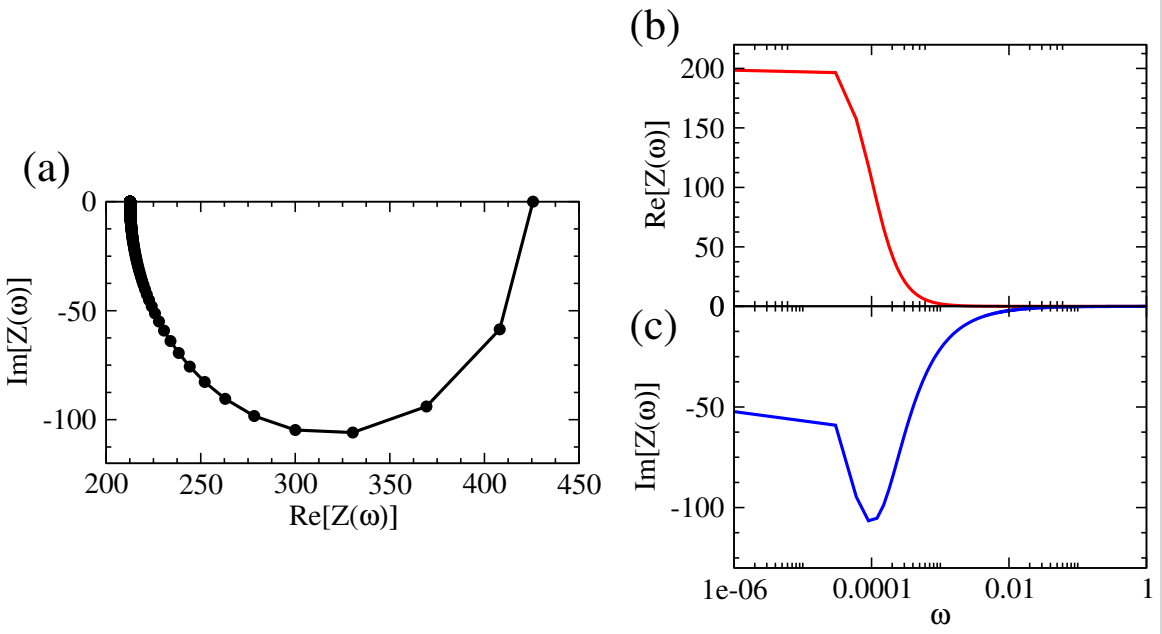

Figure 5.4: Panel (a) shows the impedance of an ordered graph where all the elements are identical to each other. Due to the symmetry of probes the impedance curve forms a semi-circle with radius $(R_n + R_j)/2$. Panel(b) and (c) are the frequency dependent real and imaginary parts of the impedance of a network.

5.3 FORWARD MODELLING

The inverse problem presented in Chapter 3 and 4 uses the conductance data as input to the misfit function. Configurational average is a function of energy and concentration of disorders present in the system. In case of networks, disorder is presented in the form of randomness in distribution of nanomaterials. When distributed on a flat surface randomly, nanomaterials tend to have multiple junctions per wire/flake and each junction exhibits different properties. When mapped on a graph, edges are not identical to one another and circuit parameters are modelled to have normal distribution. The impedance data corresponding to such network depends on the mean as well as standard deviation of the distribution. Fig. 5.5 shows three impedance curves. Black impedance signature corresponds to an ordered network with identical edges of the lattice. Red coloured impedance data corresponds to the circuit parameters following a normal distribution around

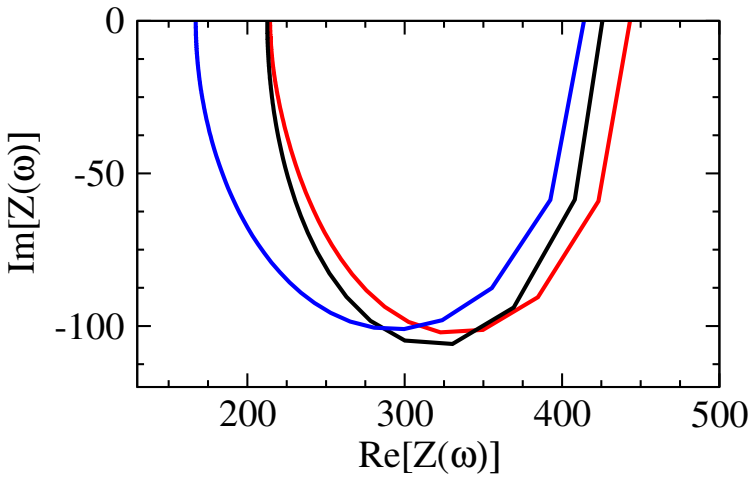

Figure 5.5: Impedance of 3 different graphs corresponding ordered graph in black, disordered graph in red and incomplete graph in blue. All of three curves are encoded with same mean parameters.

the same mean values but do not represent identical edges. Blue impedance data corresponds to a disordered graph with 15 missing edges, *i.e.* the form of description that resembles closely towards the real world nanomaterial network. Note that junction parameters corresponding to the blue curve follow the same distribution of red curve. Shape of the impedance signature remains the same even though they corresponds to 3 different networks. At present to derive the physical properties of a network, Randles circuit are used to find the relation between circuit parameters and the impedance data of the network. Traditionally coherent phase elements(CPE) are used to replace the capacitors in circuit. Impedance of the CPE is defined as

$$\mathcal{Z}_C = \frac{1}{Y_0(i\omega)^n} \tag{5.3.1}$$

here, Y_0 and n are constants. The impedance associated with CPE takes the similar form described in Eq. 5.2.15. Boukamp has shown that the exponent n depends on the distribution of RC values in the equivalent circuit. Rocha *et al* reported that square lattice network can be used in order to map the network in 2D square lattice [65, 168, 169]. This alternative method allows to derive the network properties in a more realistic ways.

The inverse problem presented in this work uses the impedance data to extract important structural information of nanomaterial and junction properties of the underlying network. We present the methodology using a simplified graph of square lattice of dimensions 100×100 representing a random nanomaterial network. In the following sections we introduce the elements necessary for the misfit function formalism.

5.3.1 *Configurational Average*

Configurational average impedance of a network is the average over M different graphs with the same mean and standard deviation of junction parameters. There are 3 variables on which the impedance of the network depends as shown in Eq. 5.2.15, R_n, R_j and C_j. For simplicity we assume zero to low deviations in the node resistances, *i.e.* we assume material resistance remains constant in entire network. Main contribution in the electrical properties of the nanowire network is coming from the junction resistance and capacitances which follows the normal distribution with mean set at a fixed value. However, in the following sections we will relax this constraint to generalise the technique. First we define the ca as a function of the spread of the junction capacitance only. Following the same procedure presented in chapter 3 we write the ca impedance,

$$\langle \mathcal{Z}(C_j^\sigma, \omega) \rangle = \frac{1}{M} \sum_{n=1}^{M} \mathcal{Z}(\omega) \tag{5.3.2}$$

Here, $\mathcal{Z}(\omega, C_j^\sigma)$ is the ca impedance defined for $R_j^\mu = C_j^\mu = 100$ and $R_j^\sigma = 50$. Note that impedance has real and imaginary part. From Eq. 5.2.15 we can state that in order to obtain information about the capacitance of the network we need to look at the imaginary part of the impedance mainly.

Fig. 5.6 shows the ca impedance curves as a function of the standard deviation of the distribution. Different coloured plots corresponds to the ca carried out at

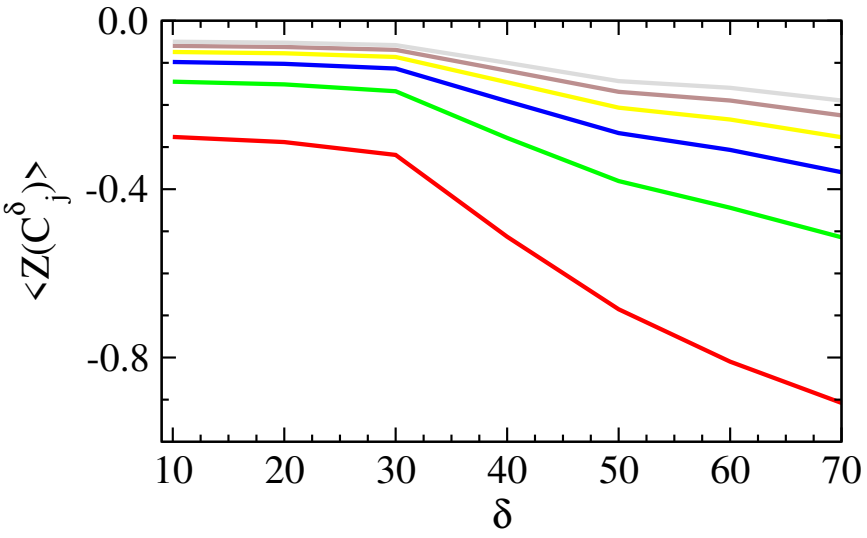

Figure 5.6: Imaginary part of the configurational average impedance of disordered graphs plotted as a function of the spread of capacitance.

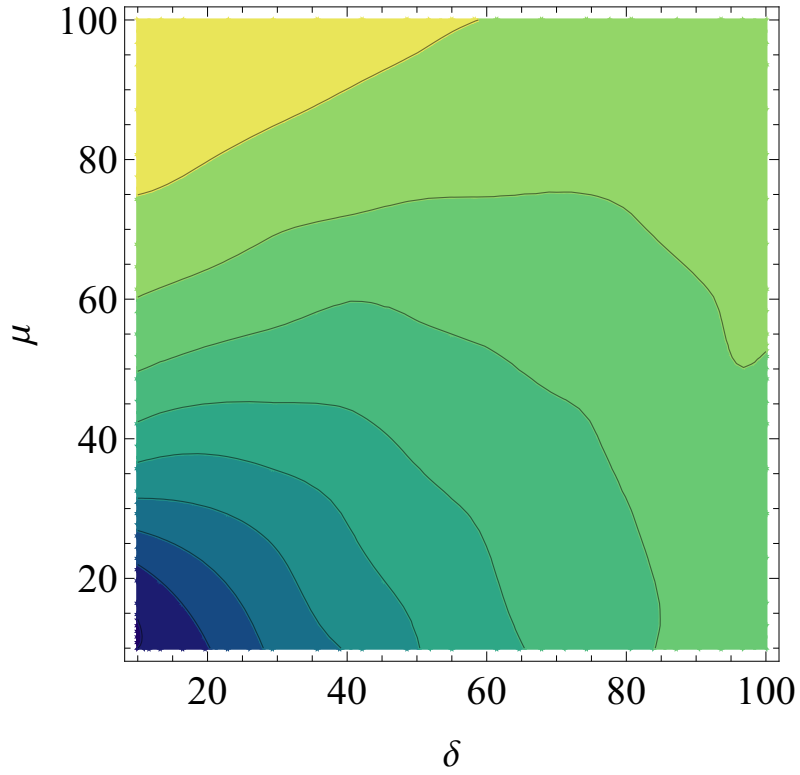

Figure 5.7: Imaginary part of the configurational average impedance plotted as a function of both mean and spread of the junction capacitance.

different frequencies. It is important to note that ca follows the same linear trend we observed in the case of impurity concentration in nanodevices, Fig. 3.3(a). This linear

behaviour was important for the inversion procedure as this allowed us to describe the average of two point correlation function in terms of its main variables. When carried out for the both parameters, *i.e.* mean and standard deviation. We observe similar behaviour. In this case the ca is now function of both standard deviation. Another important variable in the ca procedure is the number of configurations M. For the ca calculations carried out in this chapter $M = 100$ configurations are sufficient to achieve necessary statistical significance. In the next section we introduce the single variable misfit function.

5.4 MISFIT FUNCTION

In chapter 3, energy dependent conductance signature is used as an input signal to the misfit function which allows us to extract concentration of impurities present in the system. In case of nanomaterial network, different junctions properties which are associated with the connectivity of the network are responsible for unique impedance signatures. The inversion method revolves around extracting information about the junction parameters. The misfit function depends on the energy integration as conductance of the system smoothly depends on it. Similarly we make use of the frequency dependent impedance signature of network. In addition to this impedance data can be resolved in two frequency dependent components, real and imaginary. Using Eq. 5.2.15 we can state that the contribution to the imaginary part of the impedance signature comes from the junction parameters. This contribution manifests in the form of deformation of impedance semi-circle observed in the experimental data as well as derived impedance signature. [170–173].

In the previous section we calculated the ca impedance, when compared with the corresponding imaginary part of the input impedance function, the absolute deviation is plotted as a function of the spread of the junction capacitance in Fig. 5.8(a). Note that the flat feature of the deviation does not reveal any information about the spread of the junction capacitance when measured at a fixed frequency.

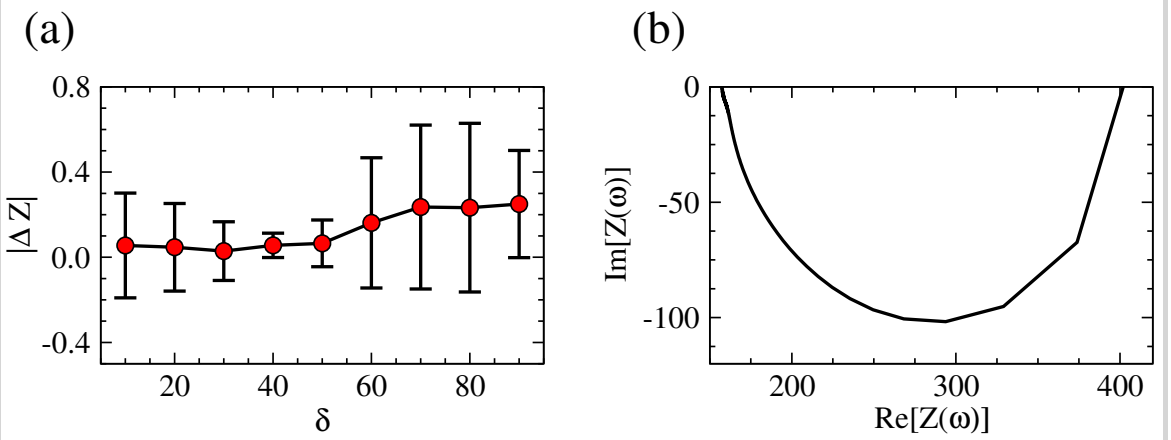

Figure 5.8: Panel (a) shows the absolute value of deviation between the input impedance and the ca impedance as a function of standard deviation at a fix. Panel(b) shows the deformed input impedance signature considered for the inversion procedure.

Error bars corresponds to 200 different frequency points on the impedance spectrum. We can now define the misfit functions with impedance data as the input as

$$\begin{aligned} \chi(\sigma) &= \frac{1}{\omega_+ - \omega_-} \int_{\omega_-}^{\omega_+} d\omega \left[\mathcal{Z}(\omega) - \langle \mathcal{Z}(\omega, \sigma) \rangle\right]^2 \\ \mathrm{Im}[\chi(\sigma)] &= \frac{1}{\omega_+ - \omega_-} \int_{\omega_-}^{\omega_+} d\omega \left[\mathrm{Im}[\mathcal{Z}(\omega)] - \langle \mathrm{Im}[\mathcal{Z}(\omega, \sigma)] \rangle\right]^2 \end{aligned} \tag{5.4.1}$$

When plotted as a function of the standard deviation the misfit function generates a minimum which correctly coincides with the actual standard deviation responsible for the input function.

Fig. 5.9(a) shows a distinctive minimum at $\sigma = 40$. When carried out for 100 different configurations, *i.e.* the misfit function correctly points out the standard deviation in the distribution of the junction capacitors accurately as shown in Fig. 5.9(b). It is important to note that the ergodic hypothesis remains valid in this case. AC impedance of a network can be described as a two point correlation function which depends on frequency of the input current. The integration over frequency is analogous to considering a wider universe of disorder configurations. As a result of which the misfit function develops a minimum when integrated over sufficient large bandwidth. Even though a detailed mathematical analysis of effects

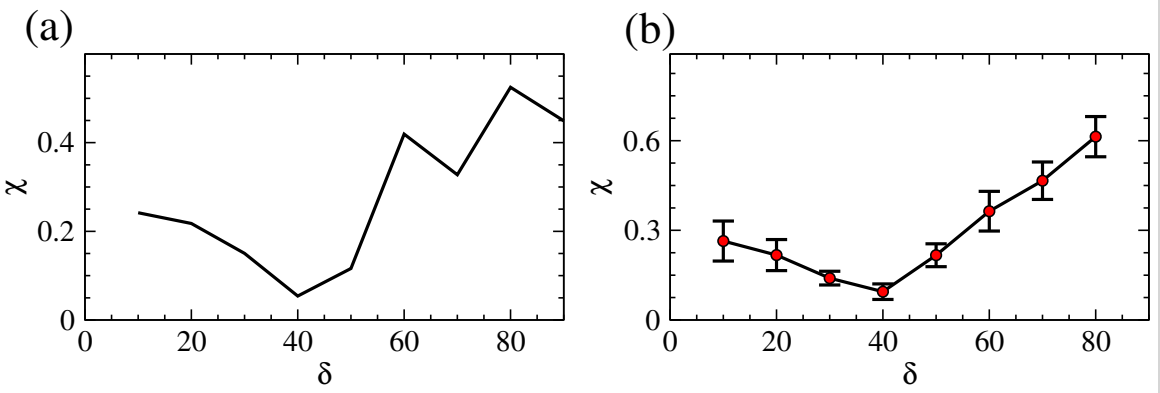

Figure 5.9: In panel (a) Misfit function defined for the input impedance in Fig. 5.8(b) shows distinctive minimum at the correct value. Panel(b) shows the accuracy of the misfit function when carried out for 100 different configurations.

of junction parameters on impedance is out of the scope of this work, the inversion procedure remains valid for macro-scale systems.

The misfit function described in Eq. 5.4.1 depends on the frequency integration limits. In Fig. 5.4(a), Impedance of an ordered network is plotted in its real and imaginary parts. Solid black dots along the curve represents frequency points for which impedance is defined. Imaginary part shows asymptotic decline to zero with increase in frequency. We observe that dampening of the impedance curve takes place at very low frequencies, $\omega \leqslant \frac{1}{R_j C_j}$. As a result accuracy of the inversion procedure relies heavily on low frequency part of the spectrum.

Following the same technique presented in this section, the misfit function can extract information about the distribution of junction resistance using the real part of the impedance data. For an ordered network, the Cole-Cole plot *i.e.* impedance spectrum forms a semi-circle at $(R_n + R_j)/2$. However, in disordered network asymmetry in the junction properties is responsible for the broadening of the impedance data. We can write the relevant misfit function as

$$\mathrm{Re}[\chi(\sigma)] = \frac{1}{\omega_+ - \omega_-} \int_{\omega_-}^{\omega_+} d\omega \left[\mathrm{Re}[\mathcal{Z}(\omega)] - \langle \mathrm{Re}[\mathcal{Z}(\omega, \sigma)]\rangle\right]^2 \tag{5.4.2}$$

Note that in Eq. 5.2.15, Real part of the impedance depends on the node and junction resistances and junction capacitance. Thus the distribution of junction capacitance

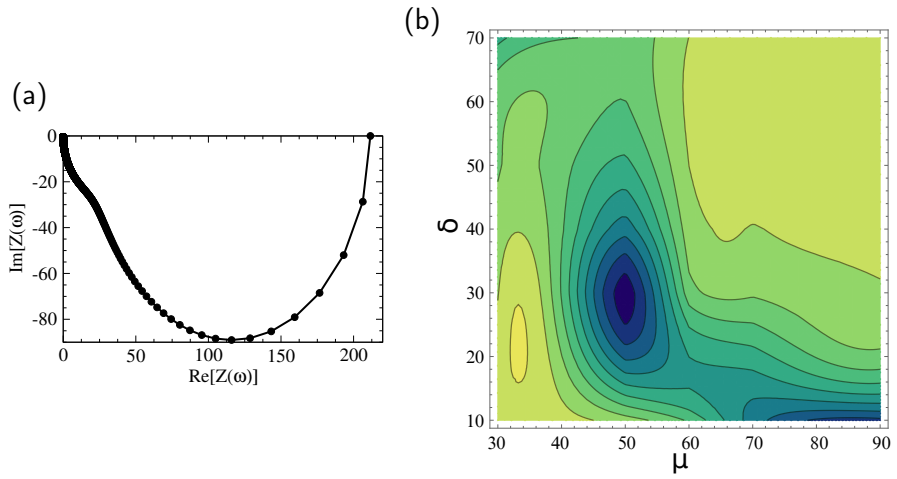

Figure 5.10: Panel(a) shows the compressed input impedance signature of a disordered graph. Panel(b) shows the corresponding misfit as a function of mean and standard deviation of the graph at the same time.

is necessary to extract information about the junction resistances. To do so we now introduce the multivariable misfit function to extract information about the mean and spread of the junction capacitance.

5.5 MULTIVARIABLE MISFIT FUNCTION

In the previous section we defined the misfit function to extract the spread of the distribution of capacitance from the impedance signature of a disordered network. While doing so the misfit function was variable of standard deviation in junction capacitance.

In this section, we define the misfit function to extract mean and standard deviation at the same time. We can write it as

$$\chi(\mu,\sigma) = \frac{1}{\omega_+ - \omega_-}\int_{\omega_-}^{\omega_+} d\omega \Big[\mathrm{Im}[\mathcal{Z}(\omega)] - \langle \mathrm{Im}[\mathcal{Z}(\omega,\mu,\sigma)]\rangle\Big]^2 \tag{5.5.1}$$

Following the same algorithm presented in the previous section, we begin with an arbitrary impedance signature, however without any information about distribution

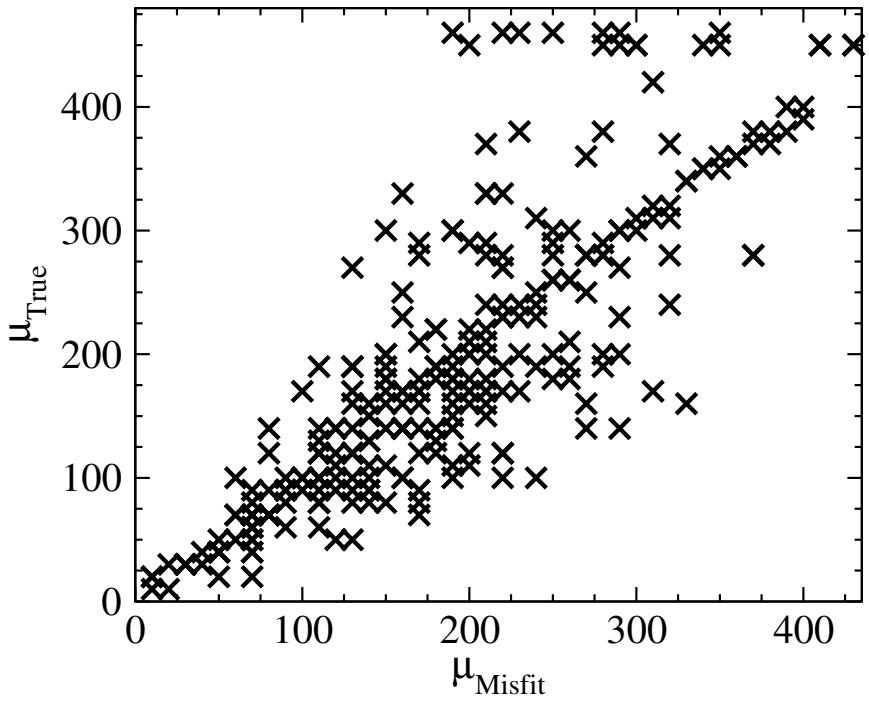

Figure 5.11: Accuracy of the inversion procedure to obtain the mean junction capacitance of a graph when carried out for 200 different samples. μ_{True} is the actual mean capacitance of the system vs μ_{misfit}, mean obtained from inversion.

of capacitance in the network. Fig. 5.10(a) shows the impedance signature of a square lattice network of dimensions 100×100. A 2D contour plot of misfit function χ is plotted in Fig. 5.10(b). A distinctive minimum is visible coinciding with the actual mean and standard deviation values of the network. It is important to note that the same method can be easily extended to obtain junction resistance and node resistance parameters using both imaginary and real parts of impedance data.

When carried out for 200 different sample networks the misfit function was able to predict the correct characterization of the junction parameters. When inversion carried out with mean (μ) as main variable Fig. 5.11 shows accuracy of the procedure. Most of the inverted solutions lies along the $y = x$ line, where x-axis defines the true mean values of the junction resistance.

5.6 SUMMARY

In this chapter we extended the inversion formalism to the nanomaterial network. Junction properties play a key role in the electronic transport of the nanowire/-nanosheet networks along with connectivity and density. In impedance spectroscopy, the network parameters are modeled and characterized using Randles circuit and coherent phase elements (CPE). Traditionally a linear chain of Randles circuit with CPE replacing the capacitor is used to model a complex 2-D network. Although, this model is simple enough to describe the experimental data, the physical interpretation of a CPE is well debited. We introduce an alternative method to extract the junction parameters specifically distribution of junction capacitance from the impedance data. To do so we map the network onto a 2-D graph, which provides extra degrees of freedom to describe the system.

In the first section of the chapter we briefly introduced necessary elements of network theory to calculate the impedance of a 2D mathematical graph using Kirchhoff laws and modified nodal analysis. Randomness and disorder is then introduced to the ordered graph by changing the R-RC elements of circuit assigned to the edge of a graph. Disorder is introduced by changing the edges of the graph. This is done by assigning the parameters to a follow a predefined distribution. This mathematical graph acts as the proxy to the experimental data. The inverse problem presented uses the the impedance signal of such graph to determine the junction properties. We mainly focus on the capacitive aspect of the junction. Real part of the impedance encodes information about the node resistance and junction resistance as the plot forms semicircle with centre at $R_n^\mu + R_j^\mu/2$. Also, at zero frequency the network purely resistive the equivalent resistance of a network is a sum of junction and node *i.e.* $R_{total}^\mu = R_n^\mu + R_j^\mu$, forming second equation for two resistive variables. We studied the dampening of the inductance data due to large distribution in the junction capacitance. ca impedance also shows a linear behavior as a function of the spread of the capacitance. In the following section we use the misfit function to extract the standard deviation. The multivariable misfit function allows us to extract

the mean and standard deviation of the junction capacitance distribution without availing any prior information.

6

SUMMARY AND FUTURE WORK

In this thesis, we presented an inversion tool that extracts fundamental underlying information about the system from seemingly noisy DC conductance signature of a quantum device and AC impedance of a nanowire/nanosheet network. For the situations in which we know the initial conditions of the system of study, the method may sound unimpressive. However, we do not have access to initial conditions, the inversion tool finds a way to retrieve the system initial setup by inspecting the response function of the system subjected to the perturbations. The so called "misfit function" reveals minima at the locations in the phase space parameter that correspond to the concentration of the scattering centres present in quantum devices and distribution of junction parameters of a random nanowire/nanosheet network. The method presented in this thesis is scalable, robust and can be built around numerous parameters. The technique provides good accuracy for the nanosystems of various materials as well as complex nanoowire/nanosheet network. Furthermore we showed that the spatial mapping of impurities present in the system is possible in a multi-terminal setup. We envisage this inversion methodology being implemented beyond conductance measurements which will provide a framework for visualising impurities from simple measurements of different properties. In this chapter, we present the summary of the thesis and possible applications of this versatile tool.

6.1 THESIS SUMMARY

In chapter 1, we provided a brief overview to the thesis that provided context to the IP described in the following chapters. We argued that the quantum mechanics is a fertile ground to develop the IP. The misfit function tool is an alternative characteri-

zation tool that is relevant to the current experimental infrastructure. We discussed the structure of the IP and necessary aspects of the tool to be relevant for the recent developments in the characterization of nanoscale devices and nanowire/nanosheet networks. The main goal of the thesis was presented in the chapter motivating the reported research.

Chapter 2 defines the mathematical tools and background required to understand the electronic transport through mesoscopic systems. We presented the Green function formalism which is used throughout this thesis for variety of materials and networks. We derived the Dyson equation and the recursive algorithm to build the pristine and discorded systems. We studied the electronic structure of graphene which is used as a go to material in this work. The Landauer-Büttiker formalism presented in this chapter is used to calculate the DC conductance of the system, a key quantity for the inversion procedure. We studied armchair and zigzag-edged graphene nanoribbon systems with the help of the Landauer-Büttiker formalism and DOS obtained by recursive GF technique. Finally we provided a simple algorithm to calculate the DC conductance of the system which is an essential part for the following chapters.

In Chapter 3, The forward and inverse modelling techniques were briefly introduced. We defined the forward modelling technique to calculate the electronic conductance of 1-D chain of atoms with the help of kubo formalism for a standard two terminal transport set-up. We define the configurational average conductance of a system to understand the statical significance of the randomly placed impurities in the system. The misfit function defined in the next section extracts information about the concentration of impurities present in the system from seemingly noisy conductance signature of the device. We argue that the method rests on an ergodic hypothesis. The misfit function is akin to a running average and, therefore, it indirectly corresponds to considering a larger number of disorder realizations in the configurational-average (CA) part of the calculation. The ergodic hypothesis implies that a running average over a continuous parameter upon which the conductance depends is equivalent to sampling different impurity configurations. In the

following sections we explore the scalability of the misfit function. It can be used to accurately extract information about the concentration and strength of multiple types of impurities. We show that the tool is model independent with the help of the calculations carried out within density functional theory. Finally, The misfit function depends on (1) the bandwidth considered for the integration, (2) number of configurations used in CA, M and (3) concentration of impurities present in the system. We found that more that 20% of available bandwidth is enough to obtain the error below 10%. Number of configurations considered for CA depend on the type of host material, however $M \approx 10^3$ are enough to obtain good accuracy. We also show that the IP tool can extract information about concentrations upto 10% present in the system with very low error.

In chapter 4, the flexibility of the tool is tested in the multiterminal setup. We also show that, in multiterminal setup and using more than one input reading it is possible to resolve the device in 4 cells. We showed that the misfit function can extract number of impurities present in part of the device when constrained by another misfit function which extracts total occupation of impurities. We show that this can be used to improve the resolution of the device in 9 and 16 cells. While solving the system of linear equation to obtain occupation in each cell resembles with the sudoku puzzle. We use graphene nano-flake embedded with 50 impurities as a case study. We were able to map the impurities in 16 cells with a very small error. We also show that the IP problem is independent of the electrode-system contact geometry.

In Chapter 5, we defined the inverse problem for random nanowire and nanosheet networks. We presented the network theory necessary to calculate the electronic transport properties. We obtained the electrical resistance and impedance of an ordered and random nanowire network using Kirchhoff's matrix. Randomness of the network is characterized by changing the junction properties of nanowires. The frequency dependent impedance signature of the network acts as the input function to the inversion procedure presented in the following sections. We showed that it is indeed possible to extract distribution of junction resistances and capacitances.

We also extract connectivity of the nanowire/nanosheet network using the same input impedance signature. In the end we conclude with an observed universal behaviour of the network which can also be used as another tool to obtain the capacitive distribution of the network.

6.2 ONGOING PROJECTS

6.2.1 *Characterization of edge disorders in zigzag Graphene Nanoribbon*

Graphene nanostructures are known to manifest different electronic properties than extended graphene. Armchair edged nanoribbons tend to develop bandgap that is directly linked with the width. Zigzag edged ribbons are generally metallic in nature and expected to host spin-polarised edge states [174]. The edge states if the zigzag nanoribbons are predicted to have ferromagnetic properties along the edges and antiferromagnetic coupling between the edges [175, 176]. Recent studies have shown that introducing perturbation in ordered and disordered fashion along the edges of ZZ edged nanodevices are proposed to have many applications in spintronics [177, 178]. The inversion technique in this thesis provide an alternative way to characterize the effect of perturbation on the spin transport. For this we consider a graphene zigzag edged system as shown in Fig. 6.1. Perturbation in form of vacancies are itched along the edge of the graphene nanoribbon.

The inversion procedure presented in chapter 3 uses the transmission signature of a device to extract information about the underlying hamiltonian. To extract the occupation of vacancies using spin polarised current, we define the misfit function as

$$\chi_s(N) = \frac{1}{\mathcal{E}_+ - \mathcal{E}_-} \int_{\mathcal{E}_-}^{\mathcal{E}_+} dE \left[T_s(E) - \langle T_s(E, N)\rangle\right]^2 \tag{6.2.1}$$

here, T_s is the spin polarized transmission and $\langle T_s\rangle$ are the spin polarized average transmissions defined as a function of vacancy concentration.

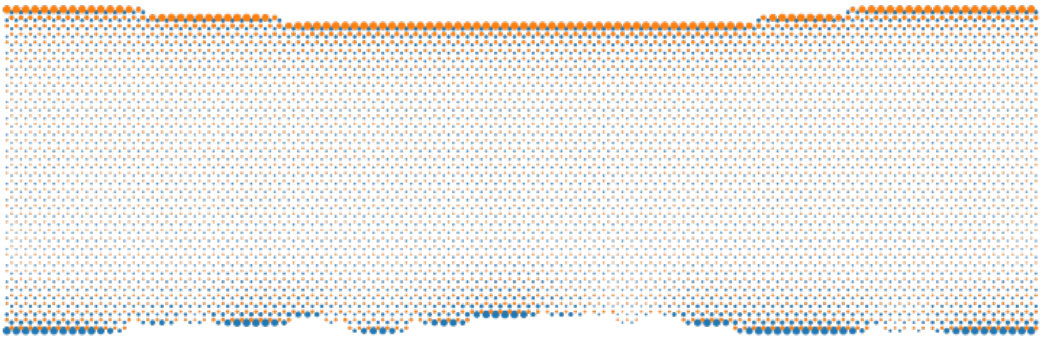

Figure 6.1: Schematic of graphene nanodevice with ordered itching of vacancies on one edge and disordered itching on another. Orange and blue colour dots corresponds to spin polarization of corresponding carbon atoms.

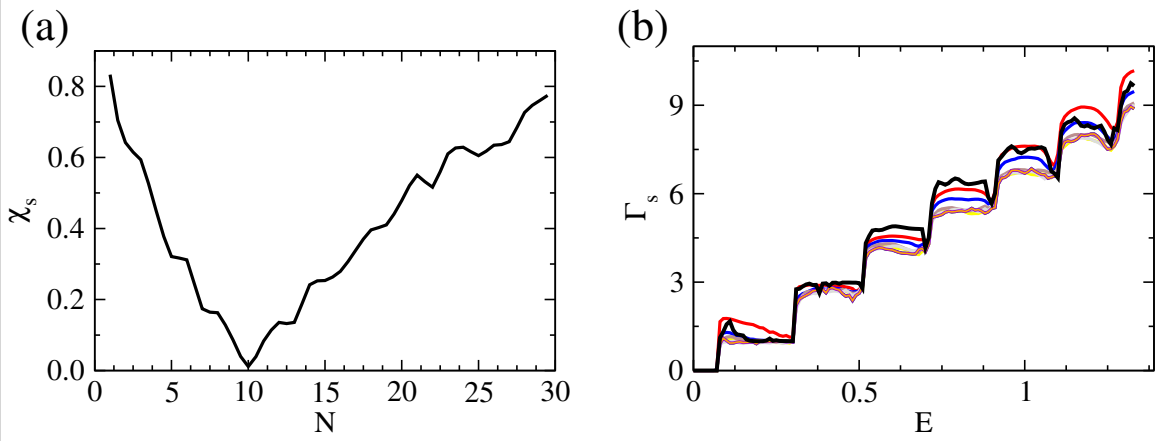

Figure 6.2: Panel (a) shows the misfit function plotted to extract occupation of vacancies on the top edge. The minimum corresponds to the true number of impurities present on the top edge of a ZGNR system. Panle(b) depicts the configurational average transmissions and in thick black input transmission spectrum used for the misfit function plotted in panel (a).

In Panel (a) of Fig. 6.2, misfit function is plotted as a function of vacancy concentration. Panel Fig. 6.2(b) depicts the spin polarised transmission signature of ribbon in black, along with the CA transmissions. Near Fermi energy the main contribution to the transmission comes from the edge states and perturbation in the region. We can define the misfit function with integration only in first two plateau of the conductance, which correctly points out the number of vacancies present on the edges. When integrated over the entire available bandwidth the misfit function

develops minimum at the total number of vacancies present in the system allowing us to calculate the asymmetry in ribbon with the constrain $N_{total} = N_{top} + N_{bottom}$.

Ability to distinguish the disorder concentration on edges of graphene nanoribbon using inversion technique can be certainly used as an alternative method to STM like techniques. Chapter 4 introduces a way to obtain spatial information about the impurities present in the system. The spin polarized transmission encodes the disorder concentration and position of vacancies in the system. The question we put forward is: can inversion technique differentiate between the ferromagnetic and antiferromagnetic ribbons. Further more can the technique extract information about local magnetic moments of a device by analysing the spin polarised transmission signatures.

6.2.2 *Target Oriented Inversion for Quantum Devices*

In geophysics, full waveform inversion (FWI) models are widely used and well developed with the help of Green function formalism. Similarly, in quantum mechanics patched GF provide one way to understand the effect of a particular patch on electronic properties of a device. Motivated from the work presented in chapter 4, such target oriented inversion can provide an alternative way to the sudoku inversion. The L-B formalism is defined in terms of the non-diagonal GFs between the two leads. For a specific target, dyson equation can be used to treat the target as a single entity and allows us to calculate the necessary non-diagonal GF terms for the conductance derivation. Freezing the area surrounding the target, we can probe effect of impurities present in the target region.

6.3 FUTURE WORK

In this thesis, we presented a versatile inversion tool which can extract fundamental structural information of a quantum device or random nanowire/nanosheet net-

work. The inversion methodology uses a two point correlation function in form of conductance or impedance of nanodevices and networks respectively. Many observable quantities can be described as a two point correlation function. In Duarte *et al* [179] we showed that the inversion procedure presented in this thesis works equally well for optical conductance signatures. We suggest that the inversion methodology can be adopted to interrogate the thermal conductivity signatures. Spatial mapping of scattering centres is another important aspect of the inversion procedure presented in this work. In the next section we discuss the possible application of the inversion technique.

6.3.1 *Magnetic Properties*

The misfit function can be written in terms of many degrees of freedom, enabling us to interrogate the disordered structures in creative ways. For instance, inclusion of the spin degrees of freedom wides the possible applications of this inversion tool. The misfit tool can interrogate the the system through spin-susceptibility, magnetoresistance or spin polarised conductance. Eq. 3.3.2, misfit function requires an integration over energy as the input conductance signature is also a function of same. The ergodic hypothesis remains valid for alternative integration variables such as magnetic field or gate voltage. Magnetic hysteresis curves can be used as an input function to derive magnetic properties of underlying hamiltonian.

Materials containing randomly distributed magnetic impurities have their own magnetisation dependent on the orientation of all the magentic moments. The interaction between the magnetic moments can be described with the help of various mechanism like direct exchange coupling and RKKY interaction. A parameter that characterises the angle distribution of magnetic moments as the variable for the misfit function can define the total energy of the system dependence on the applied field. Using this quantity as the input function, the inversion tool can extract clear information about the angular distribution of magnetic moments and the interaction mechanisms present in the system [180–184]. The magnetoresistance

is a key quantity in spintronics. Magnetoresistance is the relative change in the resistance as a result of an externally applied magnetic field. It has instrumental roles in the reading and writing of magnetic information in nanoscale device. It can be characterised by change in the resistance of the device as a function of the external magnetic field. Using this as the input function misfit function can identify what combination of magnetic components are required to produce exactly same signal. Remarkably this will be a possible strategy to engineer materials that display a desirable property [185–188].

Magnetic imaging technique can be implemented in a sudoku-style geometry. Measurements of spin-polarised currents across system-wide multi-electrodes can be inverted to describe the magnetic texture or the spatial distribution of the magnetisation, something that otherwise would require magnetic force microscopy or spin- polarised scanning tunnelling spectroscopy techniques.

6.3.2 *Thermal Properties*

The thermal conductivity of nano-materials can be calculated using a somewhat similar approach to the one used for electronic transport, namely the Kubo-Green formalism. The heat current that arises due to a temperature gradient depends on the thermal conductivity, which in turn is expressed as a Two point correlation function. Despite the difference between the two types of transport, there are many similarities that suggest that the inversion procedure is suitable to extract information from heat-related response functions.

6.4 NETWORK PROPERTIES

In Chapter 5, we presented the inversion procedure to extract information about the junction parameters of a nanowire/nanosheet network. Such networks have wide range of applications due to the flexibility offered by the control over the

network properties. Nanowire networks are promising memristive architectures for neruomorphic applications. Recently Manning et al in [62] reported winner takes all conducting path emergence which spans entire network. The memory stored in the conductance state is distributed across the network but encoded in specific connectivity pathways. Characterization of such networks is an important but difficult task. The inversion tool presented in this thesis provides a way to determine the junction parameters, allowing a way to engineer novel nanowire systems. This process can alos be used to understand the effect of the memcapacitive element of junction memristors [189]. Barwich et al in [190] examined the network morphology and conductivity in the nanosheet networks. Characterization of such networks is a difficult process which also involves electrical analysis. This can be used as an input to the misfit function which can extract not only the junction properties but also connectivity of the nanosheet networks. The misfit function is a simple characterization technique which can extract various parameters and provide a way to manipulate the systems as per the requirement.

Part I

APPENDIX

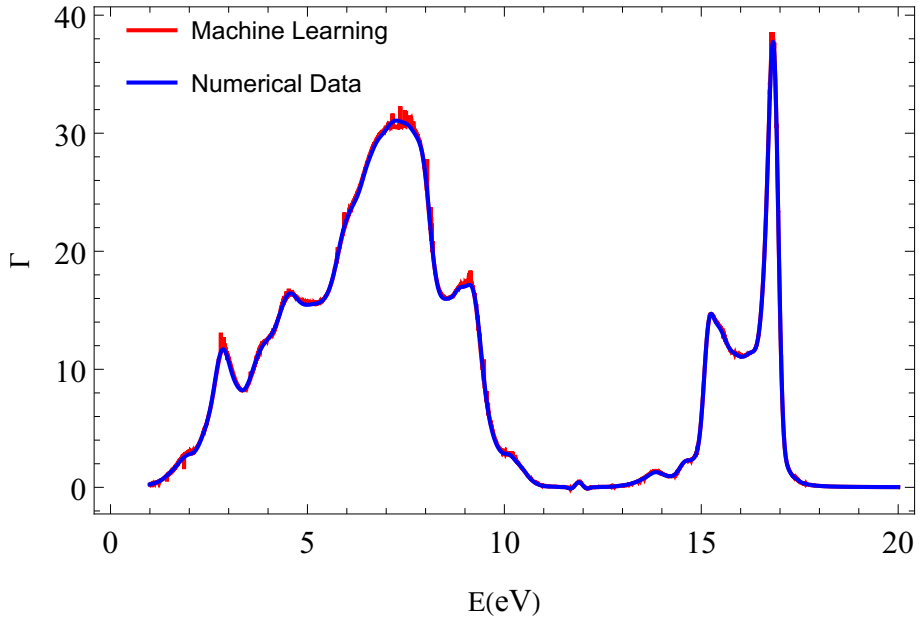

Figure A.1: Configurational average corresponding to 8% disorder randomly distributed in the device represented in Blue. In Red, ML optical conductivity shows very good prediction with the numerical result.

A

INTERPOLATION METHOD FOR CA

To demonstrate the agreement between minimizing concentration of χ and the actual disorder concentration the configurationally averaged (CA) conductance is expanded to linear order in n as [191]

$$\langle \Gamma(E, n) \rangle = \Gamma_0(E) - \beta(E)\, n, \tag{A.0.1}$$

where $\beta(E)$ is the derivative of $\langle \Gamma(E, n) \rangle$ with respect to n evaluated at $n = 0$.

Satisfactory accuracy levels of the inversion method relies on carrying out the CA part of the calculation with a good resolution in terms of n but the computational costs of doing so with a large number of concentration points by brute force is substantial. The approximation in Eq.3.3.4 provides a doorway to generate CA

for more values of n using interpolation supported by machine learning. Fig. A.2 shows a misfit function generated using numerical (red) and interpolated (black) data. This model studies the CA data (CA corresponding to red points) to generate CA spectrum for different values of n (corresponding to black points). Eq.3.3.4 is valid for a small range of concentration but it starts to move away from the linear nature as disorder concentration increases. This results in failure to understand the caveats of CA spectrum.

Machine Learning (ML) becomes a very handy tool in order to generate CA conductance spectrum. It computes CA spectrum without losing details of the conductance quantum signatures and at a low computational costs. Fig. A.1 shows very good prediction of CA optical spectrum corresponding to 8% disorder with numerically calculated optical spectrum in blue. 7 datasets corresponding to different concentrations of numerically calculated CA spectrum were used to train the model. Same model is used to generate rest of the CA points shown in black in Fig. A.2.

Wolfram Mathematica provides predefined ML tools called Predict and Classify to define a model. Both tools can generate the output corresponding to concentration and energy in this case. Model uses numerically computed CA spectrums as the training examples. Spectrum provides large number energy points to train the model. It is worth pointing out that while more sophisticated ML techniques are available to model quantum transport [101, 102], this is by no means an essential ingredient of this inversion method but one that can speed up the inversion and improve its accuracy.

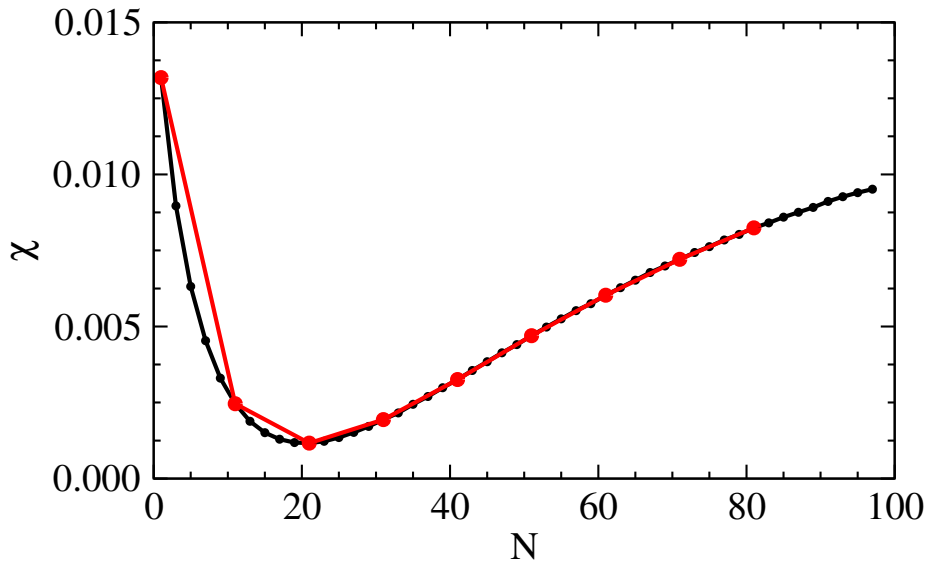

Figure A.2: Misfit function for the interpolated(black) and for the numerical data (red). The model still predicts the minimum correctly while providing more resolution around it, allowing for fine probing different parent configuration concentrations with lower computational cost.

BIBLIOGRAPHY

[1] W. Smart, "John couch adams and the discovery of neptune," *Nature*, vol. 158, no. 4019, pp. 648–652, 1946.

[2] K. Chadan and P. C. Sabatier, *Inverse problems in quantum scattering theory*. Springer Science & Business Media, 2012.

[3] G. Chavent, *Nonlinear least squares for inverse problems: theoretical foundations and step-by-step guide for applications*. Springer Science & Business Media, 2010.

[4] J. Maillet and V. Terras, "On the quantum inverse scattering problem," *Nuclear Physics B*, vol. 575, no. 3, pp. 627–644, 2000.

[5] J. Hadamard, *Lectures on Cauchy's problem in linear partial differential equations*. Courier Corporation, 2003.

[6] L. A. Takhtadzhan and L. D. Faddeev, "THE QUANTUM METHOD OF THE INVERSE PROBLEM AND THE HEISENBERG XYZ MODEL," *Russian Mathematical Surveys*, vol. 34, pp. 11–68, oct 1979.

[7] R. Weder, "Inverse scattering for the nonlinear schrödinger equation ii. reconstruction of the potential and the nonlinearity in the multidimensional case," *Proceedings of the American Mathematical Society*, vol. 129, no. 12, pp. 3637–3645, 2001.

[8] V. Enss and R. Weder, "The geometrical approach to multidimensional inverse scattering," *Journal of Mathematical Physics*, vol. 36, no. 8, pp. 3902–3921, 1995.

[9] T. Aktosun and R. Weder, *Introduction*, pp. 1–17. Cham: Springer International Publishing, 2021.

[10] M. Bertero and M. Piana, *Inverse problems in biomedical imaging: modeling and methods of solution*, pp. 1–33. Milano: Springer Milan, 2006.

[11] J. Virieux, A. Asnaashari, R. Brossier, L. MÃ©tivier, A. Ribodetti, and W. Zhou, *An introduction to full waveform inversion*, pp. R1–1–R1–40. 2017.

[12] J. Tromp, D. Komatitsch, and Q. Liu, "Spectral-element and adjoint methods in seismology," *Communications in Computational Physics*, vol. 3, no. 1, pp. 1–32, 2008.

[13] E. T. F. Dias and H. Vieira Neto, "A novel approach to environment mapping using sonar sensors and inverse problems," in *Towards Autonomous Robotic Systems* (C. Dixon and K. Tuyls, eds.), (Cham), pp. 100–111, Springer International Publishing, 2015.

[14] M. Lassas, L. Päivärinta, and E. Saksman, "Inverse scattering problem for a two dimensional random potential," *Communications in mathematical physics*, vol. 279, no. 3, pp. 669–703, 2008.

[15] T. Hoang, C. Gerving, B. Land, M. Anquez, C. Hamley, and M. Chapman, "Dynamic stabilization of a quantum many-body spin system," *Physical Review Letters*, vol. 111, no. 9, p. 090403, 2013.

[16] E. Chertkov and B. K. Clark, "Computational inverse method for constructing spaces of quantum models from wave functions," *Phys. Rev. X*, vol. 8, p. 031029, Jul 2018.

[17] R. Lai, R. Shankar, D. Spirn, and G. Uhlmann, "An inverse problem from condensed matter physics," *Inverse Problems*, vol. 33, p. 115011, Oct. 2017.

[18] E. Tsymbal and P. Dowben, "Grand challenges in condensed matter physics: from knowledge to innovation," *Frontiers in Physics*, vol. 1, p. 32, 2013.

[19] J. van der Gucht, "Grand challenges in soft matter physics," *Frontiers in Physics*, vol. 6, p. 87, 2018.

[20] G. Bertaina, D. E. Galli, and E. Vitali, "Statistical and computational intelligence approach to analytic continuation in Quantum Monte Carlo," *Advances in Physics: X*, vol. 2, no. 2, pp. 302–323, 2017.

[21] S. V. Dudiy and A. Zunger, "Searching for alloy configurations with target physical properties: Impurity design via a genetic algorithm inverse band structure approach," *Phys. Rev. Lett.*, vol. 97, p. 046401, Jul 2006.

[22] A. Franceschetti and A. Zunger, "The inverse band-structure problem of finding an atomic configuration with given electronic properties," *Nature*, vol. 402, pp. 60–63, Nov 1999.

[23] L. Yu, R. S. Kokenyesi, D. A. Keszler, and A. Zunger, "Inverse design of high absorption thin-film photovoltaic materials," *Adv. Energy Mater.*, vol. 3, no. 1, pp. 43–48, 2013.

[24] M. F. Kasim, T. Galligan, J. T. Mugglestone, G. Gregori, and S. M. Vinko, "Inverse problem instabilities in large-scale modelling of matter in extreme conditions," *Phys. Plasmas*, vol. 26, p. 112706, 2019.

[25] D. S. Jensen and A. Wasserman, "Numerical methods for the inverse problem of density functional theory," *Int. J. Quantum Chem.*, vol. 118, no. 1, p. e25425, 2018.

[26] R. Fournier, L. Wang, O. V. Yazyev, and Q. Wu, "Artificial neural network approach to the analytic continuation problem," *Phys. Rev. Lett.*, vol. 124, p. 056401, Feb 2020.

[27] L. Zhang, J.-W. Luo, A. Saraiva, B. Koiller, and A. Zunger, "Genetic design of enhanced valley splitting towards a spin qubit in silicon," *Nat. Commun.*, vol. 4, p. 2396, Sep 2013.

[28] M. d'Avezac, J.-W. Luo, T. Chanier, and A. Zunger, "Genetic-algorithm discovery of a direct-gap and optically allowed superstructure from indirect-gap si and ge semiconductors," *Phys. Rev. Lett.*, vol. 108, p. 027401, Jan 2012.

[29] V. Mlinar, "Utilization of inverse approach in the design of materials over nano- to macro-scale," *Annalen der Physik*, vol. 527, no. 3-4, pp. 187–204, 2015.

[30] R. A. Vargas-Hernández, Y. Guan, D. H. Zhang, and R. V. Krems, "Bayesian optimization for the inverse scattering problem in quantum reaction dynamics," *New J. Phys.*, vol. 21, p. 022001, feb 2019.

[31] O. Kyriienko, "Quantum inverse iteration algorithm for programmable quantum simulators," *npj Quantum Information*, vol. 6, 12 2020.

[32] A. Lopez-Bezanilla and O. A. von Lilienfeld, "Modeling electronic quantum transport with machine learning," *Phys. Rev. B*, vol. 89, p. 235411, Jun 2014.

[33] K. Hansen, G. Montavon, F. Biegler, S. Fazli, M. Rupp, M. Scheffler, O. A. von Lilienfeld, A. Tkatchenko, and K.-R. MÃŒller, "Assessment and validation of machine learning methods for predicting molecular atomization energies," *J. Chem. Theory Comput.*, vol. 9, no. 8, pp. 3404–3419, 2013.

[34] B. Himmetoglu, "Tree based machine learning framework for predicting ground state energies of molecules," *J. Chem. Phys.*, vol. 145, no. 13, p. 134101, 2016.

[35] H. Li, C. Collins, M. Tanha, G. J. Gordon, and D. J. Yaron, "A density functional tight binding layer for deep learning of chemical Hamiltonians," *J. Chem. Theory Comput.*, vol. 14, p. 5764, 2018.

[36] R. Xia and S. Kais, "Quantum machine learning for electronic structure calculations," *Nat. Commun.*, vol. 9, p. 4195, Oct 2018.

[37] P. O. Dral, "Quantum chemistry in the age of machine learning," *J. Phys. Chem. Lett.*, vol. 11, no. 6, pp. 2336–2347, 2020.

[38] J. Carrasquilla and R. G. Melko, "Machine learning phases of matter," *Nat. Phys.*, vol. 13, pp. 431–434, May 2017.

[39] Y. Leng, *Materials characterization: introduction to microscopic and spectroscopic methods*. John Wiley & Sons, 2009.

[40] F. J. Giessibl, "Advances in atomic force microscopy," *Reviews of Modern Physics*, vol. 75, no. 3, p. 949, 2003.

[41] J. I. Goldstein, D. E. Newbury, J. R. Michael, N. W. Ritchie, J. H. J. Scott, and D. C. Joy, *Scanning electron microscopy and X-ray microanalysis*. Springer, 2017.

[42] A. Guinier, *X-ray diffraction in crystals, imperfect crystals, and amorphous bodies*. Courier Corporation, 1994.

[43] K. Novoselov, "Nobel lecture: Graphene: Materials in the flatland," *Rev. Mod. Phys.*, vol. 83, no. 3, p. 837, 2011.

[44] C. Beenakker and H. van Houten, "Quantum transport in semiconductor nanostructures," in *Solid State Physics*, vol. 44, pp. 1–228, Elsevier, 1991.

[45] Z. Zanolli, R. Leghrib, A. Felten, J.-J. Pireaux, E. Llobet, and J.-C. Charlier, "Gas sensing with au-decorated carbon nanotubes," *ACS Nano*, vol. 5, no. 6, pp. 4592–4599, 2011. PMID: 21553864.

[46] S. Yuan, R. Roldán, M. Katsnelson, and F. Guinea, "Effect of point defects on the optical and transport properties of mos 2 and ws 2," *Physical Review B*, vol. 90, no. 4, p. 041402, 2014.

[47] W. Choi, N. Choudhary, G. H. Han, J. Park, D. Akinwande, and Y. H. Lee, "Recent development of two-dimensional transition metal dichalcogenides and their applications," *Materials Today*, vol. 20, no. 3, pp. 116–130, 2017.

[48] M. Chhowalla, Z. Liu, and H. Zhang, "Two-dimensional transition metal dichalcogenide (tmd) nanosheets," *Chemical Society Reviews*, vol. 44, no. 9, pp. 2584–2586, 2015.

[49] X. Duan, C. Wang, A. Pan, R. Yu, and X. Duan, "Two-dimensional transition metal dichalcogenides as atomically thin semiconductors: opportunities and challenges," *Chemical Society Reviews*, vol. 44, no. 24, pp. 8859–8876, 2015.

[50] D. Akinwande, N. Petrone, and J. Hone, "Two-dimensional flexible nanoelectronics," *Nature communications*, vol. 5, p. 5678, 2014.

[51] H. Li, S. Wang, H. Sawada, G. G. Han, T. Samuels, C. S. Allen, A. I. Kirkland, J. C. Grossman, and J. H. Warner, "Atomic structure and dynamics of single

platinum atom interactions with monolayer mos2," *ACS nano*, vol. 11, no. 3, pp. 3392–3403, 2017.

[52] Y. Zhou, P. Yang, H. Zu, F. Gao, and X. Zu, "Electronic structures and magnetic properties of mos 2 nanostructures: atomic defects, nanoholes, nanodots and antidots," *Physical Chemistry Chemical Physics*, vol. 15, no. 25, pp. 10385–10394, 2013.

[53] D. Yang, X. Fan, F. Zhang, Y. Hu, and Z. Luo, "Electronic and magnetic properties of defected monolayer wse 2 with vacancies," *Nanoscale research letters*, vol. 14, no. 1, pp. 1–9, 2019.

[54] K. S. Novoselov, A. K. Geim, S. V. Morozov, D. Jiang, M. I. Katsnelson, I. Grigorieva, S. Dubonos, and a. Firsov, "Two-dimensional gas of massless dirac fermions in graphene," *nature*, vol. 438, no. 7065, pp. 197–200, 2005.

[55] C. G. Rocha and M. S. Ferreira, "A simple theoretical approach to designing nanotube-based sensors," *physica status solidi (b)*, vol. 248, no. 3, pp. 686–693, 2011.

[56] D. P. Langley, M. Lagrange, G. Giusti, C. JimÃ©nez, Y. BrÃ©chet, N. D. Nguyen, and D. Bellet, "Metallic nanowire networks: effects of thermal annealing on electrical resistance," *Nanoscale*, vol. 6, pp. 13535–13543, 2014.

[57] M. Song, D. S. You, K. Lim, S. Park, S. Jung, C. S. Kim, D.-H. Kim, D.-G. Kim, J.-K. Kim, J. Park, Y.-C. Kang, J. Heo, S.-H. Jin, J. H. Park, and J.-W. Kang, "Highly efficient and bendable organic solar cells with solution-processed silver nanowire electrodes," *Advanced Functional Materials*, vol. 23, no. 34, pp. 4177–4184, 2013.

[58] D. Bellet, M. Lagrange, T. Sannicolo, S. Aghazade-hchors, V. H. Nguyen, D. P. Langley, D. MuÃ±oz – Rojas, C. JimÃ©nez, Y. BrÃ©chet, andN. D.Nguyen, "Transparentelectrodesbasedonsilvern Fromphysicalconsiderationstowardsdeviceintegration," Materials, vol. 10, no. 6, 2017.

[59] I. E. Stewart, A. R. Rathmell, L. Yan, S. Ye, P. F. Flowers, W. You, and B. J. Wiley, "Solution-processed copperânickel nanowire anodes for organic solar cells," *Nanoscale*, vol. 6, pp. 5980–5988, 2014.

[60] P. Won, J. J. Park, T. Lee, I. Ha, S. Han, M. Choi, J. Lee, S. Hong, K.-J. Cho, and S. H. Ko, "Stretchable and transparent kirigami conductor of nanowire percolation network for electronic skin applications," *Nano letters*, vol. 19, no. 9, pp. 6087–6096, 2019.

[61] A. R. Madaria, A. Kumar, F. N. Ishikawa, and C. Zhou, "Uniform, highly conductive, and patterned transparent films of a percolating silver nanowire network on rigid and flexible substrates using a dry transfer technique," *Nano research*, vol. 3, no. 8, pp. 564–573, 2010.

[62] H. G. Manning, F. Niosi, C. G. da Rocha, A. T. Bellew, C. OâCallaghan, S. Biswas, P. F. Flowers, B. J. Wiley, J. D. Holmes, M. S. Ferreira, *et al.*, "Emergence of winner-takes-all connectivity paths in random nanowire networks," *Nature communications*, vol. 9, no. 1, pp. 1–9, 2018.

[63] P. N. Nirmalraj, A. T. Bellew, A. P. Bell, J. A. Fairfield, E. K. McCarthy, C. OâKelly, L. F. Pereira, S. Sorel, D. Morosan, J. N. Coleman, *et al.*, "Manipulating connectivity and electrical conductivity in metallic nanowire networks," *Nano letters*, vol. 12, no. 11, pp. 5966–5971, 2012.

[64] A. T. Bellew, A. P. Bell, E. K. McCarthy, J. A. Fairfield, and J. J. Boland, "Programmability of nanowire networks," *Nanoscale*, vol. 6, no. 16, pp. 9632–9639, 2014.

[65] A. T. Bellew, H. G. Manning, C. Gomes da Rocha, M. S. Ferreira, and J. J. Boland, "Resistance of single ag nanowire junctions and their role in the conductivity of nanowire networks," *ACS nano*, vol. 9, no. 11, pp. 11422–11429, 2015.

[66] E. N. Economou, *Green's functions in quantum physics*, vol. 7. Springer Science & Business Media, 2006.

[67] A. Ziletti, D. Kumar, M. Scheffler, and L. M. Ghiringhelli, "Insightful classification of crystal structures using deep learning," *Nat. Commun.*, vol. 9, p. 2775, Jul 2018.

[68] R. Potyrailo, K. Rajan, K. Stoewe, I. Takeuchi, B. Chisholm, and H. Lam, "Combinatorial and high-throughput screening of materials libraries: Review of state of the art," *ACS Comb. Sci.*, vol. 13, no. 6, pp. 579–633, 2011.

[69] S. K. Suram, P. F. Newhouse, L. Zhou, D. G. Van Campen, A. Mehta, and J. M. Gregoire, "High throughput light absorber discovery, part 2: Establishing structureâband gap energy relationships," *ACS Comb. Sci.*, vol. 18, no. 11, pp. 682–688, 2016.

[70] H. Koinuma and I. Takeuchi, "Combinatorial solid-state chemistry of inorganic materials," *Nat. Mater.*, vol. 3, pp. 429–438, Jul 2004.

[71] M. L. Green, C. L. Choi, J. R. Hattrick-Simpers, A. M. Joshi, I. Takeuchi, S. C. Barron, E. Campo, T. Chiang, S. Empedocles, J. M. Gregoire, A. G. Kusne, J. Martin, A. Mehta, K. Persson, Z. Trautt, J. Van Duren, and A. Zakutayev, "Fulfilling the promise of the materials genome initiative with high-throughput experimental methodologies," *Appl. Phys. Rev.*, vol. 4, no. 1, p. 011105, 2017.

[72] S. Curtarolo, G. L. W. Hart, M. B. Nardelli, N. Mingo, S. Sanvito, and O. Levy, "The high-throughput highway to computational materials design," *Nat. Mater.*, vol. 12, pp. 191–201, Mar 2013.

[73] L. Yu and A. Zunger, "Identification of potential photovoltaic absorbers based on first-principles spectroscopic screening of materials," *Phys. Rev. Lett.*, vol. 108, p. 068701, Feb 2012.

[74] F. Yan, X. Zhang, Y. G. Yu, L. Yu, A. Nagaraja, T. O. Mason, and A. Zunger, "Design and discovery of a novel half-heusler transparent hole conductor made of all-metallic heavy elements," *Nat. Commun.*, vol. 6, p. 7308, Jun 2015.

[75] C. C. Fischer, K. J. Tibbetts, D. Morgan, and G. Ceder, "Predicting crystal structure by merging data mining with quantum mechanics," *Nat. Mater.*, vol. 5, pp. 641–646, Aug 2006.

[76] R. Gautier, X. Zhang, L. Hu, L. Yu, Y. Lin, T. O. L. Sunde, D. Chon, K. R. Poeppelmeier, and A. Zunger, "Prediction and accelerated laboratory discovery of previ-

ously unknown 18-electron abx compounds," *Nat. Chem.*, vol. 7, pp. 308–316, Apr 2015.

[77] R. Kubo, "Statistical-mechanical theory of irreversible processes. i. general theory and simple applications to magnetic and conduction problems," *Journal of the Physical Society of Japan*, vol. 12, no. 6, pp. 570–586, 1957.

[78] A. G. Kelly, J. O'Reilly, C. Gabbett, B. SzydÅowska, D. O'Suilleabhain, U. Khan, J. Maughan, T. Carey, S. Sheil, P. Stamenov, and J. N. Coleman, "Highly conductive networks of silver nanosheets," *Small*, vol. 18, no. 14, p. 2105996, 2022.

[79] J. Mathon, "Large enhancement of the perpendicular giant magnetoresistance in pseudorandom magnetic multilayers," *Physical Review B*, vol. 54, no. 1, p. 55, 1996.

[80] C. H. Lewenkopf and E. R. Mucciolo, "The recursive greenâs function method for graphene," *Journal of Computational Electronics*, vol. 12, no. 2, pp. 203–231, 2013.

[81] E. R. Mucciolo and C. H. Lewenkopf, "Disorder and electronic transport in graphene," *Journal of Physics: Condensed Matter*, vol. 22, no. 27, p. 273201, 2010.

[82] K. Nomura and A. H. MacDonald, "Quantum transport of massless dirac fermions," *Physical review letters*, vol. 98, no. 7, p. 076602, 2007.

[83] J. Tworzydło, C. Groth, and C. Beenakker, "Finite difference method for transport properties of massless dirac fermions," *Physical Review B*, vol. 78, no. 23, p. 235438, 2008.

[84] A. R. Hernández and C. H. Lewenkopf, "Finite-difference method for transport of two-dimensional massless dirac fermions in a ribbon geometry," *Physical Review B*, vol. 86, no. 15, p. 155439, 2012.

[85] F. J. Dyson, "The s matrix in quantum electrodynamics," *Physical Review*, vol. 75, no. 11, p. 1736, 1949.

[86] J. Schwinger, "On the green’s functions of quantized fields. i," *Proceedings of the National Academy of Sciences*, vol. 37, no. 7, pp. 452–455, 1951.

[87] H. Haug, A.-P. Jauho, *et al.*, *Quantum kinetics in transport and optics of semiconductors*, vol. 2. Springer, 2008.

[88] D. Thouless and S. Kirkpatrick, "Conductivity of the disordered linear chain," *Journal of Physics C: Solid State Physics*, vol. 14, no. 3, p. 235, 1981.

[89] P. S. Drouvelis, P. Schmelcher, and P. Bastian, "Parallel implementation of the recursive greenâs function method," *Journal of Computational Physics*, vol. 215, no. 2, pp. 741–756, 2006.

[90] D. Ferry and S. Goodnick, "Transport in nanostructures, cambridge univ," *Press, Cambridge*, 1997.

[91] P. A. Lee and D. S. Fisher, "Anderson localization in two dimensions," *Physical Review Letters*, vol. 47, no. 12, p. 882, 1981.

[92] Y. Meir and N. S. Wingreen, "Landauer formula for the current through an interacting electron region," *Phys. Rev. Lett.*, vol. 68, pp. 2512–2515, Apr 1992.

[93] S. Power and M. Ferreira, "Electronic structure of graphene beyond the linear dispersion regime," *Phys. Rev. B*, vol. 83, no. 15, p. 155432, 2011.

[94] K. S. Novoselov, A. K. Geim, S. Morozov, D. Jiang, M. I. Katsnelson, I. Grigorieva, S. Dubonos, Firsov, and AA, "Two-dimensional gas of massless Dirac fermions in graphene," *Nature*, vol. 438, no. 7065, pp. 197–200, 2005.

[95] L. Brey and H. Fertig, "Electronic states of graphene nanoribbons studied with the dirac equation," *Physical Review B*, vol. 73, no. 23, p. 235411, 2006.

[96] H. U. Baranger and P. A. Mello, "Mesoscopic transport through chaotic cavities: A random S-matrix theory approach," *Phys. Rev. Lett.*, vol. 73, pp. 142–145, Jul 1994.

[97] P. A. Lee and A. D. Stone, "Universal conductance fluctuations in metals," *Phys. Rev. Lett.*, vol. 55, pp. 1622–1625, Oct 1985.

[98] P. A. Lee, A. D. Stone, and H. Fukuyama, "Universal conductance fluctuations in metals: Effects of finite temperature, interactions, and magnetic field," *Phys. Rev. B*, vol. 35, pp. 1039–1070, Jan 1987.

[99] Y. Alhassid, "The statistical theory of quantum dots," *Rev. Mod. Phys.*, vol. 72, pp. 895–968, Oct 2000.

[100] A. Lopez-Bezanilla and O. A. von Lilienfeld, "Modeling electronic quantum transport with machine learning," *Phys. Rev. B*, vol. 89, p. 235411, Jun 2014.

[101] A. Mikhailiuk and A. Faul, "Deep learning applied to seismic data interpolation," vol. 2018, no. 1, pp. 1–5, 2018.

[102] A. Lopez-Bezanilla and O. A. von Lilienfeld, "Modeling electronic quantum transport with machine learning," *Phys. Rev. B*, vol. 89, p. 235411, Jun 2014.

[103] P. Soven, "Coherent-potential model of substitutional disordered alloys," *Physical Review*, vol. 156, no. 3, p. 809, 1967.

[104] C. H. Lewenkopf and H. A. Weidenmüller, "Stochastic versus semiclassical approach to quantum chaotic scattering," *Ann. Phys.*, vol. 212, pp. 53–83, 1991.

[105] E. R. P. Alves and C. H. Lewenkopf, "Conductance fluctuations and weak localization in chaotic quantum dots," *Phys. Rev. Lett.*, vol. 88, p. 256805, Jun 2002.

[106] J. French, P. Mello, and A. Pandey, "Ergodic behavior in the statistical theory of nuclear reactions," *Phys. Lett. B*, vol. 80, no. 1, pp. 17 – 19, 1978.

[107] T. Guhr, A. Müller-Groeling, and H. A. Weidenmüller, "Random-matrix theories in quantum physics: common concepts," *Phys. Rep.*, vol. 299, no. 4, pp. 189 – 425, 1998.

[108] A. H. Castro Neto, F. Guinea, N. M. R. Peres, K. S. Novoselov, and A. K. Geim, "The electronic properties of graphene," *Rev. Mod. Phys.*, vol. 81, pp. 109–162, Jan 2009.

[109] S. Das Sarma, S. Adam, E. H. Hwang, and E. Rossi, "Electronic transport in two-dimensional graphene," *Rev. Mod. Phys.*, vol. 83, pp. 407–470, May 2011.

[110] S. Datta, *Quantum transport: atom to transistor*. Cambridge: Cambridge University Press, 2005.

[111] A. Dibenedetto, *The electronic properties of hexagonal boron nitride and graphene nanoribbons*. Ball State University Master thesis, 2017.

[112] W. Harrison, *Electronic Structure and the Properties of Solids: The Physics of the Chemical Bond*. Dover Publications, 1989.

[113] D. Gresch, G. Autes, O. V. Yazyev, M. Troyer, D. Vanderbilt, B. A. Bernevig, and A. A. Soluyanov, "Z2pack: Numerical implementation of hybrid wannier centers for identifying topological materials," *Phys. Rev. B*, vol. 95, no. 7, p. 075146, 2017.

[114] G. Pizzi, V. Vitale, R. Arita, S. Blügel, F. Freimuth, G. Géranton, M. Gibertini, D. Gresch, C. Johnson, T. Koretsune, J. Ibañez-Azpiroz, H. Lee, J.-M. Lihm, D. Marchand, A. Marrazzo, Y. Mokrousov, J. I. Mustafa, Y. Nohara, Y. Nomura, L. Paulatto, S. Poncé, T. Ponweiser, J. Qiao, F. Thöle, S. S. Tsirkin, M. Wierzbowska, N. Marzari, D. Vanderbilt, I. Souza, A. A. Mostofi, and J. R. Yates, "Wannier90 as a community code: new features and applications," *J. Phys.: Condens. Matter*, vol. 32, p. 165902, jan 2020.

[115] M. B. Nardelli, F. T. Cerasoli, M. Costa, S. Curtarolo, R. De Gennaro, M. Fornari, L. Liyanage, A. R. Supka, and H. Wang, "PAOFLOW: A utility to construct and operate on ab initio hamiltonians from the projections of electronic wavefunctions on atomic orbital bases, including characterization of topological materials," *Comput. Mater. Sci.*, vol. 143, pp. 462–472, 2018.

[116] D. Vanderbilt, *The PythTB Package*, pp. 327–362. Cambridge: Cambridge University Press, 2018.

[117] C. W. Groth, M. Wimmer, A. R. Akhmerov, and X. Waintal, "Kwant: a software package for quantum transport," *New J. Phys.*, vol. 16, no. 6, p. 063065, 2014.

[118] L. R. F. Lima, A. Dusko, and C. Lewenkopf, "Efficient method for computing the electronic transport properties of a multiterminal system," *Phys. Rev. B*, vol. 97, no. 16, p. 165405, 2018.

[119] S. M. João, M. Anđelković, L. Covaci, T. G. Rappoport, J. M. Lopes, and A. Ferreira, "Kite: high-performance accurate modelling of electronic structure and response functions of large molecules, disordered crystals and heterostructures," *R. Soc. Open Sci.*, vol. 7, no. 2, p. 191809, 2020.

[120] D. A. Papaconstantopoulos *et al.*, *Handbook of the band structure of elemental solids*. Springer, 1986.

[121] J. C. Slater and G. F. Koster, "Simplified LCAO method for the periodic potential problem," *Phys. Rev.*, vol. 94, pp. 1498–1524, Jun 1954.

[122] R. G. Amorim, A. Fazzio, A. J. R. da Silva, and A. R. Rocha, "Confinement effects and why carbon nanotube bundles can work as gas sensors," *Nanoscale*, vol. 5, pp. 2798–2803, 2013.

[123] C. G. Rocha, A. Wall, A. R. Rocha, and M. S. Ferreira, "Modelling the effect of randomly dispersed adatoms on carbon nanotubes," *J. Phys.: Condens. Matter*, vol. 19, p. 346201, 2007.

[124] A. R. Rocha, M. Rossi, A. Fazzio, and A. J. R. da Silva, "Designing real nanotube-based gas sensors," *Phys. Rev. Lett.*, vol. 100, p. 176803, 2008.

[125] A. R. Rocha, M. Rossi, A. J. R. da Silva, and A. Fazzio, "Realistic calculations of carbon-based disordered systems," *J. Phys. D: Appl. Phys.*, vol. 43, p. 374002, 2010.

[126] G. R. Schleder, A. C. M. Padilha, C. M. Acosta, M. Costa, and A. Fazzio, "From DFT to machine learning: recent approaches to materials science-a review," *Journal of Physics: Materials*, vol. 2, p. 032001, July 2019.

[127] T. Ihn, *Semiconductor Nanostructures*. Oxford: Oxford University Press, 2010.

[128] F. Ghahari, Y. Zhao, P. Cadden-Zimansky, K. Bolotin, and P. Kim, "Measurement of the $\nu = 1/3$ fractional quantum hall energy gap in suspended graphene," *Phys. Rev. Lett.*, vol. 106, p. 046801, Jan 2011.

[129] E. Perkins, L. Barreto, J. Wells, and P. Hofmann, "Surface-sensitive conductivity measurement using a micro multi-point probe approach," *Rev. Sci. Instrum.*, vol. 84, no. 3, p. 033901, 2013.

[130] H. Lee, D. Cho, S. Shekhar, J. Kim, J. Park, B. H. Hong, and S. Hong, "Nanoscale direct mapping of noise source activities on graphene domains," *ACS Nano*, vol. 10, no. 11, pp. 10135–10142, 2016. PMID: 27934081.

[131] X. Cui, G.-H. Lee, Y. D. Kim, G. Arefe, P. Y. Huang, C.-H. Lee, D. A. Chenet, X. Zhang, L. Wang, F. Ye, F. Pizzocchero, B. S. Jessen, K. Watanabe, T. Taniguchi, D. A. Muller, T. Low, P. Kim, and J. Hone, "Multi-terminal transport measurements of MoS_2 using a van der waals heterostructure device platform," *Nature Nanotechnology*, vol. 10, no. 6, pp. 534–540, 2015.

[132] N. Shin, J. Kim, S. Shekhar, M. Yang, and S. Hong, "Nanoscale reduction of resistivity and charge trap activities induced by carbon nanotubes embedded in metal thin films," *Carbon*, vol. 141, pp. 59–66, 2019.

[133] M. Büttiker, "Four-terminal phase-coherent conductance," *Phys. Rev. Lett.*, vol. 57, pp. 1761–1764, Oct 1986.

[134] M. Jura, M. Topinka, L. Urban, A. Yazdani, H. Shtrikman, L. N. Pfeiffer, K. W. West, and D. Goldhaber-Gordon, "Unexpected features of branched flow through high-mobility two-dimensional electron gases," *Nat. Phys.*, vol. 3, p. 841â845, 2007.

[135] B. A. Braem, F. M. D. Pellegrino, A. Principi, M. Röösli, C. Gold, S. Hennel, J. V. Koski, M. Berl, W. Dietsche, W. Wegscheider, M. Polini, T. Ihn, and K. Ensslin, "Scanning gate microscopy in a viscous electron fluid," *Phys. Rev. B*, vol. 98, p. 241304, Dec 2018.

[136] B. Brun, N. Moreau, S. Somanchi, V.-H. Nguyen, K. Watanabe, T. Taniguchi, J.-C. Charlier, C. Stampfer, and B. Hackens, "Imaging Dirac fermions flow through a circular Veselago lens," *Phys. Rev. B*, vol. 100, p. 041401, Jul 2019.

[137] B. Brun, N. Moreau, S. Somanchi, V.-H. Nguyen, A. Mreńca-Kolasińska, K. Watanabe, T. Taniguchi, J.-C. Charlier, C. Stampfer, and B. Hackens, "Optimizing Dirac fermions quasi-confinement by potential smoothness engineering," *2D Materials*, vol. 7, p. 025037, mar 2020.

[138] A.-P. Li, K. W. Clark, X.-G. Zhang, and A. P. Baddorf, "Electron transport at the nanometer-scale spatially revealed by four-probe scanning tunneling microscopy," *Advanced Functional Materials*, vol. 23, no. 20, pp. 2509–2524, 2013.

[139] J. Baringhaus, M. Ruan, F. Edler, A. Tejeda, M. Sicot, A. Taleb-Ibrahimi, A.-P. Li, Z. Jiang, E. H. Conrad, C. Berger, C. Tegenkamp, and W. A. de Heer, "Exceptional ballistic transport in epitaxial graphene nanoribbons," *Nature*, vol. 506, p. 349, 2014.

[140] J. Duffy, J. Lawlor, C. Lewenkopf, and M. S. Ferreira, "Impurity invisibility in graphene: Symmetry guidelines for the design of efficient sensors," *Phys. Rev. B*, vol. 94, p. 045417, Jul 2016.

[141] E. Ridolfi, L. R. F. Lima, E. R. Mucciolo, and C. H. Lewenkopf, "Electronic transport in disordered MoS_2 nanoribbons," *Phys. Rev. B*, vol. 95, p. 035430, Jan 2017.

[142] S. Mukim, C. Lewenkopf, and M. Ferreira, "Spatial mapping of disordered 2d systems: The conductance sudoku," *Carbon*, vol. 188, pp. 360–366, 2022.

[143] R. Adelung, L. Kipp, J. Brandt, L. Tarcak, M. Traving, C. Kreis, and M. Skibowski, "Nanowire networks on perfectly flat surfaces," *Applied physics letters*, vol. 74, no. 20, pp. 3053–3055, 1999.

[144] S. Iijima, "Helical microtubules of graphitic carbon," *nature*, vol. 354, no. 6348, pp. 56–58, 1991.

[145] K. S. Novoselov, A. K. Geim, S. V. Morozov, D.-e. Jiang, Y. Zhang, S. V. Dubonos, I. V. Grigorieva, and A. A. Firsov, "Electric field effect in atomically thin carbon films," *science*, vol. 306, no. 5696, pp. 666–669, 2004.

[146] K. F. Mak, C. Lee, J. Hone, J. Shan, and T. F. Heinz, "Atomically thin mos 2: a new direct-gap semiconductor," *Physical review letters*, vol. 105, no. 13, p. 136805, 2010.

[147] A. G. Kelly, D. Finn, A. Harvey, T. Hallam, and J. N. Coleman, "All-printed capacitors from graphene-bn-graphene nanosheet heterostructures," *Applied Physics Letters*, vol. 109, no. 2, p. 023107, 2016.

[148] X. Lan, J. Bai, S. Masala, S. M. Thon, Y. Ren, I. J. Kramer, S. Hoogland, A. Simchi, G. I. Koleilat, D. Paz-Soldan, *et al.*, "Self-assembled, nanowire network electrodes for depleted bulk heterojunction solar cells," *Advanced Materials*, vol. 25, no. 12, pp. 1769–1773, 2013.

[149] L. Chua, "Ieee trans. circuit theory," *Vol. CT-18 P*, vol. 507, 1971.

[150] I. Balberg, N. Binenbaum, and C. Anderson, "Critical behavior of the two-dimensional sticks system," *Physical Review Letters*, vol. 51, no. 18, p. 1605, 1983.

[151] G. Pike and C. Seager, "Percolation and conductivity: A computer study. i," *Physical review B*, vol. 10, no. 4, p. 1421, 1974.

[152] M. Žeželj and I. Stanković, "From percolating to dense random stick networks: Conductivity model investigation," *Physical Review B*, vol. 86, no. 13, p. 134202, 2012.

[153] S. Sorel, P. E. Lyons, S. De, J. C. Dickerson, and J. N. Coleman, "The dependence of the optoelectrical properties of silver nanowire networks on nanowire length and diameter," *Nanotechnology*, vol. 23, no. 18, p. 185201, 2012.

[154] R. M. Mutiso, M. C. Sherrott, A. R. Rathmell, B. J. Wiley, and K. I. Winey, "Integrating simulations and experiments to predict sheet resistance and optical transmittance in nanowire films for transparent conductors," *ACS nano*, vol. 7, no. 9, pp. 7654–7663, 2013.

[155] A. Ponzoni, "The contributions of junctions and nanowires/nanotubes in conductive networks," *Applied Physics Letters*, vol. 114, no. 15, p. 153105, 2019.

[156] C. Pozrikidis, *An introduction to grids, graphs, and networks*. Oxford University Press, 2014.

[157] R. Aitchison, "Resistance between adjacent points of liebman mesh," *American Journal of Physics*, vol. 32, no. 7, pp. 566–566, 1964.

[158] M. Jevons, "Square lattice resistance networks with diagonal elements," *Journal of Scientific Instruments*, vol. 44, no. 7, p. 514, 1967.

[159] P. E. Lyons, S. De, F. Blighe, V. Nicolosi, L. F. C. Pereira, M. S. Ferreira, and J. N. Coleman, "The relationship between network morphology and conductivity in nanotube films," *Journal of Applied Physics*, vol. 104, no. 4, p. 044302, 2008.

[160] J. Cserti, G. Dávid, and A. Piróth, "Perturbation of infinite networks of resistors," *American Journal of Physics*, vol. 70, no. 2, pp. 153–159, 2002.

[161] J. Cserti, "Application of the lattice greenâs function for calculating the resistance of an infinite network of resistors," *American Journal of Physics*, vol. 68, no. 10, pp. 896–906, 2000.

[162] G. Venezian, "On the resistance between two points on a grid," *American Journal of Physics*, vol. 62, no. 11, pp. 1000–1004, 1994.

[163] M. Kagan, "On equivalent resistance of electrical circuits," *American Journal of Physics*, vol. 83, no. 1, pp. 53–63, 2015.

[164] D. Atkinson and F. Van Steenwijk, "Infinite resistive lattices," *American Journal of Physics*, vol. 67, no. 6, pp. 486–492, 1999.

[165] G. Strang and L. Freund, "Introduction to applied mathematics," *Journal of Applied Mechanics*, vol. 53, no. 2, p. 480, 1986.

[166] S. Kirkpatrick, "Percolation and conduction," *Reviews of modern physics*, vol. 45, no. 4, p. 574, 1973.

[167] J. Fairfield, C. Rocha, C. O'Callaghan, M. Ferreira, and J. Boland, "Co-percolation to tune conductive behaviour in dynamical metallic nanowire networks," *Nanoscale*, vol. 8, no. 43, pp. 18516–18523, 2016.

[168] C. G. da Rocha, H. G. Manning, C. O'Callaghan, C. Ritter, A. T. Bellew, J. J. Boland, and M. S. Ferreira, "Ultimate conductivity performance in metallic nanowire networks," *Nanoscale*, vol. 7, no. 30, pp. 13011–13016, 2015.

[169] C. O'Callaghan, C. G. da Rocha, H. G. Manning, J. J. Boland, and M. S. Ferreira, "Effective medium theory for the conductivity of disordered metallic nanowire networks," *Physical Chemistry Chemical Physics*, vol. 18, no. 39, pp. 27564–27571, 2016.

[170] F. Yang, "Size effect on electric-double-layer capacitances of conducting structures," *Physics Letters A*, vol. 383, no. 20, pp. 2353–2360, 2019.

[171] L. Tortet, J. Gavarri, J. Musso, G. Nihoul, J. Clerc, A. Lagarkov, and A. Sarychev, "Impedance spectroscopy of brushite composites and a scaling approach to the

dispersion behavior of inhomogeneous ionic conductors," *Physical Review B*, vol. 58, no. 9, p. 5390, 1998.

[172] A. James, C. Prakash, and G. Prasad, "Structural properties and impedance spectroscopy of excimer laser ablated zr substituted batio3 thin films," *Journal of Physics D: Applied Physics*, vol. 39, no. 8, p. 1635, 2006.

[173] S. Gupta, N. Prasad, and V. Wadhawan, "Impedance spectroscopy of the relaxor behaviour of pmn and la-doped pmn-pt compositions," *Ferroelectrics*, vol. 326, no. 1, pp. 43–47, 2005.

[174] W. Han, R. K. Kawakami, M. Gmitra, and J. Fabian, "Graphene spintronics," *Nature nanotechnology*, vol. 9, no. 10, pp. 794–807, 2014.

[175] K. Nakada, M. Fujita, G. Dresselhaus, and M. S. Dresselhaus, "Edge state in graphene ribbons: Nanometer size effect and edge shape dependence," *Physical Review B*, vol. 54, no. 24, p. 17954, 1996.

[176] P. Venezuela, R. Muniz, A. Costa, D. Edwards, S. Power, and M. Ferreira, "Emergence of local magnetic moments in doped graphene-related materials," *Physical Review B*, vol. 80, no. 24, p. 241413, 2009.

[177] H. Wang, H. S. Wang, C. Ma, L. Chen, C. Jiang, C. Chen, X. Xie, A.-P. Li, and X. Wang, "Graphene nanoribbons for quantum electronics," *Nature Reviews Physics*, vol. 3, no. 12, pp. 791–802, 2021.

[178] M. E. Kucukbas, S. McCann, and S. R. Power, "Predicting magnetic edge behaviour in graphene using neural networks," *arXiv preprint arXiv:2204.13724*, 2022.

[179] F. R. Duarte Filho, S. Mukim, A. Molina Sanchez, T. Rappoport, and M. S. Ferreira, "Decoding the DC and optical conductivities of disordered MoS_2 films: an inverse problem," *New Journal of Physics*, 2021.

[180] S. R. Power and M. S. Ferreira, "Indirect exchange and ruderman–kittel–kasuya–yosida (rkky) interactions in magnetically-doped graphene," *Crystals*, vol. 3, no. 1, pp. 49–78, 2013.

[181] P. D. Gorman, J. M. Duffy, S. R. Power, and M. S. Ferreira, "Rkky interaction between extended magnetic defect lines in graphene," *Physical Review B*, vol. 90, no. 12, p. 125411, 2014.

[182] M. A. Ruderman and C. Kittel, "Indirect exchange coupling of nuclear magnetic moments by conduction electrons," *Physical Review*, vol. 96, no. 1, p. 99, 1954.

[183] T. Kasuya, "A theory of metallic ferro-and antiferromagnetism on zener's model," *Progress of theoretical physics*, vol. 16, no. 1, pp. 45–57, 1956.

[184] K. Yosida, "Magnetic properties of cu-mn alloys," *Physical Review*, vol. 106, no. 5, p. 893, 1957.

[185] O. V. Yazyev, "Emergence of magnetism in graphene materials and nanostructures," *Reports on Progress in Physics*, vol. 73, no. 5, p. 056501, 2010.

[186] S. Wolf, D. Awschalom, R. Buhrman, J. Daughton, v. S. von Molnár, M. Roukes, A. Y. Chtchelkanova, and D. Treger, "Spintronics: a spin-based electronics vision for the future," *science*, vol. 294, no. 5546, pp. 1488–1495, 2001.

[187] D. D. Awschalom and M. E. Flatté, "Challenges for semiconductor spintronics," *Nature physics*, vol. 3, no. 3, pp. 153–159, 2007.

[188] C. Chappert, A. Fert, and F. N. Van Dau, "The emergence of spin electronics in data storage," *Nature materials*, vol. 6, no. 11, pp. 813–823, 2007.

[189] T. Wakrim, C. Vallée, P. Gonon, C. Mannequin, and A. Sylvestre, "From memristor to memimpedance device," *Applied Physics Letters*, vol. 108, no. 5, p. 053502, 2016.

[190] S. Barwich, J. Medeiros de AraÃºjo, A. Rafferty, C. Gomes da Rocha, M. S. Ferreira, and J. N. Coleman, "On the relationship between morphology and conductivity in nanosheet networks," *Carbon*, vol. 171, pp. 306–319, 2021.

[191] S. Datta, *Electronic Transport in Mesoscopic Systems*. Cambridge: Cambridge University Press, 1995.